

Large-scale geometry of the Universe

Yassir Awwad[♠] and Tomislav Prokopec[◇]

[◇] Institute for Theoretical Physics, Spinoza Institute & EMMEΦ
Utrecht University, Princetonplein 5, 3584 CC Utrecht, The Netherlands

Abstract

The large scale geometry of the late Universe can be decomposed as $\mathbb{R} \times \Sigma_3$, where \mathbb{R} stands for cosmic time and Σ_3 is the three dimensional spatial manifold. We conjecture that the geometry of the Universe's spatial section Σ_3 conforms with the Thurston-Perelman theorem, according to which the geometry of Σ_3 is either one of the eight geometries from the Thurston geometrization conjecture, or a combination of Thurston geometries smoothly sewn together. We assume that topology of individual geometries plays no observational role, *i.e.* the size of individual geometries is much larger than the Hubble radius today. We investigate the dynamics of each of the individual geometries by making use of the simplifying assumption that our local Hubble patch consists of only one such geometry, which is approximately homogeneous on very large scales, but spatial isotropy is generally violated.

Spatial anisotropies grow in time in decelerating universes, but they decay in accelerating universes. The thus-created *anisotropy problem* can be solved by a period of primordial inflation, akin to how the flatness problem is solved. Therefore, as regards Universe's large scale geometry, any of the Thurston's geometries should be considered on *a par* with Friedmann's geometries.

We consider two observational methods that can be used to test our conjecture: one based on luminosity distance and one on angular diameter distance measurements, but leave for the future their detailed forecasting implementations.

[♠] e-mail: Yassir@Awwad.nl

[◇] e-mail: T.Prokopec@uu.nl

Contents

1	Introduction & Motivation	3
1.1	The assumption of isotropy	3
1.2	Thurston-Perelman’s geometrization theorem	4
2	Thurston Space-Times	5
2.1	The FLRW geometries, \mathbb{R}^3 , \mathbb{H}^3 and \mathbb{S}^3	6
2.2	$\mathbb{R} \times \mathbb{H}^2$ and $\mathbb{R} \times \mathbb{S}^2$	6
2.3	$\widetilde{U(\mathbb{H}^2)}$	6
2.3.1	A sidenote on $\widetilde{SL(2, \mathbb{R})}$	7
2.4	Nil and Solv	7
3	Background Evolution	8
3.1	General solution	8
3.2	Friedmann Equations	9
3.3	Length scales	10
4	Distance Measures	12
4.1	Distance measures in an isotropic universe	12
4.1.1	Angular diameter distance	12
4.1.2	Luminosity distance	13
4.1.3	Etherington’s reciprocity theorem	13
4.2	Distance measures in an anisotropic universe	14
4.2.1	Angular diameter distance	14
4.2.2	Luminosity distance	16
4.2.3	The anisotropic reciprocity theorem	18
5	Distance Measures Visualised	19
5.1	Angular diameter distance	19
5.2	Luminosity distance	21
5.2.1	Spherical harmonics	22
5.2.2	Violation of parity & chiral symmetry	23
6	Anisotropic Scale Factors	25
6.1	Growth of anisotropies in an epoch with matter and cosmological constant	27
6.2	The Anisotropy Problem	30
7	Conclusion and Discussion	30
A	Geodesics of the $\mathbb{R} \times \mathbb{H}^2$ and $\mathbb{R} \times \mathbb{S}^2$ geometries	32
B	Geodesics of the $\widetilde{U(\mathbb{H}^2)}$ geometry	32
C	Geodesics of the Nil geometry	37
D	Geodesics of the Solv geometry	38

1 Introduction & Motivation

1.1 The assumption of isotropy

Much of modern cosmology, in particular the Lambda-CDM model, or Cold Dark Matter with cosmological constant, is based on the *Cosmological Principle*. This Principle is succinctly summarised by Milne [1], according to which “Two observers in uniform relative motion have *identical* views of the Universe”, *i.e.* that each sees the same evolving sequence of world-pictures. In its modern rendition, the Principle states that statistical properties of the Universe are the same to all local observers¹ and, in particular, that it is spatially homogeneous and isotropic at large enough scales.

The Cosmological Principle naturally leads one to also use a spatially homogeneous and isotropic metric – that is to say, the Friedmann-Lemaître-Robertson-Walker (FLRW) metric – to describe the space-time background of the Universe. By placing small metric perturbations on top of this background to break these symmetries, one can account for the formation of structures such as galaxies and clusters of galaxies. However, there is no strong *a priori* reason to believe that the symmetries of the background metric ought to be exact. In fact, the observational evidence for spatial isotropy and homogeneity is rather weak, if not controversial.

Based on the WMAP data, the assumption of spatial isotropy was questioned in Ref. [2], where the authors pointed at the anomalous alignment of the Cosmic Microwave Background (CMB) quadrupole and octopole (at the level $\sim 1/60$) (for a recent review of CMB anomalies, see Ref. [3]). The authors of Ref. [2] pointed out that the Universe with toroidal topology could explain such an alignment (albeit other features of this model were absent in the data); but they did not attempt geometric explanations. Later Refs. [4, 5] found no evidence for toroidal topology in the Planck satellite data. This analysis used a limited number of (Euclidean) topologies, and further investigations are warranted for a more complete understanding of what the data tell us about Universe’s topology, which include both Euclidean and curved spaces [6].

Land and Magueijo [7, 8, 9] further worked out the ideas in Ref. [2], and pointed out that the Universe may have a preferred axis, which approximately corresponds to that of the CMB dipole, suggesting that, on very large scales, the Universe violates spatial isotropy. Given that the WMAP observations of low multipoles were precise enough, the Planck data have not brought deep new insights into this question, see *e.g.* Refs. [10] and [11].²

Other CMB anomalies, summarized in [11, 12, 13], include the absence of large-angle correlations in the angular two-point function [14], point parity symmetry, the hemispherical power anomaly [15], the Cold Spot and other large-scale peaks [16, 17], with statistical significance for individual anomalies typically up to about 3σ (and sometimes more). More recent work [18] has studied the joint probability of multiple anomalies happening simultaneously by chance and concludes that this violates statistical isotropy by more than 5σ .

Recent LSS data tend to corroborate some of the the CMB anomalies, and even suggest new ones, For example, in his recent essay, Peebles [19] takes a more positive view on the anomalies, regarding them as tantalizing hints for new, as-yet-undisclosed physics. In particular, in section 3, Peebles considers anomalies in the large scale structure, and remarks: “The measured dipoles in the distribution of quasars and in the distributions of radio galaxies cataloged at several radio frequencies are in about the predicted direction, but the dipole amplitudes are too large, an anomaly,” for details see Refs. [20, 21, 22, 23]. Peebles also mentions some other (more local) anomalies, including the local void. For a more comprehensive overview of the existing anomalies and tensions in Λ CDM (which include the Hubble and σ_8 tensions) see Refs. [13], [3] and [24].

When combined, these observations and remarks present a well-grounded motivation for considering more general cosmological models that do not make the assumption of spatial isotropy, but are nonetheless capable of accounting what we observe in the night sky.

Another important question to which we do not have an unambiguous answer is: “do we live in a spatially flat or in a spatially curved universe?” When CMB data from the Planck mission [25] are combined with those from the Atacama Cosmology Telescope (ACT) [26, 27], and assuming a FLRW geometry, one obtains a Universe which is consistent with flat spatial sections. When LSS and Baryon Acoustic Oscillations (BAO) data are included one obtains, $\Omega_\kappa = -\kappa/H_0^2 = 0.001 \pm 0.002$, where H_0 is the expansion rate of the Universe today and κ Gauss’ curvature of the spatial sections. However, Planck’s measurements of the primary CMB anisotropies show evidence for a positively curved universe ($\kappa > 0$), and depending on the type of analysis used, one obtains $\Omega_\kappa = -0.044^{+0.018}_{-0.015}$ (3.4σ) when baseline Plik likelihood is used and $\Omega_\kappa = -0.035^{+0.018}_{-0.013}$ ($\gtrsim 2\sigma$) when CamCode likelihood analysis is used. At this moment it

¹The principle applies only to inertial observers in the rest frame of the Cosmic Microwave Background (CMB) photons, which defines the rest frame of the Universe. Any observer moving with respect to that frame perceives a CMB dipole and a large scale motion of the Universe’s Large Scale Structure (LSS).

²The Planck team is cautious regarding whether statistical anomalies in the CMB are real or just a statistical fluke: “The existence of these features is uncontested, but, given the modest significances at which they deviate from the standard Λ CDM cosmological model, and the *a posteriori* nature of their detection, the extent to which they provide evidence for a violation of isotropy in the CMB remains unclear. It is plausible that they are indeed simply statistical fluctuations.”

is unclear whether that is yet another anomaly, or a calibration problem. While the Planck collaboration analyses are based on the whole sky data (with our galaxy and point sources masked out), the ACT covers a fraction of the sky, possibly indicating a directional dependence in spatial curvature. A definite answer of this intriguing question will have to wait for EUCLID [28, 29] and SKAO [30], whose observations will break Planck data degeneracies with regard to Ω_κ and allow for a highly accurate measurement of spatial curvature, with an error of the order $\Delta\Omega_\kappa \sim 10^{-3}$ [31, 32].

In this paper, we explore the consequences of dropping the assumption of spatial isotropy from the outset and considering a broader set of possible *spatial geometries*. We are specifically interested in space-times that decompose into one time-like dimension and a three-dimensional spatial section as,

$$\mathcal{M} = \mathbb{R} \times \Sigma_3 \tag{1.1}$$

$$ds^2 = -dt^2 + a^2(t) \left(\gamma_{ij,\Sigma} dx^i dx^j \right). \tag{1.2}$$

We retain the assumption that spatial sections expand isotropically in (1.2) for now,³ but place no spatial isotropy requirement on the spatial section $(\Sigma_3, \gamma_{ij,\Sigma})$ itself.

The breakdown in equations (1.1–1.2) hinges on the assumption that there exists a spacelike three-dimensional hypersurface on which fluctuations in matter density vanish or are very small, and it exists if the *Cosmological Principle* holds approximately. There is a large body of observations which supports its approximate version; as discussed above, the data suggest a small violation of spatial isotropy.

Here we consider geometry of the Universe on large scales, and leave the question of topology for a future investigation. Namely, to each geometry one can associate different topologies.⁴ There is a large body of work devoted to investigating topology of the Universe, for reviews of existing attempts see Refs. [33, 34, 35, 4, 5, 6, 36]. Early attempts include the works of Starobinsky [37] and de Oliveira-Costa and Smoot [38], where the authors use the COBE data to investigate whether the Universe has toroidal topology, and find no evidence for it. Refs. [39, 40] look for circles in the CMB sky that would be an important sign of topology, but find no compelling evidence in favor of such circles.

It is interesting to note that topology can affect the amplitude of CMB fluctuations on large angular scales. Thus Ref. [41] showed that dodecahedral space topology in a spatially flat universe can suppress the amplitude of CMB fluctuations on the largest angular scales, thus explaining some of the large scale CMB anomalies. Similar results were found in Ref. [42], where the authors used $\mathbb{R}^2 \times S^1$ topology to explain the lack of CMB large-angle correlations.⁵

The search for candidates for Σ_3 leads us quite naturally to consider classification schemes for three-dimensional manifolds. For such a classification scheme, in this section and the next, we look towards the eight model geometries described in William Thurston’s geometrization conjecture [43], proven by Grigori Perelman in the early 2000s [44, 45, 46]. We consider the effect of the large-scale anisotropy inherent in these model geometries on the evolution of the Universe (Sections 3 and 6). Additionally, we study how large-scale anisotropy warps trajectories of light, thus deforming the image of faraway objects and affecting distance measures such as angular diameter distance and luminosity distance (Sections 4 and 5).

1.2 Thurston-Perelman’s geometrization theorem

Thurston-Perelman’s geometrization theorem⁶ is a partial classification of three-dimensional manifolds, analogous to the uniformization, theorem that classifies the possible geometries of Riemann surfaces. The main difference lies in the fact that not every 3-manifold can be endowed with a unique geometry, but rather every 3-manifold can be cut into pieces that can. Many formulations of the theorem exist, we will present the wording of Thurston’s original publication.

Thurston-Perelman’s geometrization theorem [43], [44, 45, 46]

The interior of every compact 3-manifold has a canonical decomposition into pieces which have geometric structures.

³In section 6 we drop the assumption of spatial isotropy of the scale factor, and present a detailed analysis of its dynamics.

⁴For example, if the Universe’s spatial sections are flat, then its geometry is \mathbb{R}^3 , which can be considered as the covering space of various topologies, the simplest ones being toroidal (\mathbb{T}^3), cuboidal ($\mathbb{T}^2 \times \mathbb{R}$) and slab ($\mathbb{T} \times \mathbb{R}^2 \simeq S^1 \times \mathbb{R}^2$).

⁵These findings are to be contrasted with the Planck 2013 [5], where one reads: “we consider flat spaces with cubic toroidal (T3), equal-sided chimney (T2) and slab (T1) topologies, three multi-connected spaces of constant positive curvature (dodecahedral, truncated cube and octahedral) and two compact negative-curvature spaces. These searches yield no detection of the compact topology with the scale below the diameter of the last scattering surface.” However, a more recent investigation [36] showed that, depending on topology, the lower constraint on the topology (length) scale may be weaker by a factor that ranges from 2 to at least 6.

⁶This theorem was initially formulated as a conjecture by Thurston and was later proven in Perelman. We therefore prefer to term it as a theorem as opposed to the conjecture moniker it commonly retains in literature.

Central to this theorem are the concepts of a geometry and a geometric structure. Briefly put, a Geometry is a pair $(X, \text{Isom}(X))$ consisting of a simply connected, complete and homogeneous Riemannian manifold X and its isometry group. A geometry $(Y, \text{Isom}(Y))$ is said to have a Geometric Structure based on X if there is a subgroup $A \subset \text{Isom}(X)$ such that Y is isometric to X/A and $\text{Isom}(Y)$ is homeomorphic to $\text{Isom}(X)/A$.

To give an example, the manifold $\mathbb{H}^2 \times S^1$ has a geometry based on $\mathbb{H}^2 \times \mathbb{R}$, since one can obtain the former from the latter taking a quotient with the subgroup $\mathbb{1}_{\mathbb{H}^2} \times \mathbb{Z}$ of $\text{Isom}(\mathbb{H}^2 \times \mathbb{R})$.

This notion can be used to define an ordering within the set of geometries, where geometry A is said to be of lower order of B if $\text{Isom}(A)$ is properly contained in $\text{Isom}(B)$. A natural follow-up question is to ask whether there are maximal geometries with respect to this ordering: are there geometries $(X, \text{Isom}(X))$ for which $\text{Isom}(X)$ is not properly contained in the isometry group of any other manifold? Thurston provides an answer to this exact question in his paper, which we will paraphrase here.

Any maximal, simply connected, three-dimensional geometry X that admits a compact quotient is equivalent to one of the eight geometries below.

- \mathbb{R}^3
- \mathbb{H}^3
- S^3
- Nil
- $\widetilde{\text{U}(\mathbb{H}^2)}$
- $\mathbb{H}^2 \times \mathbb{R}$
- $S^2 \times \mathbb{R}$
- Solv .

These eight maximal geometries can be said to form the building blocks of all compact 3-manifolds. This means that if we want to investigate space-time manifolds that decompose as in equation (1.1), then we can make a good start by modeling Σ_3 as one of the eight geometries of the above classification.

The fact that this classification applies only to compact manifolds or that a given manifold may consist of multiple copies of these geometries should not worry us too much. Due to the fact that inflation exponentially enlarges spatial sections of the Universe, it is highly likely that any complex geometric structure of the very early Universe is hidden beyond the Hubble radius, if we assume cosmic inflation occurred. Indeed, we argue in Section 3.3 that the curvature radius of any of these geometries is larger than the diameter of the observable Universe. It is therefore reasonable to assume that the observable patch of the Universe corresponds to only *one* of the Thurston geometries and, similarly, to make the additional simplifying assumption that many subtleties arising due to topology are not easily observable.⁷

We will concentrate on the consequences of introducing large-scale spatial anisotropy in the spatial part of the metric. We will make the simplifying assumption that the spatial section of the (observable) Universe corresponds to a single Thurston geometry and put aside any further topological considerations. An investigation into the possible effects of topology we will leave for future work.

2 Thurston Space-Times

In this section we will present explicit coordinate representations of space-times based on Thurston geometries. Following the approach outlined in the previous section, we will decompose space-time at large scales as

$$\mathcal{M} = \mathbb{R} \times \Sigma_3 \tag{2.1}$$

$$ds^2 = -dt^2 + a^2(t) \left(\gamma_{ij, \text{Thurston}} dx^i dx^j \right), \tag{2.2}$$

where $\gamma_{ij, \text{Thurston}}$ is specific to each of the eight geometries of this theorem.

The spatial part contains a real-valued curvature parameter κ that distinguishes between positive ($\kappa > 0$), zero ($\kappa = 0$) and negative ($\kappa < 0$) curvature. This parameter also defines a length scale, the radius of curvature, which can be written as $L = 1/\sqrt{\kappa}$ for geometries with positive curvature, $L = 1/\sqrt{-\kappa}$ for those with negative curvature, and in the zero curvature case $L \rightarrow \infty$ as κ approaches zero. We will use the curvature parameter κ and curvature radius L interchangeably in this text.

⁷Nevertheless, from the phenomenological point of view, it is worth investigating the signatures of topology of the Universe and confront them with the data. In fact, there is a large body of work mentioned above and doing precisely that, for reviews see Refs. [33, 34, 35, 4, 5, 36]. All of these works assume that the geometry of the spatial section is flat, *i.e.* $\Sigma_3 = \mathbb{R}^3$. The question of how topology may affect the analyses performed in this work is not something we will address in this work. Needless to say, this would be a natural question to investigate.

2.1 The FLRW geometries, \mathbb{R}^3 , \mathbb{H}^3 and \mathbb{S}^3

The first three Thurston geometries, \mathbb{R}^3 , \mathbb{H}^3 and \mathbb{S}^3 , are the only isotropic geometries in Thurston's classification. They are, of course, exactly the spatial slices of the familiar FLRW space-time. We can parameterise all three simultaneously in hyperspherical coordinates as follows.

$$ds^2 = -dt^2 + a^2(t) \left(d\chi^2 + S_\kappa^2(\chi) d\Omega^2 \right) = -dt^2 + a^2(t) \left(d\chi^2 + S_\kappa^2(\chi) (d\theta^2 + \sin^2(\theta) d\phi^2) \right), \quad (2.3)$$

$$S_\kappa(\chi) = \begin{cases} \sin(\chi\sqrt{\kappa})/\sqrt{\kappa} & \text{if } \kappa > 0 \\ \chi & \text{if } \kappa = 0 \\ \sinh(\chi\sqrt{-\kappa})/\sqrt{-\kappa} & \text{if } \kappa < 0 \end{cases} \quad (2.4)$$

$$= \begin{cases} L \sin(\chi/L) & \text{if } \kappa > 0 \\ \chi & \text{if } \kappa = 0 \\ L \sinh(\chi/L) & \text{if } \kappa < 0, \end{cases} \quad (2.5)$$

where $\chi \in [0, \infty)$, $\theta \in [0, \pi)$ and $\phi \in [0, 2\pi)$. The coordinate χ measures comoving distance along a radial geodesic and the angles θ and ϕ are the polar and azimuthal angles, respectively.

2.2 $\mathbb{R} \times \mathbb{H}^2$ and $\mathbb{R} \times \mathbb{S}^2$

The next two geometries, $\mathbb{R} \times \mathbb{H}^2$ and $\mathbb{R} \times \mathbb{S}^2$, are the first anisotropic spaces of Thurston's classification schema. We can think of the resulting space-time as an FLRW space-time of two dimensions, together with a third dimension that is flat. The resulting space is still homogeneous, but is anisotropic due to this special direction. We will therefore present them using hyperspherical coordinates of one dimension lower, with a free coordinate z .

$$ds^2 = -dt^2 + a^2(t) \left(dz^2 + d\chi^2 + S_\kappa^2(\chi) d\phi^2 \right). \quad (2.6)$$

Here $\chi \in [0, \infty)$ and $\phi \in [0, 2\pi)$ as before; but rather than including a polar angle θ , we instead have a real coordinate $z \in \mathbb{R}$ orthogonal to the (χ, ϕ) plane. The parameter κ again distinguishes between positive and negative curvature through S_κ , defined in (2.4).

2.3 $\widetilde{\mathbb{U}(\mathbb{H}^2)}$

The sixth Thurston geometry, $\widetilde{\mathbb{U}(\mathbb{H}^2)}$, is the universal cover of the unit tangent bundle of the hyperbolic plane. To derive its metric we will mostly follow the derivation of Fagundes in [47] and begin with the following metric of \mathbb{H}^2 .

$$d\Sigma_{\mathbb{H}^2}^2 = dx^2 + \cosh^2(x) dy^2. \quad (2.7)$$

A unit tangent vector $\hat{u}_p \in \mathbb{U}_p(\mathbb{H}^2)$ at any point $p = (x, y) \in \mathbb{H}^2$ must now satisfy $\hat{u}_p \cdot \hat{u}_p = 1$. This means we can write $\hat{u}_p = \left(\cos(\phi), \frac{\sin(\phi)}{\cosh(x)} \right)$, with $0 \leq \phi < 2\pi$. For a small displacement dp^i we can calculate the total differential,

$$Du^i = \left(\frac{\partial u^i}{\partial p^k} + \Gamma_{jk}^i u^j \right) dp^k + \frac{\partial u^i}{\partial \phi} d\phi, \quad (2.8)$$

where $i, j, k \in \{1, 2\}$, $p^1 = x$ and $p^2 = y$. The nonzero Christoffel symbols obtained from (2.7) are $\Gamma_{22}^1 = -\sinh(x) \cosh(x)$ and $\Gamma_{12}^2 = \Gamma_{21}^2 = \tanh(x)$. Therefore we get

$$D\hat{u}^1 = -\sinh(x) \sin(\phi) dy - \sin(\phi) d\phi \quad (2.9)$$

$$D\hat{u}^2 = +\tanh(x) \cos(\phi) dy + \frac{\cos(\phi)}{\cosh(x)} d\phi. \quad (2.10)$$

The length of $D\hat{u}$ is then given by $(D\hat{u}^1)^2 + (D\hat{u}^2)^2 \cosh^2(x)$, so that the metric on $\mathbb{U}(\mathbb{H}^2)$ can be written as:

$$d\Sigma_{\mathbb{U}(\mathbb{H}^2)}^2 = dx^2 + \cosh^2(x) dy^2 + (D\hat{u}^1)^2 + (D\hat{u}^2)^2 \cosh^2(x) \quad (2.11)$$

$$= dx^2 + \cosh^2(x) dy^2 + (d\phi + \sinh(x) dy)^2. \quad (2.12)$$

Note that the topology of $U(\mathbb{H}^2)$ is homeomorphic to the Cartesian product of the 2-plane with the circle. This means that this space is path-connected, but not simply-connected: there are loops that wind around ϕ that cannot be shrunk to a point. Taking the universal cover of $U(\mathbb{H}^2)$ means that we must ‘unroll’ the circle \mathbf{S} to a line by promoting the angle ϕ to a real variable z . Since the metric in (2.11–2.12) does not contain a length scale, we will introduce it by setting $x \rightarrow x\sqrt{-\kappa} = x/L$ in the argument of the hyperbolic functions.

The (identity component of the) $\widetilde{U(\mathbb{H}^2)}$ space-time can then be presented as $\mathbb{R}^{1,3}$ with the following metric:

$$ds^2 = -dt^2 + a^2(t) \left(dx^2 + \cosh^2(x\sqrt{-\kappa})dy^2 + (dz + \sinh(x\sqrt{-\kappa})dy)^2 \right) \quad (2.13)$$

$$= -dt^2 + a^2(t) \left(dx^2 + \cosh^2(x/L)dy^2 + (dz + \sinh(x/L)dy)^2 \right). \quad (2.14)$$

2.3.1 A sidenote on $\widetilde{SL(2, \mathbb{R})}$

In literature, $\widetilde{U(\mathbb{H}^2)}$ is often used interchangeably with $\widetilde{SL(2, \mathbb{R})}$ in the context of the geometrization theorem. This identification is sensible in a topology or differential geometry context, as $SL(2, \mathbb{R})$ acts naturally on \mathbb{H}^2 by way of a Möbius transformation. This action can be extended to $U(\mathbb{H}^2)$ through the tangent map, which induces a diffeomorphism between the two manifolds. However, this diffeomorphism is *not* an isometry. To see this, recall the definition of $SL(2, \mathbb{R})$,

$$SL(2, \mathbb{R}) = \left\{ \begin{pmatrix} a & b \\ c & d \end{pmatrix} \mid a, b, c, d \in \mathbb{R} \ \& \ ad - bc = 1 \right\}, \quad (2.15)$$

and parameterise any 2-dimensional real matrix g as

$$g = \begin{pmatrix} a & b \\ c & d \end{pmatrix} = \begin{pmatrix} X_1 + X_3 & X_4 + X_2 \\ X_4 - X_2 & X_1 - X_3 \end{pmatrix} \quad (2.16)$$

with $X_i \in \mathbb{R}$. For g to be in $SL(2, \mathbb{R})$ it must hold that $X_1^2 + X_2^2 - X_3^2 - X_4^2 = \det(g) = 1$. In other words, $SL(2, \mathbb{R})$ can be constructed as a unit (hyper)sphere in $\mathbb{R}^{(2,2)}$. The metric on $SL(2, \mathbb{R})$ can then be induced from the ambient space $\mathbb{R}^{(2,2)}$ by using the Iwasawa decomposition and we can take similar steps to the derivation above to pass to the universal cover and restore a length scale L . We then get the following metric,

$$ds = -dt^2 + a^2(t) (dx^2 + dy^2 - dz^2 + 2\sinh(2x\sqrt{-\kappa})dydz) \quad (2.17)$$

$$= -dt^2 + a^2(t) (dx^2 + dy^2 - dz^2 + 2\sinh(2x/L)dydz). \quad (2.18)$$

Note that dz^2 has a minus sign in this expression, as the spatial section has inherited a $(+, +, -)$ signature from the metric of $\mathbb{R}^{(2,2)}$. This shows that $SL(2, \mathbb{R})$ is not locally Euclidean and so cannot be isometric to $U(\mathbb{H}^2)$. For the purposes of this paper we will therefore refrain from identifying these two spaces.

2.4 Nil and Solv

The last two geometries, Nil and Solv, are hyperbolic geometries ($\kappa < 0$) that are the geometries of a Lie group. Nil can be described as the geometry of the Heisenberg group, while Solv can be described as the geometry of the identity component of the 2-dimensional Poincaré group. There are standard ways of presenting these manifolds as \mathbb{R}^3 endowed with a special metric.

In the case of Nil, the space-time can be presented as,

$$ds^2 = -dt^2 + a^2(t) \left(dx^2 + (1 - \kappa x^2)dy^2 + dz^2 - 2x\sqrt{-\kappa} dydz \right) \quad (2.19)$$

$$= -dt^2 + a^2(t) \left(dx^2 + (1 + x^2/L^2)dy^2 + dz^2 - 2x/L dydz \right). \quad (2.20)$$

The space-time based on Solv can be presented as,

$$ds^2 = -dt^2 + a^2(t) \left(e^{2z\sqrt{-\kappa}}dx^2 + e^{-2z\sqrt{-\kappa}}dy^2 + dz^2 \right) \quad (2.21)$$

$$= -dt^2 + a^2(t) \left(e^{2z/L}dx^2 + e^{-2z/L}dy^2 + dz^2 \right), \quad (2.22)$$

with $x, y, z \in \mathbb{R}$, $\kappa < 0$ and $L > 0$. Note that the Solv metric is diagonal, while that of Nil is not.

Finally, we note that the $\widetilde{U(\mathbb{H}^2)}$ (2.13) and Nil (2.19) geometries contain off-diagonal terms, signifying a twist and deformation of the yz -plane, see also Figures 34–39 from the appendix. To get an idea of the size of the deformation, one can diagonalize these geometries by performing x -dependent rotations (which are *not* coordinate transformations). The eigenvalues in these local diagonal frames are *e.g.* for Nil: 1 in the x -direction and $1 - \kappa x^2 \pm x\sqrt{-\kappa}\sqrt{1 - \kappa x^2}$ in the yz -plane, implying that (at short distances) the contraction/dilation along the principal axes in the yz -plane grows as $\sim \pm x\sqrt{-\kappa} = \pm x/L$.

3 Background Evolution

In this section we will derive the evolution of the cosmological background for each of the space-times. It will turn out that the evolution of all eight Thurston space-times is very similar to the evolution of the first three space-times, which we recall are the ordinary FLRW cases. This is because the metrics in equations (2.3), (2.6), (2.13), (2.19) and (2.21) presented in the previous section all admit a very similar Einstein tensor:

$$G^\mu{}_\nu = -\text{diag}\left(3\frac{\dot{a}}{a}, \frac{\dot{a} + 2\ddot{a}a}{a^2}, \frac{\dot{a} + 2\ddot{a}a}{a^2}, \frac{\dot{a} + 2\ddot{a}a}{a^2}\right) + \frac{\kappa}{a^2}\text{diag}\left(K^{(0)}, K^{(1)}, K^{(2)}, K^{(3)}\right). \quad (3.1)$$

Here $K^{(0)}, K^{(1)}, K^{(2)}$ and $K^{(3)}$ are a set of four parameters⁸ specific to each Thurston geometry that determine how strongly terms in the energy-momentum tensor are coupled to the curvature parameter κ . This makes the calculation fairly straightforward, as we can leave these parameters implicit to solve for all geometries simultaneously.

The Nil and $\widetilde{U(\mathbb{H}^2)}$ geometries are slightly more complicated in that their Einstein tensor has an additional nonzero off-diagonal term.

$$G^3{}_{2,\text{Nil}} = x\sqrt{-\kappa}\frac{\kappa}{a} \quad (3.2)$$

$$G^3{}_{2,\widetilde{U(\mathbb{H}^2)}} = 2\sinh(x\sqrt{-\kappa})\frac{\kappa}{a}. \quad (3.3)$$

For all geometries, the Ricci scalar takes the form

$$R = 6\frac{a\ddot{a} + \dot{a}^2}{a^2} - 2K^{(0)}\frac{\kappa}{a^2}. \quad (3.4)$$

This expression is devoid of any coordinates, which confirms that the Thurston space-times are indeed homogeneous – despite this not being immediately manifest from their metric representation. This means that we are free to choose the origin of our coordinate system. We will exploit this in later sections to simplify calculations.

3.1 General solution

The most general fluid solution compatible with this Einstein tensor is:

$$T^\mu{}_\nu = \rho u^\mu u_\nu + p \delta^\mu{}_\nu + \pi^\mu{}_\nu, \quad (3.5)$$

where $\rho = \rho(t)$ and $p = p(t)$ denote the fluid energy density and pressure, respectively $u^\mu = u^\mu(t)$ is the velocity vector of the fluid and $\pi_\nu{}^\mu$ is the shear tensor, which is symmetric, $\pi^\mu{}_\nu = \pi_\nu{}^\mu$, traceless, $\pi^\mu{}_\mu = 0$, and transverse, $\pi^\mu{}_\nu u^\nu = 0$. Clearly the *Ansatz* (3.5) goes beyond the perfect fluid *Ansatz* of the standard Friedmann geometries, for which the shear tensor vanishes. In section 6 we consider an alternative approach where we set $\pi^\mu{}_\nu = 0$, but allow for anisotropic expansion rates.

We now consider the Einstein equation in the rest frame of this fluid, where $u^\mu = (1, 0, 0, 0)$. This yields a slight modification of the familiar Friedmann equations,

$${}^0_0 \text{ equation:} \quad H^2 = \frac{8\pi G}{3}\rho + \frac{\Lambda}{3} + \frac{\kappa K^{(0)}}{3a^2} \quad (3.6)$$

$${}^i_i \text{ equation:} \quad \frac{\ddot{a}}{a} = -\frac{4\pi G}{3}(\rho + 3p) + \frac{\Lambda}{3} + \frac{\kappa}{a^2}\left(\frac{K^{(i)}}{2} - \frac{K^{(0)}}{6}\right) - 4\pi G\pi^i{}_{\hat{i}}. \quad (3.7)$$

⁸We have used round brackets around the indices to indicate that these are a set of parameters and not a vector.

There is no summation over repeated indices carrying hats in the equations in this section. We have omitted the $\hat{i} \hat{j}$ equation for $\hat{i} \neq \hat{j}$; for all geometries except Nil and $\widehat{U(\mathbb{H}^2)}$ this reads $\pi^{\hat{i} \hat{j}} = 0$ for $\hat{i} \neq \hat{j}$, except for $\pi^3_{2,}$ in which case one gets,

$$\pi^3_{2,\text{Nil}} = x\sqrt{-\kappa} \frac{\kappa}{8\pi G a^2} \quad (3.8)$$

$$\pi^3_{2,\widehat{U(\mathbb{H}^2)}} = 2 \sinh(x\sqrt{-\kappa}) \frac{\kappa}{8\pi G a^2}. \quad (3.9)$$

Therefore these off-diagonal stresses are suppressed when compared with the diagonal components π^i_i by a factor $\sim x\sqrt{-\kappa} = x/L$, which is much smaller than unity on distances small in comparison to the curvature radius, *i.e.* $|x| \ll L$. This suggests that their contribution to the dynamics of the Universe (in the local Hubble patch) is much smaller than that of the diagonal components, and can therefore be – to the leading approximation – neglected.

The right-hand side of (3.7) has terms containing the (fixed) spatial index \hat{i} , however the left-hand side does not. This means that all index-carrying terms on the right-hand side must be the same, independent of the choice of index \hat{i} . Therefore for all \hat{i}, \hat{j} it must hold that:

$$8\pi G a^2 \pi^{\hat{i}}_{\hat{i}} - \kappa K^{(\hat{i})} = 8\pi G a^2 \pi^{\hat{j}}_{\hat{j}} - \kappa K^{(\hat{j})} \quad (3.10)$$

Since π is traceless, we can solve for its diagonal elements,

$$\pi^{\hat{i}}_{\hat{i}} = \frac{\kappa}{24\pi G a^2} \left(2K^{(\hat{i})} - \sum_{\hat{j} \neq \hat{i}} K^{(\hat{j})} \right). \quad (3.11)$$

This can be used to rewrite the second Friedmann-like equation (3.7) into a more complete form,

$$\frac{\ddot{a}}{a} = -\frac{4\pi G}{3}(\rho + 3p) + \frac{\Lambda}{3} + \frac{\kappa}{6a^2} \left(-K^{(0)} + K^{(1)} + K^{(2)} + K^{(3)} \right). \quad (3.12)$$

When we plug in the values for the K -parameters, it will turn out that the last term in this equation, $-K^{(0)} + K^{(1)} + K^{(2)} + K^{(3)}$, vanishes for all of the Thurston space-times and so (3.12) reduces to the ordinary form of the second Friedmann equation. We obtain the evolution of ρ directly by differentiating (3.6) with respect to time

$$2H \left(\frac{\dot{a}}{a} - H^2 \right) = \frac{8\pi G}{3} \dot{\rho} - 2H \frac{K^{(0)} \kappa}{3a^2}. \quad (3.13)$$

Using (3.6) and (3.12), we can rewrite this as,

$$\dot{\rho} + 3H(\rho + p) = \frac{\kappa H}{8\pi G a^2} \left(-K^{(0)} + K^{(1)} + K^{(2)} + K^{(3)} \right) = 0. \quad (3.14)$$

3.2 Friedmann Equations

Let's now consolidate the equations from the previous section into the following set:

$$\textbf{Friedmann I:} \quad H^2 = \frac{8\pi G}{3} \rho + \frac{\Lambda}{3} + \frac{\kappa K^{(0)}}{3a^2} \quad (3.15)$$

$$\textbf{Friedmann II:} \quad \frac{\ddot{a}}{a} = -\frac{4\pi G}{3}(\rho + 3p) + \frac{\Lambda}{3} \quad (3.16)$$

$$\textbf{Energy Evolution:} \quad 0 = \dot{\rho} + 3H(\rho + p) \quad (3.17)$$

$$\textbf{Shear Constraints I:} \quad \pi^{\hat{i}}_{\hat{i}} = \frac{\kappa}{24\pi G a^2} \left(2K^{(\hat{i})} - \sum_{\hat{j} \neq \hat{i}} K^{(\hat{j})} \right) \quad (3.18)$$

$$\textbf{Shear Constraints II:} \quad \pi^3_{2,\text{Nil}} = x\sqrt{-\kappa} \frac{\kappa}{8\pi G a^2}, \quad \pi^3_{2,\widehat{U(\mathbb{H}^2)}} = 2 \sinh(x\sqrt{-\kappa}) \frac{\kappa}{8\pi G a^2} \quad (3.19)$$

The first three of these equations tell us that the last five (anisotropic) Thurston space-times admit Friedmann equations that are of the same form as the first three (isotropic) cases. Importantly, the space-times based on Thurston geometries admit the usual matter, radiation, and dark energy or cosmological constant contributions as constituents of the universe that we are used to from ordinary FLRW space-time. The only difference is that the strength of the curvature contribution to the energy density is determined by the parameter $K^{(0)}$, which varies between geometries and is given in Table 1. Aside from this difference, many of the standard analyses apply as *e.g.* we can solve the

Space-Time	$K^{(0)}$	$K^{(1)}$	$K^{(2)}$	$K^{(3)}$	$8\pi G a^2 \pi^1_{1/\kappa}$	$8\pi G a^2 \pi^2_{2/\kappa}$	$8\pi G a^2 \pi^3_{3/\kappa}$	$8\pi G a^2 \pi^3_{2/\kappa}$
FLRW	-3	-1	-1	-1	0	0	0	0
$\mathbb{R} \times \mathbb{H}^2/\mathbb{S}^2$	-1	0	0	-1	1/3	1/3	-2/3	0
$\widetilde{\mathbb{U}(\mathbb{H}^2)}$	-5/4	1/4	1/4	-7/4	2/3	2/3	-4/3	$-2 \sinh(x\sqrt{-\kappa})$
Nil	-1/4	1/4	1/4	-3/4	1/3	1/3	-2/3	$x\sqrt{-\kappa}$
Solv	-1	-1	-1	1	-2/3	-2/3	4/3	0

Table 1: Several parameters for the Thurston space-times.

flatness problem by the usual means we are familiar with from FLRW Cosmology.

However, the last two equations tell us that this comes at the cost of picking up one or two additional constraints from the Einstein field equations on the shear tensor π that must be satisfied in order for these standard analyses to apply (see also Table 1). One might imagine solving this on the matter side of the Einstein field equations by introducing some exotic, anisotropic fluid that has the correct $\propto a^{-2}$ scaling properties. However, this approach creates more problems than it solves. Firstly, one would have to come up with a candidate fluid whose energy density scales appropriately as $\propto a^{-2}$ to make up this exotic fluid. Secondly, one would have to propose a mechanism by which this fluid exerts pressure anisotropically and explain why this is fine-tuned to exactly satisfy the Shear Constraints (3.18)–(3.19). Thirdly, since we now have a second energy contribution that scales as $\propto a^{-2}$, curvature being the first, we are introducing an additional contribution to the evolution of a in equations (3.15)–(3.16); this means must extend the *flatness problem* and find not only an explanation for why the primordial curvature density is very close to zero, but also why the same is the case for the primordial energy density this exotic fluid.

Instead, we will opt to solve this on the geometry side of the Einstein field equations in Section 6 by introducing anisotropies in the scale factor. This alternative approach allows us to solve the Friedmann equations using a perfect fluid *Ansatz* at the cost of picking up anisotropies in expansion of the space-time, which grow (decay) in decelerating (accelerating) space-times, suggesting inflation as the natural solution both for the flatness and anisotropy problems. With this in mind, one can assume anisotropies to be small throughout the expansion history of the Universe.

The Nil and $\widetilde{\mathbb{U}(\mathbb{H}^2)}$ space-times remain an exception, as their π^3_2 terms cannot be absorbed into anisotropies in the scale factor. However, this term is additionally suppressed by x/L (see Table 1), which is much less than unity on sub-Hubble scales. Since this will be observationally small compared to other curvature terms in the energy-momentum tensor, we will ignore this term in the dynamics of the Universe.

3.3 Length scales

As a last topic in this section, we will calculate several length scales; these will be used to generate the plots in Section 5. In particular, we are interested in the inherent curvature radius L of the geometry and in η_* , the conformal time until the last scattering surface.

To this end, we introduce $\rho_\Lambda = \Lambda/(8\pi G)$ and $\rho_\kappa = K^{(0)}/(8\pi G a^2)$ to put the cosmological constant and curvature on the same footing as the other matter contents of the Universe. We can use this to rewrite (3.15) in terms of energy densities,

$$H^2 = \frac{8\pi G}{3} (\rho_{\text{matter}} + \rho_\Lambda + \rho_\kappa). \quad (3.20)$$

By setting $\rho_i(t) = \rho_i(0)a(t)^{-2\epsilon_i}$ ($i = \text{matter}, \Lambda, \kappa$), where ϵ_i denotes the slow roll parameter associated with the fluid i and is defined as $\epsilon_i = -\dot{H}/H^2$ if that fluid would dominate the energy content of the Universe, we can re-express Eq. (3.20) in terms of fractions of the present critical energy density $\Omega_{i,0} = \rho_{i,0}/\rho_{\text{crit},0}$ as,

$$H^2(t) = \frac{8\pi G}{3} \sum_i \frac{\rho_{i,0}}{a(t)^{2\epsilon_i}} = H_0^2 \sum_i \frac{\Omega_{i,0}}{a(t)^{2\epsilon_i}} = H_0^2 \sum_i \Omega_{i,0} (1+z(t))^{2\epsilon_i}, \quad (3.21)$$

where $z(t)$ is the redshift, $H_0^2 = \frac{8\pi G}{3} \rho_{\text{crit},0}$ denotes the expansion rate today and $\rho_{\text{crit},0}$ is the total energy density supporting it. Assuming the Universe has a matter, radiation, curvature and cosmological constant (dark energy) component, we can derive an integral expression for the (conformal) time between two events,

$$\eta = \int_{\eta_1}^{\eta_2} d\eta' = \int_{t_1}^{t_2} \frac{dt}{a} = \int_{a_1}^{a_2} \frac{da}{a^2 H(a)} = \frac{1}{H_0} \int_{a_1}^{a_2} \frac{da}{(\sum_i \Omega_{i,0} a^{4-2\epsilon_i})^{1/2}}. \quad (3.22)$$

This is an elliptic integral that does not admit an easy analytical solution in terms of elementary functions [48, 49]. Fortunately, we will not need a full analytical solution for (3.22) and we can instead compute the integral numerically by plugging in the relevant observed values.

Next, we calculate the effective curvature length scale from equations (3.15) and (3.21),

$$\Omega_\kappa = \frac{K^{(0)}_\kappa}{3H^2 a^2} \Leftrightarrow \kappa = \frac{3H^2 a^2 \Omega_\kappa^{(0)}}{K} \Leftrightarrow L = \frac{1}{aH} \sqrt{\left| \frac{K^{(0)}}{3\Omega_\kappa} \right|}. \quad (3.23)$$

To get a sense of the largest-scale of observable effects in the next chapter, we will calculate η_* , the conformal time to the surface of last scattering at $z_* \simeq 1091$, $a_* \simeq 1/1092$ in terms of the inherent curvature length scale L of the underlying 3-manifolds,⁹

$$\eta_* = L \sqrt{\left| \frac{3\Omega_{\kappa,0}}{K^{(0)}} \right|} \int_{a_*}^1 \frac{1}{\sqrt{\Omega_{\Lambda,0} a^4 + \Omega_{\kappa,0} a^2 + \Omega_{m,0} a + \Omega_{R,0}}} da. \quad (3.24)$$

We now evaluate the integral using numerical values from the 2018 Planck Results [25] in Table 2.

	$\Omega_{\Lambda,0}$	$\Omega_{\kappa,0}$	$\Omega_{R,0} = \Omega_{m,0}/(1+z_{eq})$	$\Omega_{m,0}$
Pure CMB constraints	0.6834 ± 0.0084	$-0.0440_{-0.015}^{+0.018}$	$(9.29 \pm 0.25) \cdot 10^{-5}$	0.3166 ± 0.0084
CMB + Lensing	0.6847 ± 0.0073	-0.0406 ± 0.0065	$(9.31 \pm 0.18) \cdot 10^{-5}$	0.3153 ± 0.0073
CMB + Lensing + BAO	0.6889 ± 0.0056	$+0.0007 \pm 0.0019$	$(9.18 \pm 0.17) \cdot 10^{-5}$	0.3111 ± 0.0056

Table 2: Cosmological parameters from [25].

It is worth reflecting that these constraints were obtained from observations assuming an isotropic model; we have no reason to believe they would stay the same if we assumed an anisotropic model instead. However, the proper statistical analysis for the Thurston geometries is beyond the scope of this paper, so we will work with the constraints given in Table 2 for the moment.

We will use the average values for $\Omega_{\Lambda,0}$, $\Omega_{R,0}$ and $\Omega_{m,0}$ and we will take the two standard deviations (2σ) bounds on $\Omega_{\kappa,0}$ from CMB + Lensing + BAO. We arrive at $\Omega_{\kappa,0} = 0.0007 + 2 \times 0.0019 = 0.0045$ for negatively curved geometries and $\Omega_{\kappa,0} = 0.0007 - 2 \times 0.0019 = -0.0031$ for positively curved geometries.¹⁰ The resulting values are shown in Table 3, with Table 4 contrasting the values from CMB constraints only.

Space-Time	Ω_κ	$\eta_* H_0$	LH_0	η_*/L
\mathbb{R}^3	0	3.133	∞	0
\mathbb{H}^3	0.0045	3.136	17.96	0.175
\mathbb{S}^3	-0.0031	3.138	14.91	0.210
$\mathbb{R} \times \mathbb{H}^2$	0.0045	3.136	10.37	0.302
$\mathbb{R} \times \mathbb{S}^2$	-0.0031	3.128	8.61	0.363
$\widetilde{\mathbb{U}(\mathbb{H}^2)}$	0.0045	3.136	11.59	0.271
Nil	0.0045	3.136	5.18	0.605
Solv	0.0045	3.136	10.37	0.302

Table 3: Length Scales conforming to the 2σ observational bounds, $-0.0031 \leq \Omega_\kappa \leq 0.0045$ from CMB + Lensing + BAO.

Space-Time	Ω_κ	$\eta_* H_0$	LH_0	η_*/L
\mathbb{R}^3	0	3.111	∞	0
\mathbb{H}^3				
\mathbb{S}^3	-0.074	3.125	8.45	0.37
$\mathbb{R} \times \mathbb{H}^2$				
$\mathbb{R} \times \mathbb{S}^2$	-0.074	3.125	4.88	0.64
$\widetilde{\mathbb{U}(\mathbb{H}^2)}$				
Nil				
Solv				

Table 4: The same scales based on the 2σ bounds from CMB, $-0.074 \leq \Omega_\kappa \leq -0.08$. Since κ is strictly positive for these bounds, hyperbolic spaces are left blank.

⁹ L coincides with the physical curvature radius at present. For earlier times, the physical curvature radius can be expressed as the invariant spatial distance $a(t)L$, but this will not be used in this paper.

¹⁰It is worth noting that the constraints on Ω_κ are significantly less strong on the first two rows of Table 2, for which Ω_κ is strictly negative ($\kappa > 0$) within the 2σ bounds. As only the $\mathbb{R} \times \mathbb{S}^2$ geometry is anisotropic and positively curved, this would significantly limit the scope of the paper, see Table 4, unless one would include broader confidence limits ($> 3\sigma$). Hence we have opted for the constraints that allow for both positively and negatively curved spaces.

If one were to instead allow for both strongly negatively and positively curved space-times, the assumption that proper distance λ is small compared to the curvature radius L would start to break down for distances comparable to the Hubble scale. This would necessitate the inclusion of increasingly higher-order contributions, until the power expansion breaks down entirely. Since the plots in Section 5 are generated through a power series in η_*/L , one would expect contributions at higher order to become increasingly important, which has a potential to change these plots dramatically. Lastly, we would similarly expect that topological considerations will become markedly more important in this regime, as *e.g.* boundary conditions of the Thurston patches will no longer be hidden behind the Hubble horizon.

These tables tell us two important things. Firstly, it tells us that L larger than η_* (by about half an order of magnitude for most geometries), which means that we can expand complicated expressions in powers of η_*/L to get approximate results. This will be very useful in Section 5, as we are not able to find exact expressions for all geometries.

Secondly, and perhaps more importantly, the curvature radius L is larger than the Hubble radius H_0^{-1} for all Thurston geometries. This allows us to substantiate the following assumption: If spatial sections of our Universe are well-described by a patchwork of Thurston geometries, then the Hubble sphere – and moreso Earth’s low-redshift surroundings – are very likely to belong only a single of these patches. As a result, we argue that any detectable effects of anisotropy are similarly likely to be sourced by a single geometry.

Under this assumption we can start to make predictions about how our Universe would look if we took any one of the eight Thurston-Perelman geometries as our local spatial section and our Universe were indeed curved and anisotropic. In the next section we will discuss two ways in which these effects may become manifest.

4 Distance Measures

Since our chosen constraints put the curvature radius as significantly larger than the size of the observable universe, we likely stand no chance of devising a local experiment that is sensitive enough to detect curvature anisotropy. Rather, we must look for the effects of anisotropy over very long distances or in very large-scale phenomena. We propose to use photon trajectories for this purpose, as they are bent by the presence of curvature and thus directly affected by the anisotropies in the metric. The farther a photon travels, the more apparent any deflection in its trajectory will be, so we expect any effects to be magnified for higher redshifts.

Anisotropic curvature will behave like a large lens that deforms the image of distant objects. The magnitude and shape of this deformation will depend on the position of the object in the night sky in a way that is unique to each of our geometries. This pattern of deformations can serve as a fingerprint by which we can identify a geometry.

In this section, we will derive expressions for these deformations by considering the angular diameter distance d_A , which is affected by the deformations directly, and the luminosity distance d_L , which is affected by the net change in apparent luminosity. In the next section, we will present several figures to visualise this effect for each geometry.

Plotting these distance measures will require us to derive null geodesics for each of the Thurston space-times. Fortunately, this becomes a very tractable problem when we transform Eq. (1.2) to conformal time:

$$0 = ds^2 = -dt^2 + a^2(t)d\Sigma_3^2 = a^2(t)\left(-d\eta^2 + d\Sigma_3^2\right), \quad (d\Sigma_3^2 = \gamma_{ij,\Sigma} dx^i dx^j). \quad (4.1)$$

This equation has the implicit solution $d\eta^2 = d\Sigma_3^2$,¹¹ which reduces the problem to a 3-dimensional one. That is to say, if we can find some spatial geodesic $x^i(\lambda)$ parameterised by proper distance λ on Σ_3 , then $(\eta, x^i(\eta))$ is a geodesic in the full Thurston space-time parameterised by conformal time η . Finding these spatial geodesics is further simplified by the fact that the manifolds in Thurston’s theorem are homogeneous and, as explained in Section 3, we are at liberty to place the observer at the origin of the coordinate system and to consider only radial geodesics. We will leave the derivation of such geodesics to the appendices and assume for the rest of this section that they are known.

Rigorously speaking the analysis in this section applies to rigid geometries. To capture the dynamical aspects of various Thurston geometries discussed in detail in section 6, one would have to suitably modify the analysis of this section. However, we will show later in Section 6 that geometries evolve rather slowly, so that the results derived in this section will apply to most of the situations of interest.

4.1 Distance measures in an isotropic universe

In FLRW space-time, calculating both distance measures is straightforward due to spherical symmetry on spatial slices.

4.1.1 Angular diameter distance

Angular diameter distance d_A can be defined as the ratio of an object’s physical size h at the time of emission, to the object’s apparent angular size $\delta\omega$ as viewed from the observer. In essence, it is the answer to the question, ‘in a flat universe, how far away would an object of a known size need to be in order to appear as large as it does?’

¹¹Given that $d\Sigma_3^2$ depends on spatial variables only, Eq. (4.1) implies that conformal time is a good affine parameter along geodesics, and can be used to parametrize geodesic distances on Σ_3 . Rigorously speaking this ceases to be the case when anisotropic expansion rates are considered, in which case $d\Sigma_3^2$ becomes dynamical (see section 6 for more details).

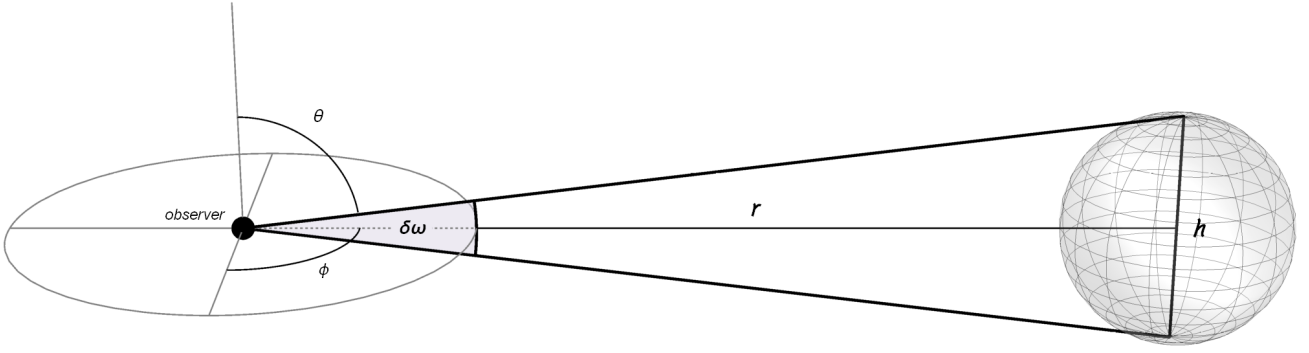


Figure 1: Angular Diameter Distance in FLRW space-time

Due to spatial isotropy, we may choose a spherical coordinate system so that the object, which we will assume to be spherical itself,¹² lies along the equator at coordinate-distance r . Again exploiting isotropy, we can decide to measure the angular diameter along an arc that lies in the (r, θ) -plane, as in Figure 1. Assuming that the angular size $\delta\omega$ of the object is small, we may write

$$d_{A, \text{FLRW}} = \frac{h}{\delta\omega} = \frac{a r \tan(\delta\omega)}{\delta\omega} \approx \frac{a r \delta\omega}{\delta\omega} = ar = aS_{\kappa}(\chi), \quad (4.2)$$

where the a in this equation and in the rest of this section is taken at the time of emission of the photon, and for the scale factor today we take, $a_0 = a(t_0) = 1$.

4.1.2 Luminosity distance

Luminosity distance d_L can be defined through a relationship between the intrinsic luminosity \mathcal{L} (in Js^{-1}) of a distant source and the observed flux f (in $\text{Jm}^{-2}\text{s}^{-1}$) as measured by an observer on Earth,

$$f = \frac{\mathcal{L}}{4\pi d_L^2} \quad \longleftrightarrow \quad d_L = \sqrt{\frac{\mathcal{L}}{4\pi f}}. \quad (4.3)$$

In essence, it answers a question similar to the angular diameter distance: ‘in a flat universe, how far away would an object of known luminosity need to be to appear as bright as it does?’

In FLRW space-time, the calculation is again fairly straightforward. Since the space-time is homogenous and isotropic, light emitted from a source spreads evenly in all directions. The flux f measured by an observer at proper distance χ is simply the luminosity \mathcal{L} of the source divided by the area $4\pi S_{\kappa}^2(\chi)$ of a hypersphere with the same radius. We also need to take into account the expansion of the Universe, which will multiply the flux by a factor of a due to red-shifting of photons and another factor of a due to the expansion slowing down the rate of incoming photons,

$$f = \frac{\mathcal{L}a^2}{A_{\text{hypersphere}}} = \frac{\mathcal{L}a^2}{4\pi S_{\kappa}^2(\chi)}. \quad (4.4)$$

It follows directly from (4.3) and (4.4) that,

$$d_{L, \text{FLRW}} = \frac{S_{\kappa}(\chi)}{a}. \quad (4.5)$$

4.1.3 Etherington’s reciprocity theorem

By comparing equations (4.2) and (4.5) we see that there is a relationship between angular diameter distance and luminosity distance known as Etherington’s reciprocity theorem. Sometimes also referred to as the distance duality relation, it states simply that

$$d_L = (1+z)^2 d_A = \frac{d_A}{a^2}. \quad (4.6)$$

¹²The assumption of sphericity is convenient, but not necessary, for the derivation of Eq. (4.2). More generally, the source size can be characterised by an arc, see Figure 1, and we will adopt a more general approach in the anisotropic case.

4.2 Distance measures in an anisotropic universe

In an anisotropic setting, spherical symmetry is broken. This means that the angular diameter distance and luminosity distance will become an explicit function of the direction in which an observer is looking. Furthermore, if axial symmetry is also broken along this direction, the angular diameter distance will, in addition, depend on the orientation of the arc along which the observer measures the object's angular size. In a more general setting, these two distance measures become a quantity assigned to a particular choice of arc or solid angle, and a proper distance.

4.2.1 Angular diameter distance

In what follows we first exploit homogeneity of the Thurston-Perelman geometries to put the observer at the origin of the coordinate system. We then introduce some additional notation to parameterize arcs on the unit sphere around the observer. For a given direction $\hat{P} = (P_x, P_y, P_z)$ on the unit sphere in which we point a telescope, we can define two orthogonal unit vectors,

$$\hat{\theta} = \left(\frac{P_x P_z}{\sqrt{1 - P_z^2}}, \frac{P_y P_z}{\sqrt{1 - P_z^2}}, -\sqrt{1 - P_z^2} \right) \quad (4.7)$$

$$\hat{\phi} = \left(-\frac{P_y}{\sqrt{1 - P_z^2}}, \frac{P_x}{\sqrt{1 - P_z^2}}, 0 \right) \quad (4.8)$$

so that the triple $(\hat{P}, \hat{\theta}, \hat{\phi})$ is an orthonormal basis on \mathbb{R}^3 . We can now define any arc \mathcal{A} through \hat{P} by picking two angles, ζ and $\delta\omega$, and then writing,

$$\mathcal{A}(\hat{P}, \zeta, \delta\omega) := \{ \mathcal{G}(\hat{P}; \zeta, s) \mid \zeta = \text{fixed} \ \& \ s \in [-\delta\omega/2, \delta\omega/2] \}. \quad (4.9)$$

where \mathcal{G} characterises points on the unit sphere ¹³ through,

$$\mathcal{G}(\hat{P}; \zeta, s) = \cos(s)\hat{P} + \sin(s) \left(\cos(\zeta)\hat{\theta} + \sin(\zeta)\hat{\phi} \right). \quad (4.10)$$

Here $\delta\omega \in (0, 2\pi)$ determines the angular size of the arc and the parameter ζ specifies the orientation of the arc around the vector \hat{P} . For instance, if \hat{P} lies along the equator, then setting $\zeta = 0$ means the arc lies orthogonal to the equator, while if we set $\zeta = \pi/2$ then it lies parallel to the equator.

Now suppose that we have chosen \hat{P} and \mathcal{A} so that our telescope points at a distant object so that $\delta\omega$ coincides with the object's apparent (angular) size along the arc \mathcal{A} . In order to derive the angular diameter distance, we then want to know how the angular size $\delta\omega$ relates to the object's proper size h along this direction. In order to do this, we need to trace the rays of incoming light back to their source along this arc. However, since we can no longer assume isotropy, we cannot simply extend the initial directions specified by \mathcal{A} to a set of straight lines. Instead, we must account for the fact that the curvature of space may curve photon trajectories, as illustrated in Figure 2.

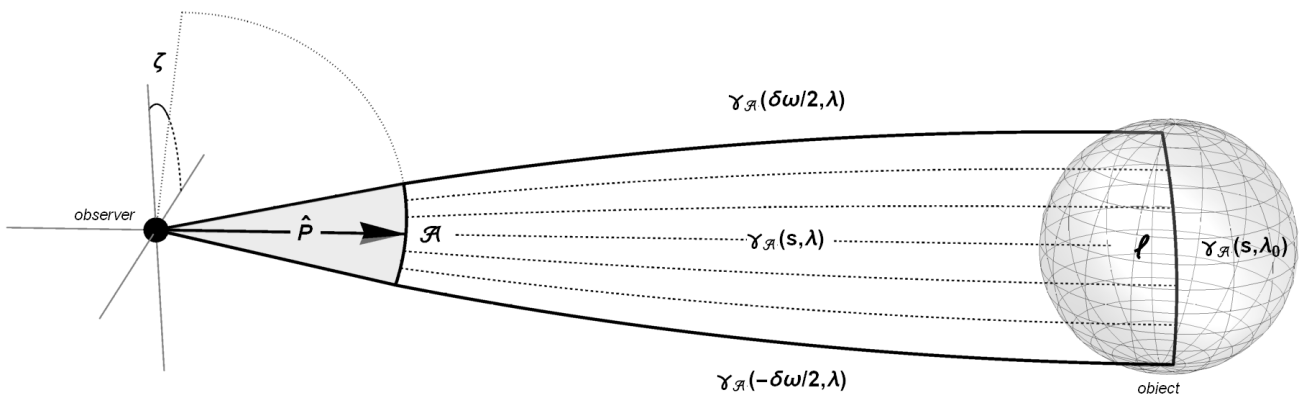


Figure 2: Angular diameter distance in an anisotropic space-time.

This means we must solve the geodesic equation for light-like (radial) geodesics with an arbitrary initial direction, which we do explicitly in Appendices A-D. For now, we assume that we know a family of geodesics $\{\gamma(\hat{P}, \lambda)\}$ characterised by

¹³Even though the coordinate frame in (4.7) and (4.8) is singular when $P_z = \pm 1$, it is more convenient for our purposes than a nonsingular frame one would obtain by *e.g.* a Gram-Schmidt procedure. The results of this section are not affected by the choice of approach.

the initial direction \hat{P} and dependent on geodesic proper distance λ along the spatial 3-manifold Σ_3 .¹⁴ The geodesics within this set is additionally assumed to satisfy,

$$\gamma(\hat{P}, 0) = 0, \quad \left. \frac{d\gamma(\hat{P}, \lambda)}{d\lambda} \right|_{\lambda=0} = \hat{P}. \quad (4.11)$$

For each choice of \hat{P} and \mathcal{A} , we can define a 1-parameter sub-family $\gamma_{\mathcal{A}}$ as,

$$\gamma_{\mathcal{A}}(s, \lambda) = \gamma(\mathcal{G}(\hat{P}; \zeta, s), \lambda), \quad (4.12)$$

where ζ is the (fixed) orientation of the arc and the angle $s \in [-\delta\omega/2, \delta\omega/2]$ parameterizes the internal angle between the initial direction of a given geodesic and the midpoint of the arc \hat{P} . By construction, the set of initial directions of this sub-family corresponds exactly to the arc \mathcal{A} , that is to say,

$$\left\{ \left. \frac{d\gamma_{\mathcal{A}}(s, \lambda)}{d\lambda} \right| s \in [-\delta\omega/2, \delta\omega/2] \ \& \ \lambda = 0 \right\} = \mathcal{A}. \quad (4.13)$$

If we now fix λ to the proper distance λ_0 of a faraway object, then the angle s traces a distant arc between opposite sides of this faraway object as we let s vary from $-\delta\omega/2$ to $\delta\omega/2$. Under the assumption that $\delta\omega$ is small compared to unity and λ_0 is small compared to L , the arc length ℓ of this distant arc multiplied by a coincides with the proper size h of the object. This means we can write,¹⁵

$$h \simeq a\ell = a \int_{-\delta\omega/2}^{\delta\omega/2} ds \sqrt{\gamma_{ij,\Sigma} \frac{d\gamma^i(\mathcal{G}(\hat{P}; \zeta, s), \lambda_0)}{ds} \frac{d\gamma^j(\mathcal{G}(\hat{P}; \zeta, s), \lambda_0)}{ds}}, \quad (4.14)$$

where a in this equation, is again understood to be the scale factor at the time of emission of the photons. Hence, for any of the Thurston space-times, the angular diameter distance of an object visible in the direction \hat{P} that sits at proper distance λ_0 measured along an arc \mathcal{A} of apparent size $\delta\omega$ and orientation ζ can be expressed as,

$$d_A(\hat{P}, \lambda_0, \delta\omega, \zeta) := a \frac{\ell}{\delta\omega} = \frac{a}{\delta\omega} \int_{-\delta\omega/2}^{\delta\omega/2} ds \sqrt{\gamma_{ij,\Sigma} \frac{d}{ds} \gamma^i(\mathcal{G}(\hat{P}; \zeta, s), \lambda_0) \frac{d}{ds} \gamma^j(\mathcal{G}(\hat{P}; \zeta, s), \lambda_0)}. \quad (4.15)$$

In the regime where $L \gg \lambda_0 \gg h$, the arc is small and far away enough that $\delta\omega$ is small compared to unity, but the curvature effects are not so strong that small deviations from the initial angle will lead to extreme differences at distance λ_0 . In this regime, the integrand in the previous equation is approximately the same for all $s \in [-\delta\omega/2, \delta\omega/2]$ and so can be approximated by a constant. This means that we can approximate the expressions for ℓ and d_A to a high degree of accuracy by,

$$\ell \simeq \delta\omega \sqrt{\gamma_{ij,\Sigma} \frac{d}{ds} \gamma^i(\mathcal{G}(\hat{P}; \zeta, s), \lambda_0) \frac{d}{ds} \gamma^j(\mathcal{G}(\hat{P}; \zeta, s), \lambda_0)} \Big|_{s=0}, \quad (4.16)$$

such that

$$\boxed{d_A(\hat{P}, \lambda_0, \zeta) \simeq a \sqrt{\gamma_{ij,\Sigma} \frac{d}{ds} \gamma^i(\mathcal{G}(\hat{P}; \zeta, 0), \lambda_0) \frac{d}{ds} \gamma^j(\mathcal{G}(\hat{P}; \zeta, 0), \lambda_0)} \Big|_{s=0}}, \quad (4.17)$$

and the expression is no longer dependent on $\delta\omega$. This is the anisotropic equivalent of approximating $h \approx ar\delta\omega$ in (4.2) for sufficiently small $\delta\omega$. In this regime, $\delta\omega$ drops out of the expression for the angular diameter distance, and we are left with a more manageable expression that is solely dependent on direction \hat{P} , distance λ_0 and orientation ζ of the arc.

Lastly, we check the isotropic limit of this derivation. In FLRW space-time, equation (4.15) reduces to a familiar form given in Eq. (4.2),

$$d_{A, \text{FLRW}} = \frac{h}{\delta\omega} \simeq \frac{a}{\delta\omega} \int_{-\delta\omega/2}^{\delta\omega/2} ds \sqrt{r^2 (\sin^2(s) + \cos^2(s))} = \frac{ar\delta\omega}{\delta\omega} = aS_{\kappa}(\chi). \quad (4.18)$$

¹⁴Or, equivalently, conformal time, see (4.1).

¹⁵Rigorously speaking, the derivation presented in this section applies to spaces which expand with a uniform, isotropic expansion rate. To generalize to spaces that expand anisotropically, discussed in section 6, one would have to replace the uniform scalar factor $a(t)$ by the scale factor that characterises the expansion in direction \hat{P} .

4.2.2 Luminosity distance

To study the general case for luminosity distance, consider a beam of light emitted over a small solid angle $\delta\Omega$ from a source, which we will approximate as point-like. If the source radiates equally in every direction, then the power through this solid angle can be written as

$$\mathcal{L}_{\text{Beam}} = \mathcal{L}_{\text{Source}} \times \frac{\delta\Omega}{4\pi}. \quad (4.19)$$

Now suppose that this beam of light terminates on a photosensitive plate of a detector (*e.g.* a telescope) at some proper distance λ_0 as in Figure 3. Conservation of energy implies that the power flowing through this plate must be equal to the power flowing through the initial solid angle $\delta\Omega$, up to powers of a to compensate for the expansion of the universe.¹⁶

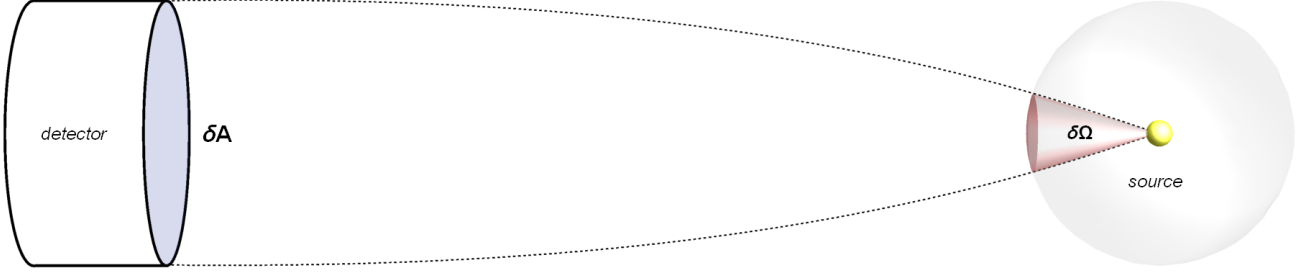


Figure 3: Luminosity distance in an anisotropic space-time

The flux through this plate can thus be written as

$$f_{\text{Detector}} = \frac{\mathcal{L}_{\text{Beam}} a^2}{\delta A} = \frac{\mathcal{L}_{\text{Source}}}{4\pi} \times \frac{\delta\Omega a^2}{\delta A}, \quad (4.20)$$

where δA is the beam's cross-sectional area at distance λ . Comparing this to the definition of d_L in equation (4.3), we can write a general (geometric) expression for the luminosity distance as

$$d_L = \frac{1}{a} \sqrt{\frac{\delta A}{\delta\Omega}}. \quad (4.21)$$

Following the approach in Section 4.2.1, we use homogeneity of spatial sections to place the source at the origin and pick \hat{P} to be the initial direction of an emitted photon. This situation is sketched in Figure 4.

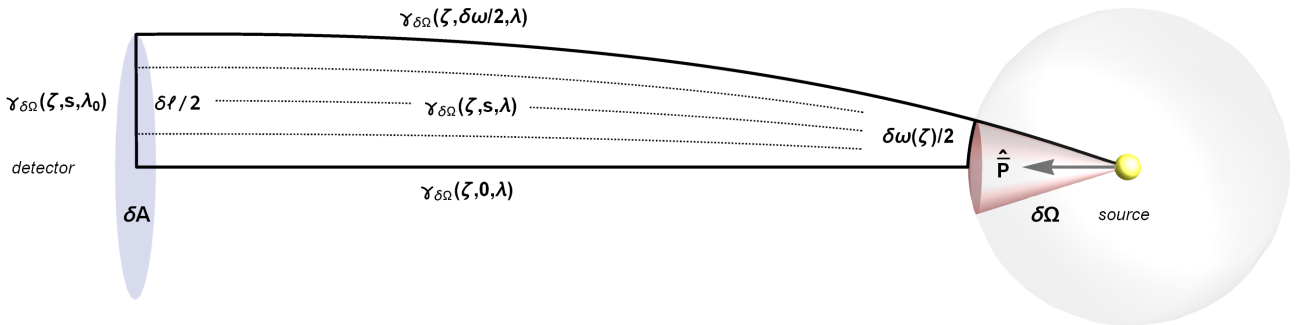


Figure 4: Luminosity distance in an anisotropic space-time.

We can describe this solid angle $\delta\Omega$ by specifying the angular distance $\delta\omega(\zeta)/2$ from the vector \hat{P} to the edge of $\delta\Omega$ along every direction ζ .¹⁷ This means we can write,

$$\delta\Omega(\hat{P}, \delta\omega(\zeta)) := \{\mathcal{G}(\hat{P}; \zeta, s) \mid \zeta \in [0, 2\pi) \ \& \ s \in [0, \delta\omega(\zeta)/2]\}, \quad (4.22)$$

¹⁶Note that we make the additional implicit assumption here λ_0 is small compared to L so that no extreme lensing effects occur that might cause beams emitted in disparate directions to intersect. Such intersections are typical for positively curved spaces ($\kappa > 0$), but usually do not occur in negatively curved spaces ($\kappa < 0$).

¹⁷Note that we have implicitly assumed here that $\delta\Omega$ is convex and so can be conveniently parameterised this manner. This assumption is not necessary to the derivation, as we will eventually arrive at an expression that is independent of $\delta\Omega$. However, making this assumption here means we avoid additional complexity surrounding the parameterization of $\delta\Omega$, which would detract from the clarity of the derivation presented. The assumption is justified in the small- $\delta\Omega$ regime, as the way the small solid angle grows or shrinks as it propagates from source to detector is important at first order and effects of its shape (barring pathological examples) will contribute at higher order.

where \mathcal{G} is the same as in (4.10). As in the previous subsection, for each choice of \hat{P} and $\delta\Omega$ described in this way, we can now find a 2-parameter family of geodesics,

$$\gamma_{\delta\Omega}(\zeta, s, \lambda) = \gamma\left(\mathcal{G}(\hat{P}; \zeta, s), \lambda\right), \quad (4.23)$$

characterized by $\zeta \in [0, 2\pi)$ and $s \in [0, \delta\omega(\zeta)/2]$, that terminates on the plate of the detector at $\lambda = \lambda_0$. As before, the set of initial directions of this sub-family corresponds exactly to the solid angle $\delta\Omega$

$$\left\{ \frac{d\gamma_{\delta\Omega}(\zeta, s, \lambda)}{d\lambda} \Big|_{s \in [0, \delta\omega(\zeta)/2] \ \& \ \zeta \in [0, 2\pi) \ \& \ \lambda = 0} \right\} = \delta\Omega. \quad (4.24)$$

From here, it is not difficult to write out the areas $\delta\Omega$ and δA in integral form:

$$\delta A = \frac{1}{2} \int_0^{2\pi} \left(\frac{\ell(\zeta)}{2} \right)^2 d\zeta = \frac{1}{2} \int_0^{2\pi} \left(\int_0^{\delta\omega(\zeta)/2} ds \sqrt{\gamma_{ij, \Sigma} \frac{d\gamma^i(\mathcal{G}(\hat{P}; \zeta, s), \lambda_0)}{ds} \frac{d\gamma^j(\mathcal{G}(\hat{P}; \zeta, s), \lambda_0)}{ds}} \right)^2 d\zeta \quad (4.25)$$

$$\delta\Omega = \frac{1}{2} \int_0^{2\pi} \left(\frac{\delta\omega(\zeta)}{2} \right)^2 d\zeta. \quad (4.26)$$

If we divide the first integral by the second, we get the ratio we are looking for. However, there is one subtlety to be addressed. We have derived an expression for the luminosity distance dependent on \hat{P} , which is the direction in which the luminous source emitted the light that reaches the observer, as expressed in the local inertial frame of the source. Observationally, we are more interested in an expression dependent on \hat{P} , see figure 5, which is the direction in which an observer views a luminous source as measured in the local inertial frame of the observer. So what remains to be done is to find some way of connecting these vectors and translating them from one frame to another.

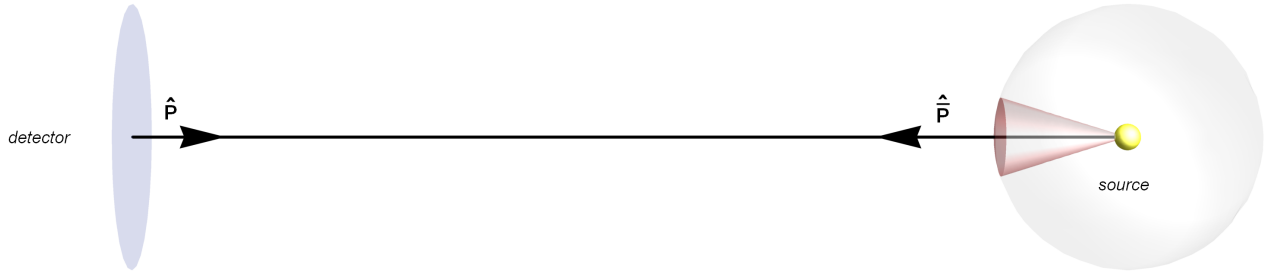


Figure 5: Relationship between \hat{P} and $\hat{\hat{P}}$.

Homogeneity of spatial slices and reversibility of solutions to the geodesic equation make this (conceptually) relatively straightforward. In the frame of the observer, light is incoming along some direction \hat{P} after having traveled some geodesic distance λ_0 . Since geodesic distance is invariant, we can construct the reverse geodesic $\gamma(\hat{P}, \lambda)$ from the observer back to the source and find the position of the source at $\gamma(\hat{P}, \lambda_0)$. We can then find the initial direction of the photons emitted from the source by taking the derivative of this geodesic at $\lambda = \lambda_0$ and reversing the sign (see figure 5):

$$\hat{\hat{P}} = - \frac{d\gamma(\hat{P}, \lambda)}{d\lambda} \Big|_{\lambda=\lambda_0}. \quad (4.27)$$

However, this is $\hat{\hat{P}}_o$ expressed in the coordinates of the observer, not those of the source. To obtain $\hat{\hat{P}}_s$ in the coordinates of the source, we must construct the transformation T from the frame of the observer to the frame of the source and then apply the tangent map of this transformation, dT , to the equation above,¹⁸

$$\boxed{\hat{\hat{P}}_s[\hat{P}_o] := dT \left(- \frac{d\gamma(\hat{P}_o, \lambda)}{d\lambda} \Big|_{\lambda=\lambda_0} \right)}. \quad (4.33)$$

¹⁸We will work out the Solv geometry case explicitly as an example, as the diagonal metric makes the calculation quick. Suppose that we have two local inertial frames, O and O' , and the second frame has its origin at (a, b, c) with respect to the coordinates of the first, then we can express the metric of both frames in terms of the coordinates of the first,

$$ds^2 = e^{2z/L} dx^2 + e^{-2z/L} dy^2 + dz^2 \quad (4.28)$$

$$ds'^2 = e^{2z'/L} dx'^2 + e^{-2z'/L} dy'^2 + dz'^2 \quad (4.29)$$

$$= e^{2(z+c)/L} dx'^2 + e^{-2(z+c)/L} dy'^2 + dz'^2 \quad (4.30)$$

Since both frames must agree about the geometry of the spatial section, we can equate ds^2 and ds'^2 and then easily relate the two frames

Hence, to obtain the luminosity distance from the point of view of the detector, we need to plug equations (4.25) and (4.26) into (4.21) and replace \hat{P} by $\hat{P}_s(\hat{P}_o)$ as given in (4.33). Putting this together, we can write the following expression for the luminosity distance of a source visible in the direction \hat{P}_o that sits at proper distance λ_0 and emits light at the detector through a solid angle $\delta\Omega$ as

$$\left(d_L(\hat{P}_o, \lambda_0, \delta\Omega)\right)^2 := \frac{1}{a^2} \frac{\delta A}{\delta\Omega} = \frac{1}{a^2} \frac{\int_0^{2\pi} \left(\int_0^{\delta\omega(\zeta)/2} ds \sqrt{\gamma_{ij,\Sigma} \frac{d}{ds} \gamma^i \left(\mathcal{G} \left(\hat{P}_s[\hat{P}_o]; \zeta, s \right), \lambda_0 \right) \frac{d}{ds} \gamma^j \left(\mathcal{G} \left(\hat{P}_s[\hat{P}_o]; \zeta, s \right), \lambda_0 \right)} \right)^2 d\zeta}{\int_0^{2\pi} \left(\frac{\delta\omega(\zeta)}{2} \right)^2 d\zeta}. \quad (4.34)$$

This expression is not immediately useful, though, as we do not a-priori know what the solid angle $\delta\Omega$ and looks like. One would have to define the shape of the detector plate by setting $\ell(\zeta)$ and then finding $\delta\omega(\zeta)$ so that the family $\gamma_{\delta\Omega}$ maps $\delta\Omega$ exactly onto δA . This is, however, a hard problem to solve in general.

A more tractable approach can be taken by restricting to the regime where $L \gg \lambda_0 \gg \sqrt{\delta A}$ like we did with angular diameter distance. In this regime, the detector is small and far away enough from the source that $\delta\Omega$ is small compared to unity, but the curvature effects are not so strong that small deviations from the initial angle will lead to extreme differences at distance λ_0 . We can then make use of the approximation in (4.16) to make the following simplification,

$$\delta A \simeq \frac{1}{8} \int_0^{2\pi} \ell^2(\zeta) d\zeta \quad (4.35)$$

$$\delta\Omega \simeq \frac{1}{8} \int_0^{2\pi} \frac{\ell^2(\zeta)}{\left[\gamma_{ij,\Sigma} \frac{d}{ds} \gamma^i \left(\mathcal{G} \left(\hat{P}_s[\hat{P}_o]; \zeta, s \right), \lambda_0 \right) \frac{d}{ds} \gamma^j \left(\mathcal{G} \left(\hat{P}_s[\hat{P}_o]; \zeta, s \right), \lambda_0 \right) \right]_{s=0}} d\zeta. \quad (4.36)$$

This allows us to express the luminosity distance directly as a function of the shape of the detector without making any reference to $\delta\omega$.

Within this same regime, the incoming photon flux is approximately constant across the detector plate. Hence we can make the additional simplifying assumption that the detector is disk-shaped, *i.e.* $\ell(\zeta) = \ell$, as it is the area of the detector plate that is important at first order and the effects of the shape will contribute at higher orders. This means that the dependence on ℓ also drops out of the expression entirely and d_L becomes a purely geometrical quantity depending only on \hat{P}_o and λ_0 ,

$$\left(d_L(\hat{P}_o, \lambda_0)\right)^2 \simeq \frac{2\pi}{a^2} \left(\int_0^{2\pi} \frac{1}{\left[\gamma_{ij,\Sigma} \frac{d}{ds} \gamma^i \left(\mathcal{G} \left(\hat{P}_s[\hat{P}_o]; \zeta, s \right), \lambda_0 \right) \frac{d}{ds} \gamma^j \left(\mathcal{G} \left(\hat{P}_s[\hat{P}_o]; \zeta, s \right), \lambda_0 \right) \right]_{s=0}} d\zeta \right)^{-1}. \quad (4.37)$$

Lastly, we check the isotropic limit of our derivation. In FLRW space-time, equation (4.34) reduces to a familiar form,

$$\left(d_{L, \text{FLRW}}\right)^2 = \frac{1}{a^2} \frac{\delta A}{\delta\Omega} = \frac{1}{a^2} \frac{\int_0^{2\pi} \left(\int_0^{\delta\omega/2} ds \sqrt{r^2 (\sin^2(s) + \cos^2(s))} \right)^2 d\zeta}{\int_0^{2\pi} \left(\frac{\delta\omega(\zeta)}{2} \right)^2 d\zeta} = \frac{1}{a^2} \frac{2\pi r^2 \left(\frac{\delta\omega}{2} \right)^2}{2\pi \left(\frac{\delta\omega}{2} \right)^2} = \frac{S_\kappa^2(\chi)}{a^2}, \quad (4.38)$$

which agrees with Eq. (4.5).

4.2.3 The anisotropic reciprocity theorem

The statement of Etherington's theorem can be amended to hold in a more general anisotropic context. With the notational machinery we have developed in the previous section, this is not a difficult task. We will work explicitly in

by the transformation,

$$T(x, y, z) = (xe^{c/L} + a, ye^{-c/L} + b, z + c) = (x', y', z'). \quad (4.31)$$

Therefore, for the Solv geometry this means that can relate the direction of emission of light from the source, \hat{P}_s , to the direction at which the observer receives this light, \hat{P}_o by

$$\hat{P}_s[\hat{P}_o] = - \left(\frac{d\gamma^1(\hat{P}_o, \lambda)}{d\lambda} e^{c/L}, \frac{d\gamma^2(\hat{P}_o, \lambda)}{d\lambda} e^{-c/L}, \frac{d\gamma^3(\hat{P}_o, \lambda)}{d\lambda} \right)_{\lambda=\lambda_0}. \quad (4.32)$$

Similar analyses can be carried out for the other Thurston geometries, but we refrain from explicating them here for the sake of brevity. Derivations for other geometries are available upon request.

the regime when $L \gg \lambda \gg h$ and $L \gg \lambda \gg \sqrt{\delta A}$, so that we can start from equation (4.37). Next, we recognise term in the denominator of the integrand in this equation as the term on the right-hand side of (4.17) and we write

$$\left(d_L(\hat{P}, \lambda)\right)^{-2} = \frac{a^2}{2\pi} \int_0^{2\pi} \frac{1}{\left[\gamma_{ij, \Sigma} \frac{d}{ds} \gamma^i \left(\mathcal{G}(\hat{P}_s[P]; \zeta, s), \lambda\right) \frac{d}{ds} \gamma^j \left(\mathcal{G}(\hat{P}_s[P]; \zeta, s), \lambda\right)\right]_{s=0}} d\zeta \quad (4.39)$$

$$= \frac{a^2}{2\pi} \int_0^{2\pi} \frac{a^2}{\left(d_A(\hat{P}_s[P], \lambda, \zeta)\right)^2} d\zeta \quad (4.40)$$

so that,

$$\boxed{\frac{1}{d_L^2(\hat{P}, \lambda)} = \frac{a^4}{2\pi} \int_0^{2\pi} \frac{1}{d_A^2(\hat{P}_s[P], \lambda, \zeta)} d\zeta}. \quad (4.41)$$

In the isotropic case where d_A does not depend on ζ , this of course reduces to the familiar isotropic form of Etherington's theorem in (4.6). Its generalization to anisotropic spaces in Eq. (4.41) is one of the principal results of this paper.

5 Distance Measures Visualised

With the machinery we have developed in the previous section, we are only a small step away from visualizing the effect of large-scale curvature on angular diameter distance and luminosity distance. To show the maximal potential extent of these effects, we have opted to generate plots for the largest redshift that we can conceivably optically measure, $z_* \simeq 1091$, or the redshift at the time of recombination.

The plots in this section ¹⁹ were generated by taking the expressions for d_A and d_L , (4.17) and (4.37) from the previous section and setting λ_0 to η_* as shown in Table 3. Where necessary for computational speed, expressions were expanded to order L^{-6} , or, equivalently, κ^3 . The resulting length scales are plotted on the (ϕ, θ) -plane relative to the flat scenario. We have used *red* to signify a distance that is shorter than the spatially flat case and *vice versa* for *blue*.

5.1 Angular diameter distance

The figures below show the angular diameter distance relative to a flat geometry for a large triangle whose far side lies at redshift of $z_* \simeq 1091$. Two bars are drawn for each point on the figure representing the principal axes, meaning that one represents the direction in which the angular diameter distance is *smallest* and the other represents the direction in which the angular diameter distance is *largest*.

The length of the bar represents the (absolute) magnitude of the effect and the color gradient represents magnitude and sign: the bar is colored red if the angular distance is shorter than in the flat case and *vice versa* for blue. Thus a long red bar indicates that the angular diameter is much smaller than flat (relative to other points on the figure) when measured along that direction, while a small blue bar indicates that the distance is a little bit larger than the flat case when measured along that direction. These graphs can also be read as indicating the axes along which objects would be maximally observationally deformed by anisotropic curvature compared to a flat scenario.

Note that every figure is plotted on a separate color gradient, so the scale varies between plots. The Nil geometry shows the strongest effect on any one single arc, followed by the other anisotropic geometries and then the isotropic geometries.

¹⁹ *Mathematica* notebooks are available upon request.

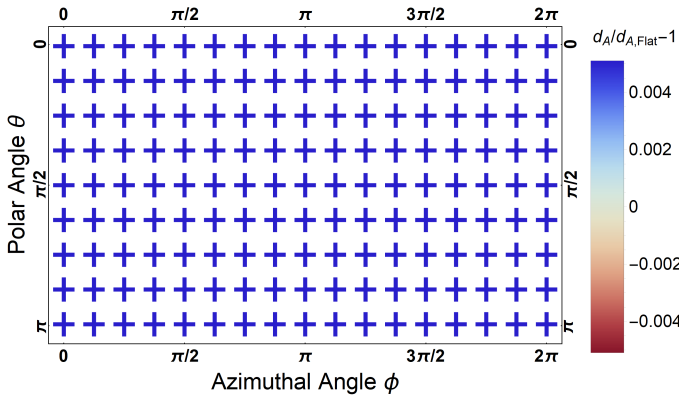


Figure 6: d_A for the \mathbb{H}^3 geometry.

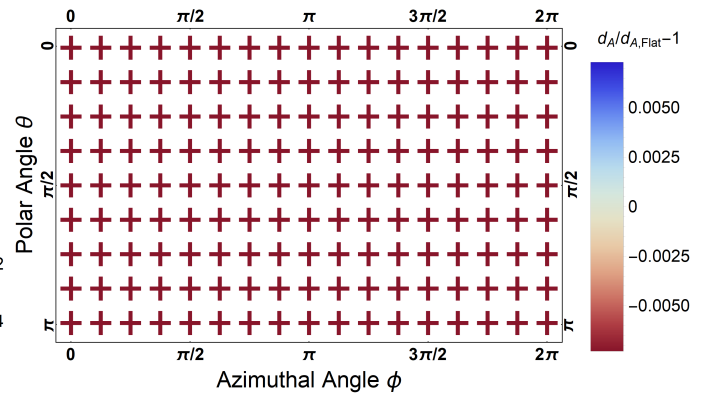


Figure 7: d_A for the S^3 geometry.

As one would expect in the isotropic case, the angular diameter distance shows no dependence on the the direction or orientation of the arc for the \mathbb{H}^3 and S^3 geometries. In the hyperbolic case, a given solid angle in Earth's night sky corresponds to a greater physical area at a given distance from the origin than in a flat model. This area will be populated by proportionally more objects, each of which will appear smaller and thus seem to be further away (blue), see figure 6. The opposite is true of the spherical case, objects will appear larger and therefore appear closer (red), because a smaller volume of space gets projected onto the same solid angle, see figure 7.

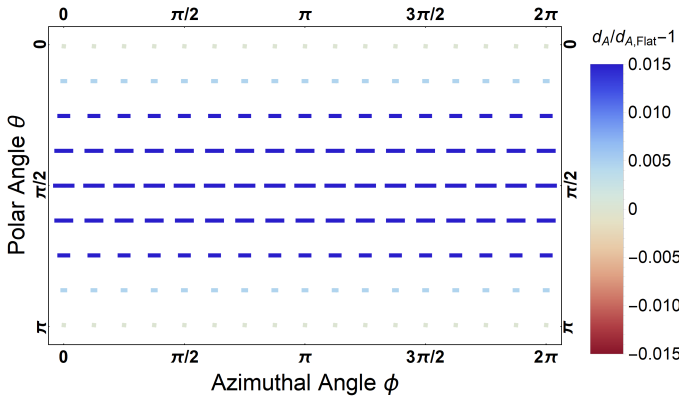


Figure 8: d_A for the $\mathbb{R} \times \mathbb{H}^2$ geometry.

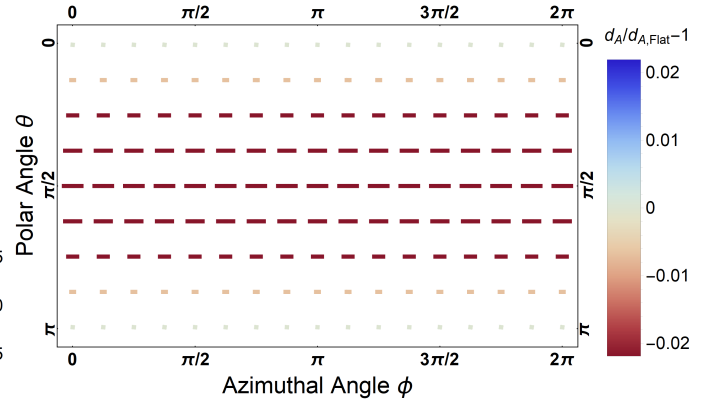


Figure 9: d_L for the $\mathbb{R} \times S^2$ geometry.

The $\mathbb{R} \times \mathbb{H}^2$ and $\mathbb{R} \times S^2$ geometries show the first signs of anisotropy. We see again that the hyperbolic geometry tends to make objects appear further and spherical geometry makes them appear closer. While axial symmetry around the z -axis is preserved, we see that arcs in different directions and orientations are affected differently.

Arcs along the ϕ -directions are maximally stretched or compressed, while arcs along the θ direction are unaffected. The effect is greatest at the equator, which indeed is the plane in which \mathbb{H}^2 and S^2 lie, and vanishes as we turn as we rotate the arc to the poles. This pattern exactly matches the set-up of the spatial sections, which are flat in the z -direction and curved along the (x, y) -plane.

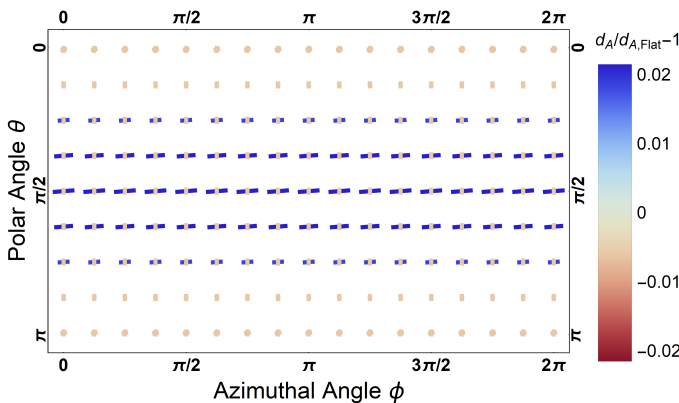


Figure 10: d_A for the $\widetilde{U}(\mathbb{H}^2)$ geometry.

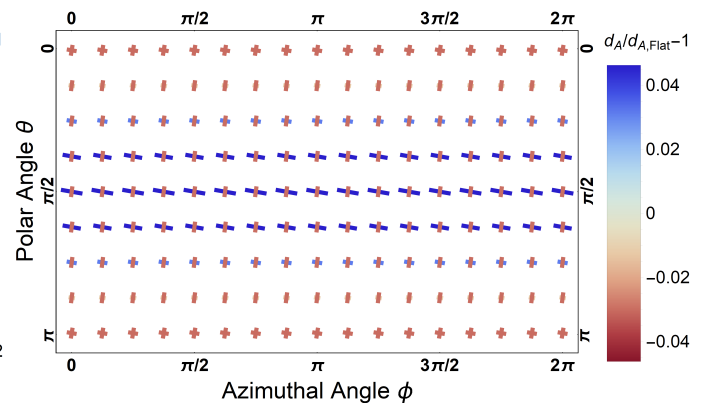


Figure 11: d_A for the Nil geometry.

The figure for the $\widetilde{U}(\mathbb{H}^2)$ geometry bears some resemblance to that of the $\mathbb{R} \times \mathbb{H}^2$ geometry in that arcs along the

equator are contracted. This is not entirely unsurprising, as both geometries use the hyperbolic 2-plane \mathbb{H}^2 as part of their definition. There are some major differences, however.

Most notably, although rotational symmetry around the z -axis is preserved, the arcs that are maximally contracted no longer lie along the ϕ -direction but are tilted slightly out of the (x, y) -plane. This means that we lose mirror symmetry along the cardinal directions, which was present for the previous geometries. Additionally, we see that there is some slight stretching happening just off from the θ -direction, and objects also become stretched in the ϕ -direction towards the poles.

Nil looks very similar to a more extreme version of $\widetilde{U(\mathbb{H}^2)}$ in that the overall behaviour is similar (although mirrored), but the magnitudes are more severe. The scale of the graph has increased by more than a factor of 2, we see that the degree of stretching is more significant compared to the degree of compression and the orientation of the arcs most affected by the anisotropy is tilted out of the cardinal planes to a greater degree.

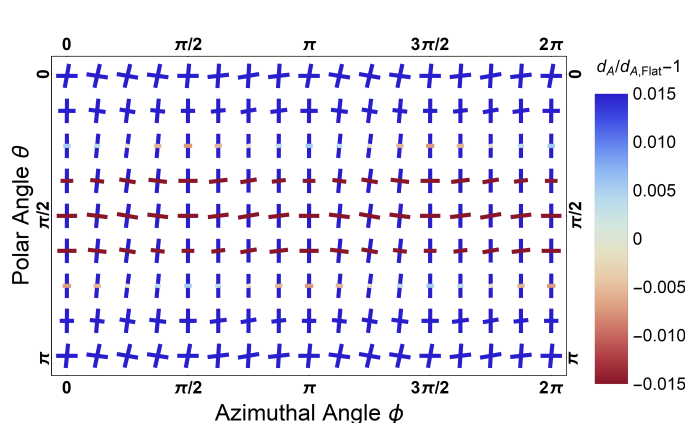


Figure 12: d_A for the Solv geometry.

The Solv behaves like an inverse of $\widetilde{U(\mathbb{H}^2)}$ geometry, objects are stretched rather than compressed along approximately the ϕ -direction at the equator and *vice versa* for the θ -direction. However, there are also significant differences, as the graph for Solv shows a richer behavior.

We see that the angular diameter distance loses its axial symmetry entirely, as we see the two bars are oriented differently at each point on the plot. In addition, we see that the chiefly vertically-oriented arcs are always a deep blue, while the more horizontally-oriented arcs go from a deep blue at the poles to a deep red at the equator. This means that objects are very compressed at the poles, whereas they get deformed significantly at the equator – being elongated in one direction and flattened in another.

5.2 Luminosity distance

The figures below show the luminosity distance relative to a flat geometry at redshift of $z_* \simeq 1091$. Since this measure is now not dependent on a choice of arc, we can use a heat map to show the behavior in greater resolution. Red again indicates that the distance is shorter than the flat case and *vice versa* for blue. Alternatively, these figures can be read as indicating the relative change of apparent luminosity due to anisotropic curvature when compared to a flat geometry.

As before, every figure has its own color gradient, and the scale of the gradient gets larger for each subsequent plot. The growth of the scale in this plots is typically slower than for the angular diameter distance, as the image of an object may be very compressed in one direction but slightly stretched in another direction; this averages out to a moderate decrease in luminosity distance. We see that the anisotropic geometries generate ‘hot’ (brighter) and ‘cold’ (darker) spots at the poles relative to the equator.

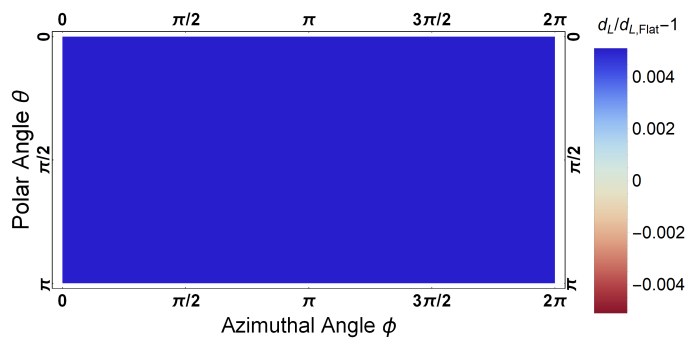


Figure 13: d_L for the \mathbb{H}^3 geometry.

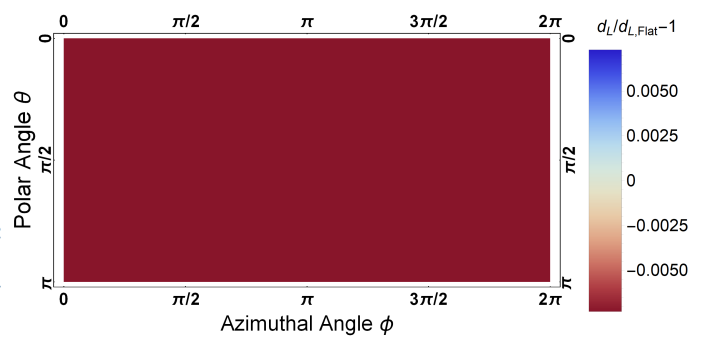


Figure 14: d_L for the S^3 geometry.

The heat maps for the isotropic geometries are again exactly what we expect. They are constant with respect to θ and ϕ , with luminosity distances being longer (blue) in the hyperbolic geometric and shorter (red) in the spherical one.

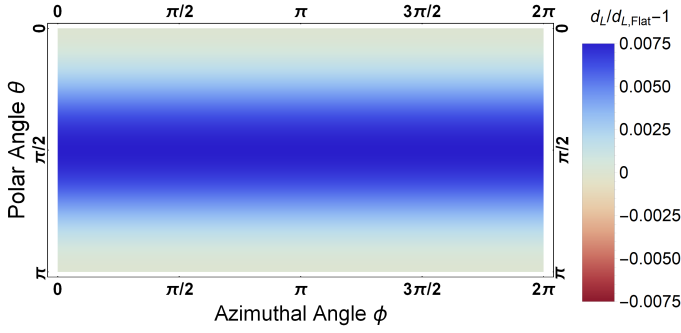


Figure 15: d_L for the $\mathbb{R} \times \mathbb{H}^2$ geometry.

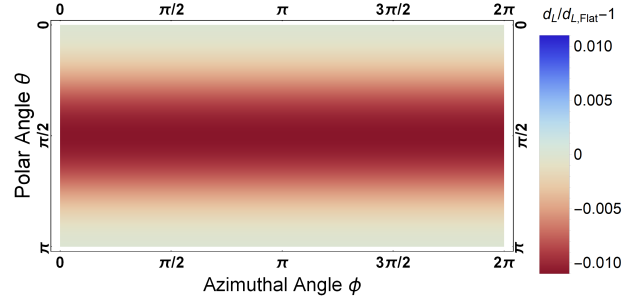


Figure 16: d_L for the $\mathbb{R} \times S^2$ geometry.

The heat maps for the $\mathbb{R} \times \mathbb{H}^2$ and $\mathbb{R} \times S^2$ geometries display the same behaviour as their barred counterparts above. Since objects get deformed in the ϕ -direction – compressed (blue) for \mathbb{H}^2 and elongated (red) for S^2 – the net apparent luminosity changes accordingly. This creates the pattern that we see, the distances are maximally elongated or shortened along the equator of the geometry and the effect vanished towards the poles. Note also that the scale on these luminosity plots differs by about a factor of two from the scale in the angular diameter distance plots, reflecting the fact that the anisotropy only affects one direction.

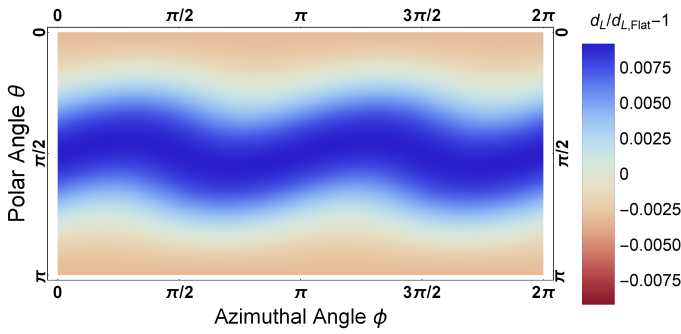


Figure 17: d_L for the $\widetilde{U}(\mathbb{H}^2)$ geometry.

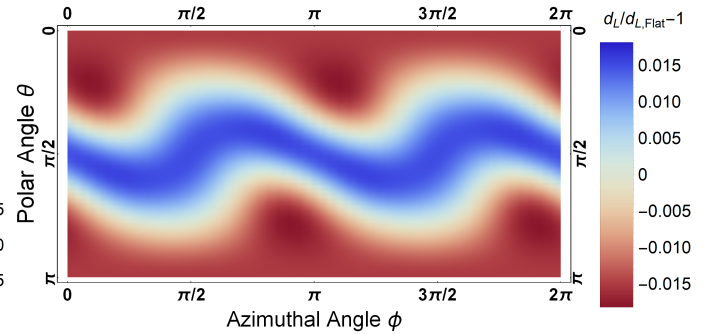


Figure 18: d_L for the Nil geometry.

The heatmap for $\widetilde{U}(\mathbb{H}^2)$ and Nil geometries approximately match what we would expect from their barred plots, an overall decrease in the apparent luminosity along the equator and an increase towards the poles. However, these heatmaps do not show the neat, axially symmetric pattern that we observed for angular diameter distance, but is instead deformed into a wave-like pattern. This deformation is caused by the transformation between \hat{P} and $\widehat{\hat{P}}$ discussed in the previous section, and the direct result of geodesic trajectories being curved (twisted) by the geometry.

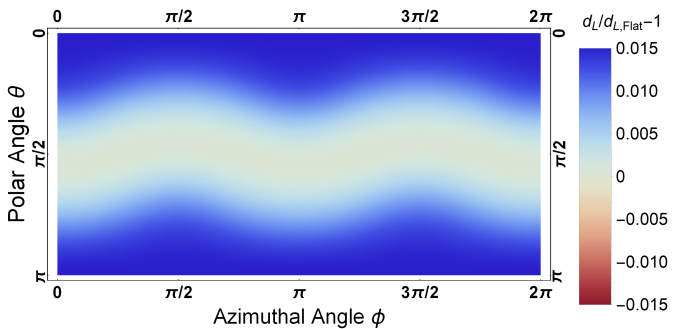


Figure 19: d_L for the Solv geometry

Something similar happens for the Solv geometry, as the equatorial band gets deformed into a wavelike pattern. Note that the scale for the luminosity distance plot of this geometry is similar to that of its angular diameter distance plot, owing to the fact that objects get compressed maximally in both the ϕ and θ directions close to the poles.

5.2.1 Spherical harmonics

Anticipating the use of astronomical data for testing these geometries, we point at an interesting feature of these geometries when their expressions for luminosity distance are expanded in powers of λ/L . For at least the first few powers in this expansion, we observe that the series up to the n -th power can be expanded in spherical harmonics Y_ℓ^m of at most order $\ell = n$, suggesting that this is generally true. However, we do not have a proof that this holds at

higher powers. For example, the luminosity distance for the Nil geometry can be expanded as follows,

$$\begin{aligned}
d_{L,\text{Nil}} = & \left(\frac{\sqrt{\pi}}{36} Y_0^0 - \frac{\sqrt{\pi}}{9\sqrt{5}} Y_2^0 \right) \left(\frac{\lambda}{L} \right)^2 + \left(\frac{i\sqrt{\pi}}{2\sqrt{210}} [Y_3^2 - Y_3^{-2}] \right) \left(\frac{\lambda}{L} \right)^3 \\
& + \left(-\frac{2683\sqrt{\pi}}{43200} Y_0^0 + \frac{11\sqrt{\pi}}{945} Y_2^0 - \frac{5\sqrt{5\pi}}{168\sqrt{6}} [Y_2^2 + Y_2^{-2}] \right) \\
& + \frac{649\sqrt{\pi}}{37800} Y_4^0 - \frac{5\sqrt{5\pi}}{252\sqrt{2}} [Y_4^2 + Y_4^{-2}] + \frac{\sqrt{\pi}}{8\sqrt{70}} [Y_4^4 + Y_4^{-4}] \left(\frac{\lambda}{L} \right)^4 + \mathcal{O} \left(\frac{\lambda}{L} \right)^5.
\end{aligned} \tag{5.1}$$

A visual illustration of this feature for the Nil geometry is given in figures 20-23.²⁰

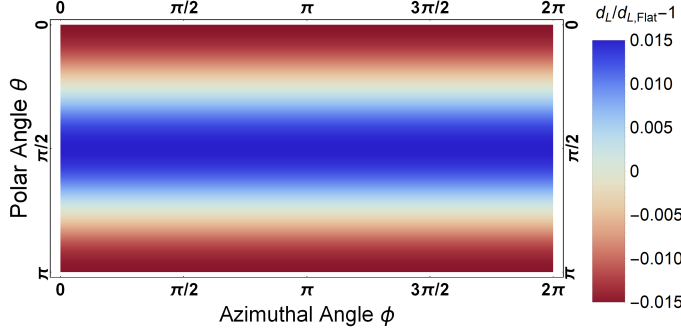


Figure 20: The $(\lambda/L)^2$ modes for the Nil geometry.

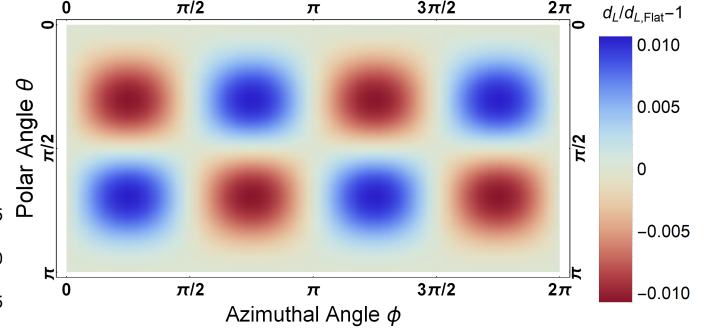


Figure 21: The $(\lambda/L)^3$ modes for the Nil geometry.

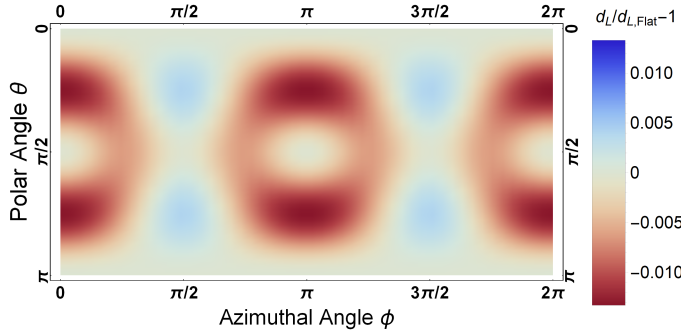


Figure 22: The $(\lambda/L)^4$ modes for the Nil geometry.

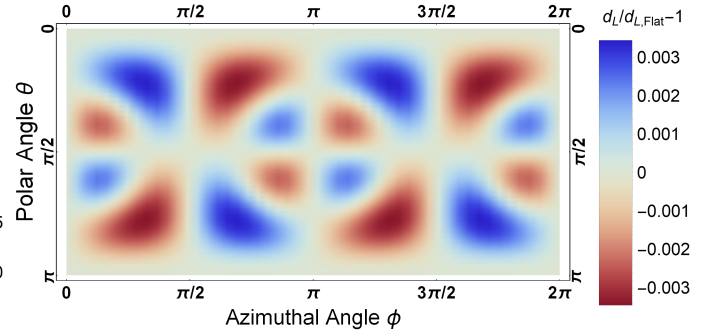


Figure 23: The $(\lambda/L)^5$ modes for the Nil geometry.

5.2.2 Violation of parity & chiral symmetry

Lastly, we point at two other interesting features that may be useful: all of the last three Thurston geometries violate parity, in the sense that one obtains a different metric if the geometry is mirrored through the origin; and two out of three are also chiral, in the sense that one cannot relate the geometry to its mirror image by rotations and translations. See also Table 5. These features gain relevance in light of the recent claims that there is evidence for parity violation both in the CMB data [50, 51, 52, 53] and in the LSS [54, 55, 56].

	Parity	Chirality	x	y	z	$x \ \& \ y$	$x \ \& \ z$	$y \ \& \ z$	$x, y \ \& \ z$
$\widetilde{\text{U}}(\mathbb{H}^2)$	Violated	Chiral	Y	Y	Y	-	-	-	Y
Nil	Violated	Chiral	Y	Y	Y	-	-	-	Y
Solv	Violated	Not Chiral	-	-	Y	-	Y	Y	Y
Rest	Obeeyed	Not Chiral	-	-	-	-	-	-	-

Table 5: This table shows which of the last Thurston geometries violate parity and whether they are chiral or not. In addition, it is stated whether reflection through a given axis yields a different result (Y) or the same metric (-).

This is fairly easy to derive from the metrics of these geometries, which will again present in a simple form below,

²⁰The heat maps of harmonics for other geometries can be obtained upon request.

using $L = \sqrt{-\kappa}$ for notational convenience.

$$d\Sigma_{\widetilde{U(\mathbb{H}^2)}}^2 = dx^2 + \cosh(2x/L)dy^2 + dz^2 + 2 \sinh(x/L)dydz \quad (5.2)$$

$$d\Sigma_{\text{Nil}}^2 = dx^2 + \left(1 + \frac{x^2}{L^2}\right) dy^2 + dz^2 - \frac{2x}{L} dydz \quad (5.3)$$

$$d\Sigma_{\text{Solv}}^2 = e^{2z/L} dx^2 + e^h - 2z/L dy^2 + dz^2 \quad (5.4)$$

The diagonal components of the $\widetilde{U(\mathbb{H}^2)}$ geometry are mirror-even for reflections along cardinal directions, but the off-diagonal component, $2dydz \sinh(x/L)$, is mirror-odd. Hence mirroring this geometry through the origin, which is really mirroring in all three cardinal directions, will flip the sign of this metric and yield a different geometry. Since any rotation can be expressed as a pair of two reflections (typically with respect to two different hyperplanes), it follows that no rotation can undo the effect of a single reflection. Hence this geometry violates parity and is chiral in the sense described above.

The reasoning is similar for the Nil geometry, whose diagonal elements are insensitive to reflections along cardinal directions, but the off-diagonal term $2x dydz/L$ picks up a minus sign if any such reflection is performed. Using the same line of reasoning, Nil is also parity-violating and chiral.

The Solv geometry behaves slightly differently, as only reflection along the z -direction changes the metric by effectively exchanging the coordinates x and y . This change can then simply be undone by rotating by 90 degrees in the (x, y) -plane to return the metric to its original form. It follows that this geometry violates parity, but is not chiral in the sense described above.

This violation of parity is also a visible feature in our plots for luminosity distance. To see this, we can decompose $d_L(\hat{P}, \lambda)$ into a parity-even and a parity-odd component using the following expressions,

$$d_L(\hat{P}, \lambda)_{\text{odd}} = \frac{1}{2} \left(d_L(\hat{P}, \lambda) - d_L(-\hat{P}, \lambda) \right) = \frac{1}{2} \left(d_L(\hat{P}, \lambda) - d_L(\hat{P}, -\lambda) \right) \quad (5.5)$$

$$d_L(\hat{P}, \lambda)_{\text{even}} = \frac{1}{2} \left(d_L(\hat{P}, \lambda) + d_L(-\hat{P}, \lambda) \right) = \frac{1}{2} \left(d_L(\hat{P}, \lambda) + d_L(\hat{P}, -\lambda) \right) . \quad (5.6)$$

These expressions are plotted in Figures 24–29 below. Note that equations (5.5) and (5.6) imply that even (odd) powers in λ/L must likewise be parity-even (parity-odd), which can be seen by contrasting Figures 26 and 27 for the Nil geometry with Figures 20–23 above.

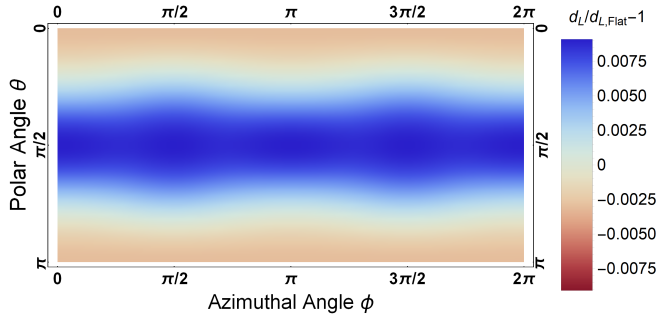


Figure 24: Parity-even component of d_L for $\widetilde{U(\mathbb{H}^2)}$.

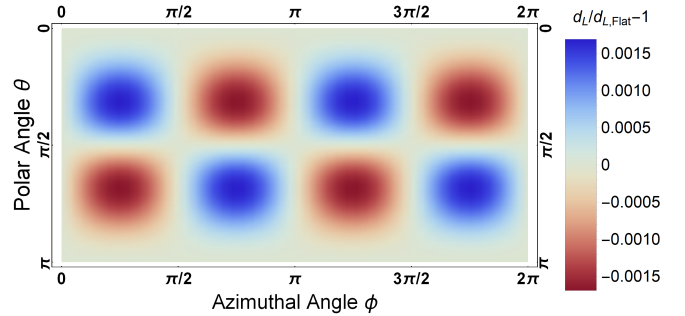


Figure 25: Parity-odd component of d_L for $\widetilde{U(\mathbb{H}^2)}$.

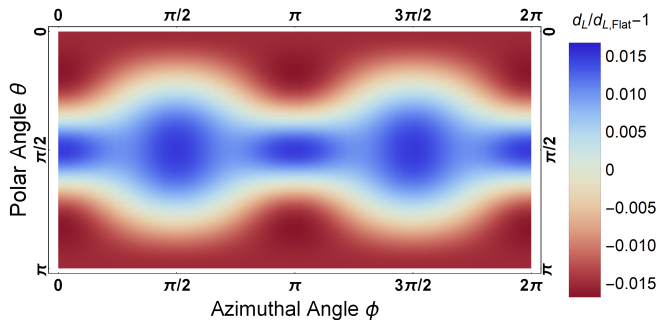


Figure 26: Parity-even component of d_L for Nil.

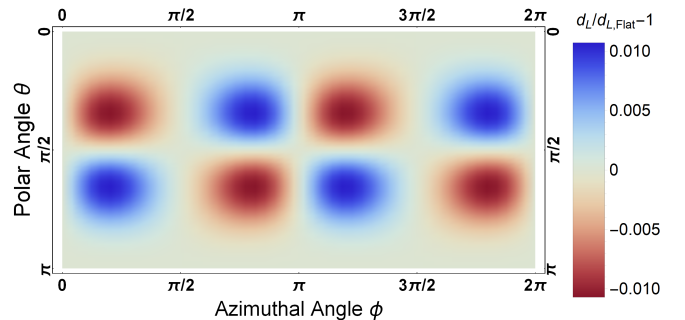


Figure 27: Parity-odd component of d_L for Nil.

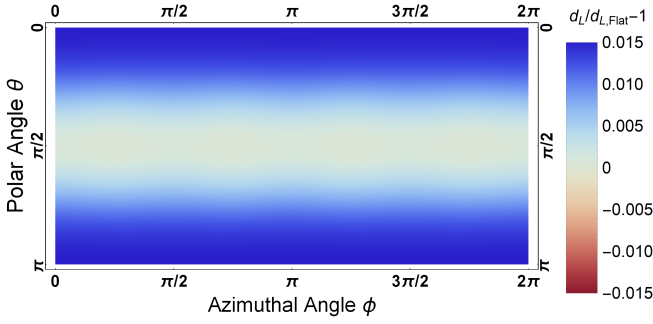


Figure 28: Parity-even component of d_L for Solv.

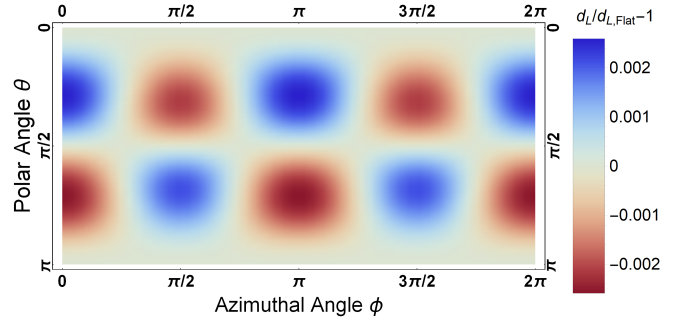


Figure 29: Parity-odd component of d_L for Solv.

Note that all of the reflections marked with Y in Table 5 act through the same mechanism – which is either flipping the sign on the off-diagonal term, or effectively exchanging the x - and y -coordinate. This means that reflection-even and reflection-odd luminosity distances defined in an equivalent manner with respect to any of the reflections marked with Y will yield the same result as the expressions in equations (5.5) and (5.6).

6 Anisotropic Scale Factors

In Section 3, we found that solving the Friedmann equations for anisotropic geometries required the introduction of a rather peculiar fluid with a nonvanishing shear tensor π^i_j and an $\propto a^{-2}$ scaling property. In this section we will ask the question whether we can get rid of this shear tensor by dropping the assumption of isotropy for the scale factor a . In particular, we are interested in figuring out whether this approach is compatible with a perfect fluid solution and in studying the time dependence of anisotropies in the expansion.

We will make a slight alteration to the metric equation (2.2) by splitting the scale factor a into three components, A_1 , A_2 , and A_3 that are *a priori* independent.

$$ds^2 = -dt^2 + \gamma_{ab, \text{Thurston}} \begin{pmatrix} A_1(t) & 0 & 0 \\ 0 & A_2(t) & 0 \\ 0 & 0 & A_3(t) \end{pmatrix}_i^a \begin{pmatrix} A_1(t) & 0 & 0 \\ 0 & A_2(t) & 0 \\ 0 & 0 & A_3(t) \end{pmatrix}_j^b dx^i dx^j, \quad (6.1)$$

The Friedmann equations in an expanding universe in the metric (6.1) (*cf. e.g.* Ref. [57]) depend on the Thurston geometry under consideration, but will admit a generic perfect fluid solution after some work. By splitting a , we introduce non-zero terms in the off-diagonal components of the Einstein tensor that depend on (derivatives of) A_1 , A_2 , and A_3 . If we insist on working in a perfect fluid solution, we must require that these off-diagonal terms vanish. This means that we must solve one or more differential equations that constrain A_1 , A_2 , and A_3 .

For instance, in the Solv geometry, G^0_3 picks up terms dependent on A_1 and A_2 , which must vanish if we wish to obtain a perfect fluid solution. This means that we must require

$$G^0_{3, \text{Solv}} = \frac{\sqrt{-\kappa}}{A_3^2} \left(\dot{A}_2 - \frac{\dot{A}_1}{A_1} \right) = 0. \quad (6.2)$$

One can easily satisfy this equation by setting A_1 proportional to A_2 ; their relative (constant) factor A_2/A_1 can be absorbed by a suitable rescaling of the y -coordinate in the metric. The constraints that follow from applying this procedure to all geometries are shown in Table 6.

Space-time	Constraints	A_{dom}
\mathbb{R}^3	$\kappa = 0$	n/a
$\mathbb{H}^3/\mathbb{S}^3$	$A_1 = A_2 = A_3$	a
$\mathbb{R} \times \mathbb{H}^2/\mathbb{S}^2$	$A_1 = A_2$	A_1
$\widetilde{\mathbb{U}}(\mathbb{H}^2)$	$A_1 = A_2 = A_3$	a
Nil	$A_2 = A_3$	A_1
Solv	$A_1 = A_2$	A_3

Table 6: Anisotropic scale factor constraints and the dominant contribution to the Einstein field equations.

The $\widetilde{\mathbb{U}}(\mathbb{H}^2)$ and Nil geometries are again somewhat exceptional here, as $G^3_2 = x\sqrt{-\kappa}\kappa/A_1(t)^2$ cannot be made to vanish by equating scale factors. However, as discussed in Section 3, this term is suppressed by $x/L \ll 1$ with respect to the leading curvature contributions, and can therefore be neglected at the leading order in κ .

What is of additional note about $\widetilde{U(\mathbb{H}^2)}$ is that the constraint equations force the scale factors for all three directions to be the same. This means that it is not possible for this geometry to get rid of the special $\propto a^{-2}$ terms in the Einstein Tensor by introducing anisotropic expansion while leaving the underlying geometric structure static. This means we don't know how a universe with this geometry evolves, as spatial sections evolve dynamically; but for sufficiently large L we know that anisotropies remain small and for the periods of time and scales at which we can measure, this effect is likely to be small. We will not spend any additional time on this and leave it as an open problem to devise a peculiar fluid with the appropriate scaling properties or to understand how this geometry can be supported dynamically.

With these constraints satisfied, the diagonal elements of the Einstein field equations take the following form:

$${}^0_0 \text{ equation: } \quad \frac{\dot{A}_1 \dot{A}_2}{A_1 A_2} + \frac{\dot{A}_2 \dot{A}_3}{A_2 A_3} + \frac{\dot{A}_3 \dot{A}_1}{A_3 A_1} = 8\pi G\rho + \Lambda + \frac{K^{(0)}\kappa}{A_{\text{dom}}^2} \quad (6.3)$$

$${}^1_1 \text{ equation: } \quad \frac{\ddot{A}_2}{A_2} + \frac{\ddot{A}_3}{A_3} + \frac{\dot{A}_2 \dot{A}_3}{A_2 A_3} = 8\pi G(-\mathcal{P}) + \Lambda + \frac{K^{(1)}\kappa}{A_{\text{dom}}^2} \quad (6.4)$$

$${}^2_2 \text{ equation: } \quad \frac{\ddot{A}_3}{A_3} + \frac{\ddot{A}_1}{A_1} + \frac{\dot{A}_3 \dot{A}_1}{A_3 A_1} = 8\pi G(-\mathcal{P}) + \Lambda + \frac{K^{(2)}\kappa}{A_{\text{dom}}^2} \quad (6.5)$$

$${}^3_3 \text{ equation: } \quad \frac{\ddot{A}_1}{A_1} + \frac{\ddot{A}_2}{A_2} + \frac{\dot{A}_1 \dot{A}_2}{A_1 A_2} = 8\pi G(-\mathcal{P}) + \Lambda + \frac{K^{(3)}\kappa}{A_{\text{dom}}^2}, \quad (6.6)$$

where \mathcal{P} denotes the (isotropic) pressure and $K^{(0)}$, $K^{(1)}$, $K^{(2)}$ and $K^{(3)}$ are the curvature coupling parameters from Section 3. Here A_{dom} is one of the three anisotropic scale factors, which contributes predominantly to the Einstein field equations; these can be obtained by writing out these field equations and reading off the appropriate factor (see Table 6 above).

It is instructive to introduce the Universe's volume scale, $V = A_1 A_2 A_3$, which shows the growth of some referential volume, in terms of which one can define the average expansion rate $H(t)$ and the average scale factor $a(t)$ as,

$$H(t) \equiv \frac{\dot{a}}{a} = \frac{1}{3} \left(\frac{\dot{A}_1}{A_1} + \frac{\dot{A}_2}{A_2} + \frac{\dot{A}_3}{A_3} \right), \quad a(t) \equiv V^{1/3} = [A_1 A_2 A_3]^{1/3}. \quad (6.7)$$

By pairwise subtracting equations (6.4–6.6) one easily obtains,

$${}^2_2 - {}^1_1 \rightarrow \frac{d}{dt} \left[\frac{\dot{A}_1}{A_2} - \frac{\dot{A}_2}{A_2} \right] + 3H \left[\frac{\dot{A}_1}{A_2} - \frac{\dot{A}_2}{A_2} \right] = \kappa \left[\frac{K^{(2)} - K^{(1)}}{A_{\text{dom}}^2} \right] \quad (6.8)$$

$${}^3_3 - {}^2_2 \rightarrow \frac{d}{dt} \left[\frac{\dot{A}_2}{A_2} - \frac{\dot{A}_3}{A_3} \right] + 3H \left[\frac{\dot{A}_2}{A_2} - \frac{\dot{A}_3}{A_3} \right] = \kappa \left[\frac{K^{(3)} - K^{(2)}}{A_{\text{dom}}^2} \right] \quad (6.9)$$

$${}^1_1 - {}^3_3 \rightarrow \frac{d}{dt} \left[\frac{\dot{A}_3}{A_3} - \frac{\dot{A}_1}{A_2} \right] + 3H \left[\frac{\dot{A}_3}{A_3} - \frac{\dot{A}_1}{A_2} \right] = \kappa \left[\frac{K^{(1)} - K^{(3)}}{A_{\text{dom}}^2} \right]. \quad (6.10)$$

It is convenient to introduce differential expansion rates,

$$\Delta H_{12} = \frac{\dot{A}_1}{A_1} - \frac{\dot{A}_2}{A_2}, \quad \Delta H_{23} = \frac{\dot{A}_2}{A_2} - \frac{\dot{A}_3}{A_3}, \quad \Delta H_{31} = \frac{\dot{A}_3}{A_3} - \frac{\dot{A}_1}{A_1}, \quad (6.11)$$

in terms of which equations (6.8–6.10) become,

$$\frac{1}{a^3} \frac{d}{dt} [a^3 \Delta H_{12}(t)] = \kappa \left[\frac{K^{(2)} - K^{(1)}}{A_{\text{dom}}^2} \right] \quad (6.12)$$

$$\frac{1}{a^3} \frac{d}{dt} [a^3 \Delta H_{23}(t)] = \kappa \left[\frac{K^{(3)} - K^{(2)}}{A_{\text{dom}}^2} \right] \quad (6.13)$$

$$\frac{1}{a^3} \frac{d}{dt} [a^3 \Delta H_{31}(t)] = \kappa \left[\frac{K^{(1)} - K^{(3)}}{A_{\text{dom}}^2} \right]. \quad (6.14)$$

It is now clear that the anisotropic expansion is generated by κ , *i.e.* when $\kappa = 0$ there exists isotropic Universe solutions. Therefore, when κ is small, one can study anisotropies in powers of κ . With this in mind, equations (6.12–6.14) can be simplified to,

$$\frac{1}{a^3} \frac{d}{dt} [a^3 \Delta H_{12}(t)] = \frac{\kappa}{a^2} [K^{(2)} - K^{(1)}] + \mathcal{O}(\kappa^2) \quad (6.15)$$

$$\frac{1}{a^3} \frac{d}{dt} [a^3 \Delta H_{23}(t)] = \frac{\kappa}{a^2} [K^{(3)} - K^{(2)}] + \mathcal{O}(\kappa^2) \quad (6.16)$$

$$\frac{1}{a^3} \frac{d}{dt} [a^3 \Delta H_{31}(t)] = \frac{\kappa}{a^2} [K^{(1)} - K^{(3)}] + \mathcal{O}(\kappa^2). \quad (6.17)$$

Note that A_{dom} drops out from these equations as, any deviation from a is absorbed into the $\mathcal{O}(\kappa^2)$ terms. This means that the results from hereon are generically applicable to every Thurston geometry. Equations (6.15–6.17) can be integrated upon introducing the following time variable, $d\tau = adt$,

$$\Delta H_{12}(t) = \frac{\kappa\tau}{a^3} \left[K^{(2)} - K^{(1)} \right] + \mathcal{O}(\kappa^2) \quad (6.18)$$

$$\Delta H_{23}(t) = \frac{\kappa\tau}{a^3} \left[K^{(3)} - K^{(2)} \right] + \mathcal{O}(\kappa^2) \quad (6.19)$$

$$\Delta H_{31}(t) = \frac{\kappa\tau}{a^3} \left[K^{(1)} - K^{(3)} \right] + \mathcal{O}(\kappa^2), \quad (6.20)$$

where

$$\tau(t) = \int^t a(t') dt', \quad (6.21)$$

and we assumed that the initial anisotropies (incorporated in the integration constants) are negligibly small. Notice that the individual expansion rates can be expressed in terms of the average expansion rate $H(t)$ and differential expansion rates,

$$H_1 \equiv \frac{\dot{A}_1}{A_1} = H + \frac{\Delta H_{12} - \Delta H_{31}}{3} \quad (6.22)$$

$$H_2 \equiv \frac{\dot{A}_2}{A_2} = H + \frac{\Delta H_{23} - \Delta H_{12}}{3} \quad (6.23)$$

$$H_3 \equiv \frac{\dot{A}_3}{A_3} = H + \frac{\Delta H_{31} - \Delta H_{23}}{3}. \quad (6.24)$$

Inserting this into the Friedmann equation (6.3) gives,

$$3H^2 + \frac{1}{9} \left[\begin{array}{l} (\Delta H_{12} - \Delta H_{31})(\Delta H_{23} - \Delta H_{12}) \\ + (\Delta H_{23} - \Delta H_{12})(\Delta H_{31} - \Delta H_{23}) \\ + (\Delta H_{31} - \Delta H_{23})(\Delta H_{12} - \Delta H_{31}) \end{array} \right] = 8\pi G\rho + \Lambda + \frac{\kappa K^{(0)}}{a^2}. \quad (6.25)$$

Inserting into this the solutions (6.18–6.20) and moving these terms to the right hand side, results in,

$$\begin{aligned} H^2 &= \frac{8\pi G}{3}\rho + \frac{\Lambda}{3} + \frac{\kappa K^{(0)}}{3a^2} - \frac{\kappa^2\tau^2}{27a^6} \left[\begin{array}{l} (K^{(1)} + K^{(2)} - 2K^{(3)})(K^{(2)} + K^{(3)} - 2K^{(1)}) \\ + (K^{(2)} + K^{(3)} - 2K^{(1)})(K^{(3)} + K^{(1)} - 2K^{(2)}) \\ + (K^{(3)} + K^{(1)} - 2K^{(2)})(K^{(1)} + K^{(2)} - 2K^{(3)}) \end{array} \right] \\ &= \frac{8\pi G}{3}\rho + \frac{\Lambda}{3} + \frac{\kappa K^{(0)}}{3a^2} - \frac{\kappa^2\tau^2}{27a^6} \times 3[K^{(1)}K^{(2)} + K^{(2)}K^{(3)} + K^{(3)}K^{(1)} - (K^{(1)})^2 - (K^{(2)})^2 - (K^{(3)})^2], \end{aligned} \quad (6.26)$$

where the last term is of the second order in κ , and it represents the backreaction of the anisotropic expansion on the average (isotropic) expansion rate. The next step is to determine how the individual scale factors deviate from the isotropic expansion. Upon inserting equations (6.18–6.20) and into (6.22–6.24) one obtains,

$$\frac{d}{dt} \ln \left(\frac{A_1(t)}{a(t)} \right) = \frac{\kappa\tau(t)}{3a^3(t)} \left(K^{(2)} + K^{(3)} - 2K^{(1)} \right) \quad (6.27)$$

$$\frac{d}{dt} \ln \left(\frac{A_2(t)}{a(t)} \right) = \frac{\kappa\tau(t)}{3a^3(t)} \left(K^{(3)} + K^{(1)} - 2K^{(2)} \right) \quad (6.28)$$

$$\frac{d}{dt} \ln \left(\frac{A_3(t)}{a(t)} \right) = \frac{\kappa\tau(t)}{3a^3(t)} \left(K^{(1)} + K^{(2)} - 2K^{(3)} \right). \quad (6.29)$$

By introducing a compact notation, $\Delta K_{(1)} = (K^{(2)} + K^{(3)} - 2K^{(1)})/K^{(0)}$ (plus cyclical permutation for $K_{(2)}$ and $K_{(3)}$), these equations can be written as one equation for $A_i(t) = A_1(t)$, $A_2(t)$, or $A_3(t)$ as,

$$\ln \left(\frac{A_i(t)}{a(t)} \right) = \int^t \frac{\kappa\tau(t') \Delta K_{(i)} K^{(0)}}{3a(t')^3} dt'. \quad (6.30)$$

6.1 Growth of anisotropies in an epoch with matter and cosmological constant

It is well-known that relatively recently (at a redshift $z = z_{\text{DE}} \simeq 0.7$) the Universe entered a dark energy dominated epoch, during which it exhibits an accelerated expansion. It is therefore essential to include dark energy when studying the dynamics of anisotropies.

In this section we study the growth of anisotropies in an era dominated by nonrelativistic matter ($\rho_m(t) = \rho_{m,0}/a^3$) and cosmological constant Λ , which we take to represent dark energy. This is an excellent approximation for the observed Universe from the decoupling at $z_* \simeq 1091$ up to today ($z = 0$). Neglecting for now the curvature contribution $\propto \kappa$ (which we know is small), the Friedmann equation (3.15) (*cf.* also the anisotropic Friedmann equation (6.26)) simplifies to,

$$H^2 = \frac{\dot{a}^2}{a^2} = \frac{8\pi G}{3} \frac{\rho_{m,0}}{a^3} + \frac{\Lambda}{3}, \quad (6.31)$$

whose solution is,

$$a(t) = a_{\text{eq}} \sinh^{\frac{2}{3}} \left(\frac{\sqrt{3\Lambda} t}{2} \right), \quad a_{\text{eq}} = \left(\frac{8\pi G \rho_{m,0}}{\Lambda} \right)^{\frac{1}{3}} = \left(\frac{\Omega_{m,0}}{\Omega_{\Lambda,0}} \right)^{1/3}, \quad (6.32)$$

where $\Omega_{m,0} = \rho_{m,0}/H_0^2$, $\Omega_{\Lambda,0} = \Lambda/(3H_0^2)$, t is cosmological time, with $t = 0$ corresponding to the Big Bang singularity. The first step towards understanding the dynamics of anisotropies dictated by Eq. (6.30) is to evaluate the time variable $\tau(t')$ defined in Eq. (6.21), which for the problem at hand reduces to the following integral,

$$\tau(t) = \int^t a(\tilde{t}) d\tilde{t} = \sqrt{\frac{3}{\Lambda}} \frac{1}{(a_{\text{eq}})^{\frac{3}{2}}} \int^a \frac{\tilde{a}^{\frac{3}{2}}}{\sqrt{1 + \left(\frac{\tilde{a}}{a_{\text{eq}}}\right)^3}} d\tilde{a} = \frac{2}{\sqrt{3\Lambda}} a_{\text{eq}} \int^{(a/a_{\text{eq}})^{3/2}} \frac{\tilde{x}^{\frac{2}{3}}}{\sqrt{1 + \tilde{x}^2}} d\tilde{x}, \quad (6.33)$$

where $\tilde{x} = (\tilde{a}/a_{\text{eq}})^{\frac{3}{2}}$ and we made use of,

$$\frac{da}{dt} = \sqrt{\frac{\Lambda}{3}} a_{\text{eq}} \frac{\cosh\left(\frac{\sqrt{3\Lambda} t}{2}\right)}{\sinh^{\frac{1}{3}}\left(\frac{\sqrt{3\Lambda} t}{2}\right)} = \sqrt{\frac{\Lambda}{3}} \frac{(a_{\text{eq}})^{\frac{3}{2}}}{a(t)^{\frac{1}{2}}} \sqrt{1 + \left(\frac{a}{a_{\text{eq}}}\right)^3}. \quad (6.34)$$

Next, by expanding $(1 + \tilde{x}^2)^{-\frac{1}{2}} = \sum_{n=0}^{\infty} \left(\frac{1}{2}\right)_n (-\tilde{x}^2)^n / n!$, where $(z)_n = \Gamma(z+n)/\Gamma(z)$ denotes the Pochhammer symbol, and exchanging the sum and the integral, the integral in equation (6.33) can be evaluated,

$$\begin{aligned} \tau(t) &= \int^t a(\tilde{t}) d\tilde{t} = \frac{2a_{\text{eq}}}{\sqrt{3\Lambda}} \sum_{n=0}^{\infty} \frac{\left(\frac{1}{2}\right)_n (-1)^n}{n!} \int^{x=(a/a_{\text{eq}})^{3/2}} \tilde{x}^{\frac{2}{3}+2n} d\tilde{x} = \frac{a_{\text{eq}}}{\sqrt{3\Lambda}} \sum_{n=0}^{\infty} \frac{\left(\frac{1}{2}\right)_n (-1)^n}{n!} \frac{x^{\frac{5}{3}+2n}}{\frac{5}{3}+2n} \\ &= \frac{a_{\text{eq}}}{\sqrt{3\Lambda}} x^{\frac{5}{3}} \frac{\Gamma\left(\frac{5}{6}\right)}{\Gamma\left(\frac{11}{6}\right)} \sum_{n=0}^{\infty} \frac{\left(\frac{1}{2}\right)_n \left(\frac{5}{6}\right)_n (-x^2)^n}{\left(\frac{11}{6}\right)_n n!} = \frac{a_{\text{eq}}}{\sqrt{3\Lambda}} \frac{6}{5} \left(\frac{a}{a_{\text{eq}}}\right)^{\frac{5}{2}} \times {}_2F_1\left(\frac{1}{2}, \frac{5}{6}; \frac{11}{6}; -\left(\frac{a}{a_{\text{eq}}}\right)^3\right), \end{aligned} \quad (6.35)$$

where ${}_2F_1(\alpha, \beta; \gamma; z)$ denotes Gauss' hypergeometric function. Upon inserting this result into Eqs. (6.27–6.29) one obtains,

$$\ln \left[\frac{A_1(t)}{a(t)} \right] = (K^{(2)} + K^{(3)} - 2K^{(1)}) \frac{2\kappa}{5\Lambda a_{\text{eq}}^3} \int^{a(t)} \frac{da'}{\sqrt{1 + \left(\frac{a'}{a_{\text{eq}}}\right)^3}} \times {}_2F_1\left(\frac{1}{2}, \frac{5}{6}; \frac{11}{6}; -\left(\frac{a'}{a_{\text{eq}}}\right)^3\right) \quad (6.36)$$

$$\ln \left[\frac{A_2(t)}{a(t)} \right] = (K^{(3)} + K^{(1)} - 2K^{(2)}) \frac{2\kappa}{5\Lambda a_{\text{eq}}^3} \int^{a(t)} \frac{da'}{\sqrt{1 + \left(\frac{a'}{a_{\text{eq}}}\right)^3}} \times {}_2F_1\left(\frac{1}{2}, \frac{5}{6}; \frac{11}{6}; -\left(\frac{a'}{a_{\text{eq}}}\right)^3\right) \quad (6.37)$$

$$\ln \left[\frac{A_3(t)}{a(t)} \right] = (K^{(1)} + K^{(2)} - 2K^{(3)}) \frac{2\kappa}{5\Lambda a_{\text{eq}}^3} \int^{a(t)} \frac{da'}{\sqrt{1 + \left(\frac{a'}{a_{\text{eq}}}\right)^3}} \times {}_2F_1\left(\frac{1}{2}, \frac{5}{6}; \frac{11}{6}; -\left(\frac{a'}{a_{\text{eq}}}\right)^3\right). \quad (6.38)$$

By making a few substitutions, and using the compact notation from Eq. (6.30), Eqs. (6.36–6.38) can be rewritten as

$$\ln \left[\frac{A_i(t)}{a(t)} \right] = \Delta K_{(i)} \Omega_{\kappa,0} \times \frac{2}{5\Omega_{m,0}} \int^a da' \frac{{}_2F_1\left(\frac{1}{2}, \frac{5}{6}; \frac{11}{6}; -a'^3 \frac{\Omega_{\Lambda,0}}{\Omega_{m,0}}\right)}{\sqrt{1 + a'^3 \frac{\Omega_{\Lambda,0}}{\Omega_{m,0}}}}. \quad (6.39)$$

Using the values of $\Omega_{\Lambda,0}$ and $\Omega_{m,0}$ from Table 2 we can put constraints on (the growth of) this ratio by constraining each term in kind. In figures 30 and 31 we plot the evolution of anisotropies $\ln(A_i/a)$ (in units of $\Delta K_{(i)} \Omega_{\kappa,0}$) from early in the matter-dominated era up to roughly today (left panel) and up to a distant future (right panel). We see that $\ln(A_i)$ grows linearly with the scale factor in the matter-dominated, but the growth slows down in the dark energy-dominated epoch, asymptoting to a constant in a distant future.

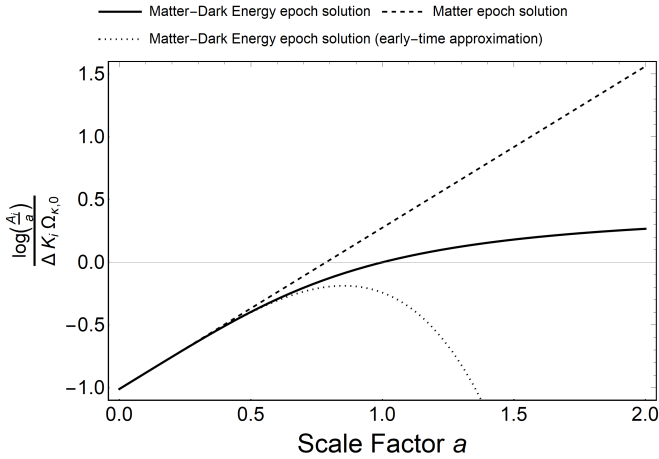


Figure 30: The evolution of anisotropy in equation (6.39). The integration constant is chosen such that the ratio vanishes today (when $a = 1$). Also shown are the matter epoch solution (dashed) and the small- a , early-time expansion from equation (6.40) (dotted). We see that the evolution of $\ln(A_i/a)$ is linear in a in the matter-dominated epoch and slows down in the dark energy-dominated epoch.

In order to understand whether the growth of anisotropies (6.36–6.38) can be neglected in the analysis presented in earlier sections, note first that in predominantly matter era ($z \gg z_{\text{DE}} \simeq 0.7$) the argument of the hypergeometric function in Eq. (6.39) is small, justifying its Taylor expansion (*cf.* Eq. (6.35)). Keeping the two leading terms, the integral in (6.39) evaluates to,

$$\ln \left[\frac{A_i(t)}{a(t)} \right] = \Delta K_{(i)} \Omega_{\kappa,0} \times \frac{2}{5\Omega_{\text{m},0}} a \left(1 - \frac{2}{11} \frac{\Omega_{\Lambda,0}}{\Omega_{\text{m},0}} a^3 \right) + \mathcal{O}(a^7). \quad (6.40)$$

Here we have used gauge freedom to fix anisotropy in the scale factors at zero, *ergo* $A_1 = A_2 = A_3$, at initial time by a suitable (global) rescaling of the spatial coordinates. This is analogous to the gauge freedom to set $a(t_0) = 1$ at present time in isotropic FLRW space-time by a global rescaling of the radial coordinate. This expansion is valid for times earlier than today, *i.e.* when $a = 1/(1+z) < 1$ ($z > 0$).

To get an expansion valid at late times ($a \gg 1$), one can use Eq. (9.132.2) in Ref. [58]²¹ to obtain,

$$\ln \left[\frac{A_i(t)}{a(t)} \right] = \ln \left[\frac{A_i(t)}{a(t)} \right]_{\infty} - \Delta K_{(i)} \Omega_{\kappa,0} \times \frac{1}{2\Omega_{\Lambda,0}} \frac{1}{a^2} \left[1 - \frac{2}{3} \frac{\Gamma(\frac{5}{6})\Gamma(\frac{2}{3})}{\sqrt{\pi}} \left(\frac{\Omega_{\text{m},0}}{\Omega_{\Lambda,0}} \right)^{\frac{1}{3}} \frac{1}{a} - \frac{1}{10} \frac{\Omega_{\text{m},0}}{\Omega_{\Lambda,0}} \frac{1}{a^3} \right] + \mathcal{O}(a^{-6}), \quad (6.42)$$

where we made use of,

$$\frac{{}_2F_1 \left(\frac{1}{2}, -\frac{1}{3}; \frac{2}{3}; -a'^3 \frac{\Omega_{\Lambda,0}}{\Omega_{\text{m},0}} \right)}{\sqrt{1 + a'^3 \frac{\Omega_{\Lambda,0}}{\Omega_{\text{m},0}}}} \simeq \frac{5}{2} \frac{\Omega_{\text{m},0}}{\Omega_{\Lambda,0}} \frac{1 - \frac{1}{4} \frac{1}{a'^3} \frac{\Omega_{\text{m},0}}{\Omega_{\Lambda,0}} - \frac{\Gamma(\frac{5}{6})\Gamma(\frac{2}{3})}{\sqrt{\pi}} \left(a'^3 \frac{\Omega_{\Lambda,0}}{\Omega_{\text{m},0}} \right)^{-\frac{1}{3}}}{a'^3} + \mathcal{O}(a^{-7}). \quad (6.43)$$

Here the constant $\ln \left[\frac{A_i(t)}{a(t)} \right]_{\infty}$ can be evaluated numerically (or read off from the graph in Figure 31). This constant has no relevance for the dynamics of anisotropies, as it can also be subtracted by a suitable global rescaling of the spatial coordinates. This implies that, in a cosmological constant-dominated era (such as inflation), anisotropies in the scale factors $\ln \left[\frac{A_i(t)}{a(t)} \right]$ decay rapidly (exponentially fast) in time as $\propto 1/a^2 \propto e^{-2H_{\Lambda} t}$, where $H_{\Lambda}^2 = \Omega_{\Lambda,0} H_0^2 = \Lambda/3$.

Next we comment on the implications of the above findings. From observations we know that spatial anisotropies today are small, or more quantitatively, $|\Omega_{\kappa,0}| \ll 1$ and $\Delta K_{(i)}$ are at most of the order of unity (*cf.* Table 1). Combining this with the observation that, from the beginning of matter era, $\ln \left[\frac{A_i(t)}{a(t)} \right] / [\Delta K_{(i)} \Omega_{\kappa,0}] \simeq 1$ (which can

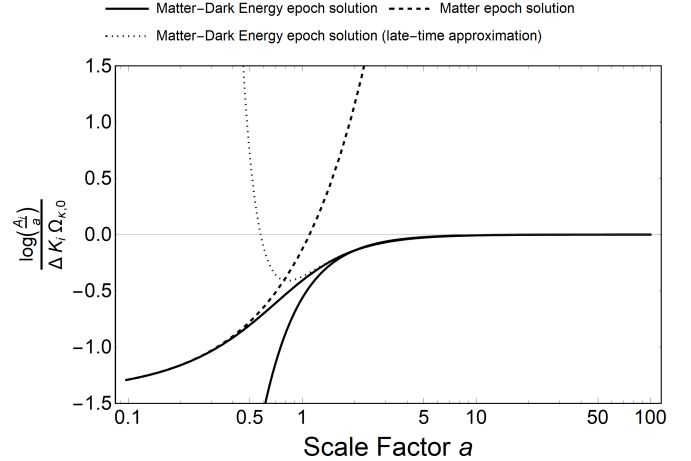


Figure 31: The same graph as on the left, but with a log scale on the horizontal axis to show late-time behaviour. The integration constant is chosen such that the ratio vanishes as $a \rightarrow \infty$. Also shown are the matter epoch solution (dashed) and the large- a , late-time expansion from equation (6.42) (dotted). Whereas in the matter-dominated era anisotropies diverge over time, in the dark energy epoch anisotropies asymptote to a constant value.

²¹According to Eq. (9.132.2) in Ref. [58],

$${}_2F_1 \left(\frac{1}{2}, \frac{5}{6}; \frac{11}{6}; z \right) = \frac{5}{2} (-z)^{-\frac{1}{2}} \times {}_2F_1 \left(\frac{1}{2}, -\frac{1}{3}; \frac{2}{3}; \frac{1}{z} \right) + \frac{\Gamma(\frac{11}{6})\Gamma(-\frac{1}{3})}{\sqrt{\pi}} (-z)^{-\frac{5}{6}}, \quad \left(z = -\frac{\Omega_{\Lambda,0}}{\Omega_{\text{m},0}} a'^3 \right). \quad (6.41)$$

be read off from Figure 30), one can infer from Eq. (6.40) that the change in anisotropies $\Delta(A_i)$ from the beginning of the matter-dominated era up to today ($a = 1$) can be estimated as,

$$\Delta \ln \left[\frac{A_i}{a} \right] \simeq \Delta \left(\frac{A_i}{a} \right) = \frac{A_i}{a} - 1 \simeq \Delta K_{(i)} \Omega_{\kappa,0} \ll 1, \quad (6.44)$$

thus justifying our treatment in Sections 2, 3, 4 and 5, where we neglected the dynamics of anisotropies.²²

6.2 The Anisotropy Problem

With these results in mind, we can make the following remarks regarding whether there is an *anisotropy problem* in the Universe, which can be formulated as follows:

Given that anisotropies grow in the radiation and matter era, and that the observed anisotropies are small today, one must fine-tune the initial geometry of the Universe such to be isotropic to a very high precision.

In order to better understand this problem, let us briefly recall the flatness problem. In an expanding universe with $\epsilon = -\dot{H}/H^2 = \text{constant}$, $\rho_m \propto a^{-2\epsilon}$ ($\epsilon \simeq 0$ in inflation, $\epsilon \simeq 2$ in radiation and $\epsilon = 3/2$ in matter), and therefore,

$$\Omega_\kappa = \frac{\rho_\kappa}{\rho_m} \sim a^{2(\epsilon-1)} \sim e^{2(\epsilon-1)N}, \quad (N = \ln(a)), \quad (6.45)$$

meaning that Ω_κ decays in inflation as $\Omega_\kappa \sim e^{-2N_I}$, and it grows in radiation and matter eras as $\Omega_\kappa \sim e^{2N_R}$ and $\Omega_\kappa \sim e^{N_M}$, respectively, where N_I, N_R and N_M denotes the number of e-foldings in the respective epoch. From this one easily infers that the flatness problem is solved if inflation lasts at least,

$$\text{Flatness problem:} \quad N_I > (N_I)_{\min} = N_R + \frac{1}{2}N_M. \quad (6.46)$$

Let us now consider the growth of anisotropies in an $\epsilon = \text{constant}$ epoch. From Eq. (6.26) we see that anisotropies scale as, $\tau^2/a^6 \sim a^{2\epsilon-4}$, which when compared with $\rho \sim a^{-2\epsilon}$ yields, $\Omega_{\text{anis}} \sim a^{4(\epsilon-1)} \sim e^{4(\epsilon-1)N}$ and $\Omega_{\text{anis}}/\Omega_\kappa \sim a^{2(\epsilon-1)} \sim e^{2(\epsilon-1)N}$, implying that both $\Omega_{\text{anis}} = \rho_{\text{anis}}/\rho$ and $\Omega_{\text{anis}}/\Omega_\kappa$ decay (grow) in accelerating (decelerating) space-times. From this we infer in inflation, $\Omega_{\text{anis}} \sim e^{-4N_I}$, and in radiation and matter era, $\Omega_{\text{anis}} \sim e^{4N_R}$ and $\Omega_{\text{anis}} \sim e^{2N_M}$, respectively. From these observations we see that the anisotropy problem is solved when $-4N_I + 4N_R + 2N_M < 0$, or equivalently,

$$\text{Anisotropy problem:} \quad N_I > (N_I)_{\min} = N_R + \frac{1}{2}N_M, \quad (6.47)$$

which is the same as the condition in Eq. (6.46). Curiously (but not surprisingly), the same condition is obtained if one requires $\Omega_{\text{anis}}/\Omega_\kappa < 1$. Notice that the result (6.47) could have been guessed from Eqs. (6.18–6.24), according to which the relative differences in the Hubble rates scale as, $\Delta H/H \propto a^{2(\epsilon-1)} \sim e^{2(\epsilon-1)N}$.

For our two exceptional cases, Nil and $\widetilde{\text{U}}(\mathbb{H}^2)$ geometries, we note that the off-diagonal contributions to the energy momentum tensor in Eqs. (3.8–3.9) scale as $\propto 1/a^2$. Even though we do not know the precise dynamical geometry of these space-times, it is reasonable to assume that the growth of these off diagonal contributions will follow the same time patterns as the other geometries given this scaling property. Then, by the same logic as footnote 22 we, can trust that the relative error is small as long as equation (6.47) holds.

The principal result of this section is that inflation solves the anisotropy problem of the Universe precisely in the same way as it solves the flatness problem of standard Friedmann cosmologies. This implies that, from a first-principle point of view, *any of the eight Thurston geometries is equally well-motivated to be the geometry of the Universe*. Which one of these is the preferred description of the Universe is a matter to be settled observationally. This finding is one of the main results of this work.

7 Conclusion and Discussion

In this paper we advance the hypothesis that the large scale geometry of spatial sections of the Universe (see equations (1.1–1.2)) can be described as a patchwork of one or more of the eight Thurston-Perelman geometries that

²² Even though it is true that spatial anisotropies are small today and were even smaller in the past, they do grow rapidly in matter era, $\Delta(A_i(t)/a(t)) \sim \Delta K_{(i)} \Omega_{\kappa,0} a(t) \propto 1/(1+z)$, which seems to put into question our estimates of the luminosity distance and angular diameter distance at large redshifts. One can argue that is not a legitimate concern as follows. The question boils down to whether in the distance measures d_L and d_A one can replace a directional scale factor $A_i(t)$ by the average scale factor $a(t)$. The *relative error* one makes in this way (when estimating the effects of spatial anisotropies on d_L and d_A) is at most of the order $\Delta(A_i(t)/a(t)) \sim \Delta K_{(i)} \Omega_{\kappa,0}$, which is $\propto \kappa$, impacting the distance measures at a higher (second) order in κ , such that this effect can be consistently neglected.

are sewn together smoothly. The first three of these eight geometries, as described in section 2, are the well-known homogeneous and isotropic Friedmann-Lemaître-Robertson-Walker (FLRW) geometries. Since FLRW space-times are widely studied and well-understood, we have focused our attention on the remaining five geometries, which are all homogeneous, but violate spatial isotropy. To our knowledge, these geometries were not given a serious consideration in the literature.

In section 3 we have shown that these geometries give rise to a set of Friedmann equations (3.15–3.17), compatible with usual cosmological inventory: matter, radiation and dark energy. However, satisfying these equations requires the introduction of a field with peculiar scaling properties to support the anisotropy of the underlying geometry, which we have assumed in sections 3, 4 and 5 to make the analysis simpler, and thus more pedagogical.

An important question is how one could observationally test the large scale geometry of the Universe and, in particular, how one could distinguish whether we live in a spatially isotropic universe characterised by one of the three FLRW geometries, or in a universe based on one of the five anisotropic Thurston geometries. To answer this question, in Appendices A, B, C and D we have worked out how light propagates in all of the anisotropic Thurston geometries, which are then used in section 4 to calculate angular diameter distance and luminosity distance for all of the geometries. Because of spatial anisotropy of these geometries, we have derived general relations which show how angular diameter distance and luminosity distance depend the underlying geometry. To improve clarity we provide visual representations for all Thurston geometries for both angular diameter distance and luminosity distance in Section 5. These figures show how distant objects would be deformed and dimmed or brightened by the presence of large-scale anisotropies.

In particular, one can infer from Figures 17–19 that, when expanded in powers of λ/L , where λ is the geodesic distance and L the curvature scale, the geometries $\widetilde{U(\mathbb{H}_2)}$, Nil and Solv show a specific angular dependence described by spherical harmonics Y_ℓ^m ($m \in [-\ell, \ell]$), which can be a useful feature when confronting these geometries against data. Finally, in subsection 5.2.2 and Figures 24–29 we show that three of the Thurston geometries, namely $\widetilde{U(\mathbb{H}_2)}$, Nil and Solv, violate parity, and that, in addition, $\widetilde{U(\mathbb{H}_2)}$ and Nil violate chiral symmetry. These properties can also be used for testing these geometries against the data. Namely, the data already show tantalizing hints for parity violation in the Planck data [50, 51, 52, 53] and in the LSS four-point functions [54, 55, 56].

The validity and limitations of the assumption of spatial isotropy are discussed in detail in section 6. In particular, we have shown that in the matter era most of the Thurston geometries²³ can be supported by a standard, spatially isotropic cosmological (perfect) fluid, provided one introduces anisotropic scale factors, which allow for different expansion rates in different spatial directions. Even though anisotropies in the scale factors grow rapidly in the matter era (see Eqs. (6.39–6.42) and Figures 30 and 31), one can show that the Universe’s geometry can remain stable over large periods of time (many e-foldings), and moreover that the corrections in the distance measures induced by the dynamics of anisotropies are of a higher order in curvature κ , *cf.* Eq. (6.26), and therefore can be consistently neglected. Furthermore, even though Thurston geometries pose an anisotropy problem in standard Big Bang cosmologies, it can be solved by a sufficiently long period of cosmic inflation (see Eq. (6.47)) in a way analogous to the flatness problem of standard FLRW space-times.

The next natural step is to make use of the results of this paper to investigate whether the current data contain evidence to single out any one of the Thurston geometries as a preferred candidate, and make forecasts for the upcoming observations. Moreover, the methods developed in the recent study [59] can aid such investigations.

Further theoretical work could also be done to study the effects of anisotropy on the polarization of light. We have seen in subsection 5.2.2 that both parity and chiral symmetry can be violated in the Thurston geometries. One expects that photons with different polarizations will be affected differently in such geometries. Finding such a difference may open up additional avenues for probing curvature anisotropies.

Lastly, it is worth remarking that Thurston’s classification schema is related to the well-known Bianchi spaces, as shown among others in [47, 60]. However a complete discussion of this correspondence is beyond the scope of this paper.

Acknowledgements

This work is part of the Delta ITP consortium, a program of the Netherlands Organisation for Scientific Research (NWO) that is funded by the Dutch Ministry of Education, Culture and Science (OCW).

²³The exceptions are $\widetilde{U(\mathbb{H}_2)}$ and Nil. Even though we do not know the precise dynamics of these geometries, we give a simple argument in favour of long time stability of these geometries.

Appendices

A Geodesics of the $\mathbb{R} \times \mathbb{H}^2$ and $\mathbb{R} \times \mathbb{S}^2$ geometries

The fourth and fifth Thurston geometries are the first anisotropic spaces of Thurston's classification scheme, hence we will begin our treatment of geodesics here. We start from spatial sections of metric (2.6) presented in Section 2,

$$d\Sigma_3^2 = dz^2 + d\chi^2 + S_\kappa^2(\chi)d\phi^2. \quad (\text{A.1})$$

Since this metric is anisotropic, we cannot rely on three-dimensional rotational symmetry to place geodesics along convenient axes. We must therefore solve the Killing equation explicitly, which becomes considerably more simple by using the isometries of the metric in (A.1). If K^i is a Killing vector we can construct a conserved charge,

$$Q_K = K_i(x) \frac{dx^i}{d\lambda}, \quad (\text{A.2})$$

that is constant along geodesic trajectories. With enough Killing vectors, we can solve a set of first-order equations instead. The metric (A.1) has two Killing vectors, ∂_z and ∂_ϕ , which leads to two conserved quantities,

$$P_z = \dot{z}, \quad (\text{A.3})$$

$$L_\phi = S_\kappa^2(\chi)\dot{\phi}. \quad (\text{A.4})$$

We can use these conserved charges together with the requirement that the geodesics are space-like,

$$\epsilon = -g_{ij} \frac{dx^i}{d\lambda} \frac{dx^j}{d\lambda} = -1, \quad (\text{A.5})$$

to write a general (implicit) expression for geodesics of the metric (A.1) as,

$$z(\lambda) = P_z \lambda + z_0 \quad (\text{A.6})$$

$$\dot{\chi}(\lambda) = \pm \sqrt{1 - P_z^2 - L_\phi^2 / S_\kappa^2(\chi(\lambda))} \quad (\text{A.7})$$

$$\dot{\phi}(\lambda) = L_\phi / S_\kappa^2(\chi(\lambda)). \quad (\text{A.8})$$

Radial Geodesics.

Setting $L_\phi = 0$ restricts us to just the spatial radial geodesics and by further requiring that that $x^i(\lambda = 0) = \vec{0}$, they will start at the origin of our coordinate system. These geodesics are then given by

$$z(\lambda) = P_z \lambda \quad (\text{A.9})$$

$$\chi(\lambda) = P_\chi \lambda \quad (\text{A.10})$$

$$\phi(\lambda) = \phi_0, \quad (\text{A.11})$$

under the constraint that $P_z^2 + P_\chi^2 = 1$. This strongly motivates a change of coordinates $z = \rho \cos(\theta)$, $\chi = \rho \sin(\theta)$, under which the metric (A.1) changes to,

$$d\Sigma_3^2 = d\rho^2 + \rho^2 d\theta^2 + S_\kappa^2(\rho \sin(\theta)) d\phi^2. \quad (\text{A.12})$$

In these coordinates, the geodesics look like

$$\rho(\lambda) = \lambda \quad (\text{A.13})$$

$$\theta(\lambda) = \theta_0 \quad (\text{A.14})$$

$$\phi(\lambda) = \phi_0. \quad (\text{A.15})$$

Hence (radial) proper distance to the origin is simply given by $\ell_{\text{rad}} = \lambda_f \equiv \rho_0$.

B Geodesics of the $\widetilde{\text{U}}(\mathbb{H}^2)$ geometry

We start with the metric that we derived in Section 2,

$$d\Sigma_3^2 = dx^2 + dy^2 \cosh^2(x/L) + (dy \sinh^2(x/L) + dz)^2 = dx^2 + dy^2 \cosh(2x/L) + dz^2 + 2dydz \sinh(x/L), \quad (\text{B.1})$$

where we have written $L = 1/\sqrt{-\kappa}$ for notational convenience. Nil has two obvious Killing vectors, ∂_y and ∂_z , which leads to two conserved quantities and therefore to two first-order equations.

$$Q_1 = \dot{y} \cosh(2x/L) + \dot{z} \sinh(x/L) \quad \longrightarrow \quad \dot{y} = \frac{Q_1 - Q_2 \sinh(x/L)}{\cosh^2(x/L)}. \quad (\text{B.2})$$

$$Q_2 = \dot{y} \sinh(x/L) + \dot{z} \quad \longrightarrow \quad \dot{z} = \frac{-Q_1 \sinh(x/L) + Q_2 \cosh(2x/L)}{\cosh^2(x/L)}. \quad (\text{B.3})$$

We can again use the space-like nature of the geodesics so solve for x .

$$1 = g_{ij} \frac{dx^i}{d\lambda} \frac{dx^j}{d\lambda} = \dot{x}^2 + \dot{y}^2 \cosh^2(x/L) + \left(\dot{y} \sinh(x/L) + \dot{z} \right)^2. \quad (\text{B.4})$$

Plugging in conserved charges from (B.2) and (B.3) gives,

$$\dot{x} = \pm \sqrt{1 - Q_2^2 - \frac{\left(Q_1 - Q_2 \sinh(x/L) \right)^2}{\cosh^2(x/L)}}. \quad (\text{B.5})$$

At the origin $(x, y, z) = \vec{0}$ the first-order equations reduce to,

$$\dot{x} = \pm \sqrt{1 - Q_1^2 - Q_2^2} \quad (\text{B.6})$$

$$\dot{y} = Q_1 \quad (\text{B.7})$$

$$\dot{z} = Q_2. \quad (\text{B.8})$$

This means we can reformulate the conserved charges for geodesics crossing the origin in terms of initial momenta, $P_x = \pm \sqrt{1 - Q_1^2 - Q_2^2}$, $P_y = Q_1$ and $P_z = Q_2$, subject to the constraint that $P_x^2 + P_y^2 + P_z^2 = 1$. Since P_x must be real-valued, this tells us that $Q_1^2 + Q_2^2 \leq 1$.

We can now rewrite equation (B.5) as an integral equation by using separation of variables,

$$\int d\lambda = \int dx \left[1 - Q_2^2 - \frac{\left(Q_1 - Q_2 \sinh(x/L) \right)^2}{\cosh^2(x/L)} \right]^{-\frac{1}{2}}. \quad (\text{B.9})$$

We now substitute $w = \sinh(x/L)$, so that $dw = \frac{dx}{L} \cosh(x/L) = \frac{dx}{L} \sqrt{1+w^2}$. With this substitution we can rewrite the integral equation as,

$$\int d\lambda = L \int \frac{dw}{\sqrt{1+w^2}} \left[1 - Q_2^2 - \frac{(Q_1 - Q_2 w)^2}{1+w^2} \right]^{-\frac{1}{2}} \quad (\text{B.10})$$

$$\int d\lambda = L \int \frac{dw}{\sqrt{\underbrace{(1 - 2Q_2^2)}_A w^2 + \underbrace{(2Q_1 Q_2)}_B w + \underbrace{(1 - Q_1^2 - Q_2^2)}_C}}. \quad (\text{B.11})$$

We have now reduced solving the geodesic equation to solving the following integral:

$$\mathcal{I} = \int \frac{dw}{\sqrt{Aw^2 + Bw + C}}. \quad (\text{B.12})$$

Since we are interested in real-valued solutions, we will restrict ourselves to the region where $p \equiv Aw^2 + Bw + C > 0$. Note that A and B take values in the interval $[-1, 1]$ depending on Q_1 and Q_2 while $C = P_x^2$ is restricted to $[0, 1]$. This means we must proceed carefully as both A and the discriminant $\Delta \equiv B^2 - 4AC$ have the potential to take positive and negative values.

To more easily study the different regions, we parameterise the initial velocities as

$$P_x = \sin(\theta) \cos(\phi) \quad (\text{B.13})$$

$$P_y = \sin(\theta) \sin(\phi) \quad (\text{B.14})$$

$$P_z = \cos(\theta). \quad (\text{B.15})$$

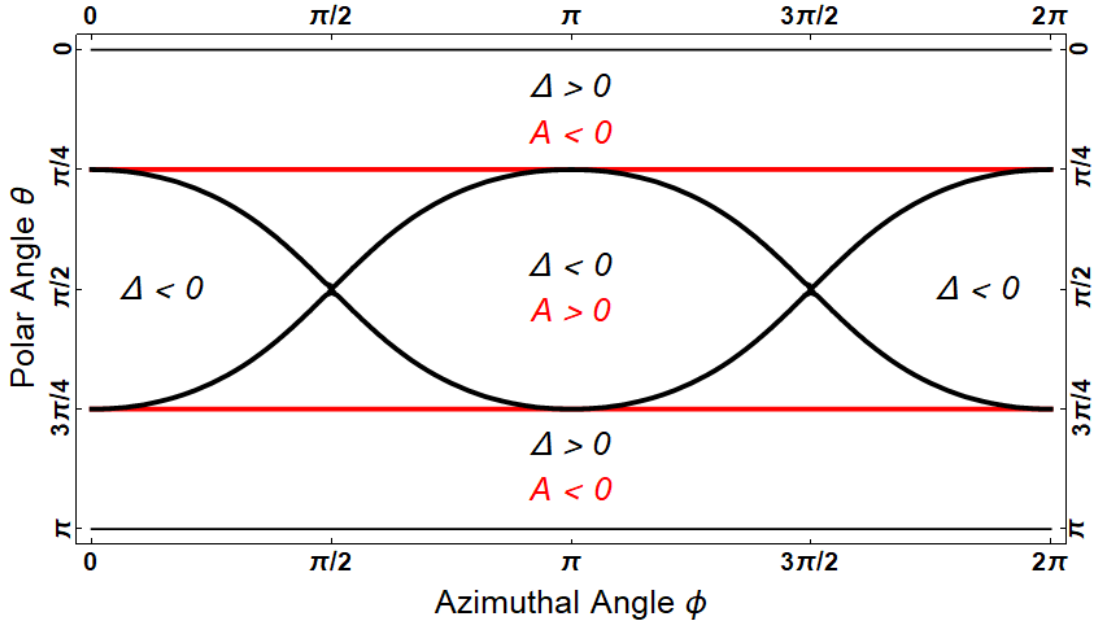


Figure 32: An overview of the regions

We can then plot the sign of A and Δ on the (ϕ, θ) plane in Figure 32 below to visualise the relevant regions.

Case 1: $A > 0$.

The first big region we consider is the region where A is positive. In this case, we can complete the square and substitute $u = w + B/2A$ to get,

$$\mathcal{I} = \frac{1}{\sqrt{A}} \int \frac{dw}{\sqrt{(w + \frac{B}{2A})^2 - \frac{\Delta}{4A^2}}} = \frac{1}{\sqrt{A}} \int \frac{du}{\sqrt{u^2 - \frac{\Delta}{4A^2}}}. \quad (\text{B.16})$$

If $\text{sign}(\Delta) = \pm 1$ then we can define $a = \sqrt{\mp\Delta}/2A$ and write equation (B.16) as

$$\mathcal{I} = \begin{cases} \frac{1}{\sqrt{A}} \int \frac{du}{\sqrt{u^2 + a^2}} = \frac{1}{\sqrt{A}} \ln \left| \frac{u + \sqrt{u^2 + a^2}}{a} \right| = \frac{1}{\sqrt{A}} \ln \left| \frac{2Aw + B + 2\sqrt{A}\sqrt{p}}{\sqrt{-\Delta}} \right|, & \text{if } \Delta < 0 \\ \frac{1}{\sqrt{A}} \int \frac{du}{\sqrt{u^2 - a^2}} = \frac{1}{\sqrt{A}} \ln \left| \frac{u + \sqrt{u^2 - a^2}}{a} \right| = \frac{1}{\sqrt{A}} \ln \left| \frac{2Aw + B + 2\sqrt{A}\sqrt{p}}{\sqrt{\Delta}} \right|, & \text{if } \Delta > 0. \end{cases} \quad (\text{B.17})$$

Let's investigate the sign of the expression inside the absolute value brackets. Since $A > 0$ and $p > 0$ by assumption, we can only have an overall minus sign inside the logarithm if $|2Aw + B| > 2\sqrt{A}\sqrt{Aw^2 + Bw + C}$ and $2Aw + B < 0$. The first condition is equivalent to $\Delta > 0$ (square both sides and rearrange), and the second one to $w < -B/2A$. This means that we never get an overall minus sign in the $\Delta < 0$ case and only sometimes for the $\Delta > 0$ case.

Since the first condition is met for the $\Delta > 0$ case by assumption, we know that the polynomial p has two distinct real-valued roots, $w_{\pm} = -B/2A \pm \sqrt{\Delta}/2A$. Since $A > 0$ we know that p takes non-positive values for $w \in [w_-, w_+]$ and so \mathcal{I} will only have real-valued solutions for $w \in (-\infty, w_-) \cup (w_+, \infty)$. Since $2Aw + B$ is negative if $w < -B/2A$, this means that the argument of the logarithm in the $\Delta > 0$ case is negative when $w < w_-$ and positive when $w > w_+$.

In the third case, $\Delta = 0$, p has exactly one root $w_0 = -B/2A$ and we can rewrite equation (B.16) as

$$\mathcal{I} = \frac{1}{\sqrt{A}} \int \frac{du}{\sqrt{u^2}} = \frac{\text{sign}(u)}{\sqrt{A}} \ln |u| = \begin{cases} -\frac{1}{\sqrt{A}} \ln(-w - B/2A), & \text{if } \Delta = 0 \text{ and } w < w_0 \\ +\frac{1}{\sqrt{A}} \ln(+w + B/2A), & \text{if } \Delta = 0 \text{ and } w > w_0. \end{cases} \quad (\text{B.18})$$

So far we have left the integration constant implicit. We can pick and choose convenient values for this integration

constant to write a complete solution to equation (B.12) when $A > 0$:

$$\mathcal{I} = \begin{cases} +\frac{1}{\sqrt{A}} \ln \left(-2Aw - B - 2\sqrt{A}\sqrt{Aw^2 - Bw + C} \right), & \text{if } \Delta > 0 \text{ and } w < w_- \\ -\frac{1}{\sqrt{A}} \ln \left(-2Aw - B - 2\sqrt{A}\sqrt{Aw^2 + Bw + C} \right), & \text{if } \Delta = 0 \text{ and } w < w_0 \\ +\frac{1}{\sqrt{A}} \ln \left(+2Aw + B + 2\sqrt{A}\sqrt{Aw^2 + Bw + C} \right), & \text{otherwise.} \end{cases} \quad (\text{B.19})$$

Figure 33 below visualises the different regions of this solution.

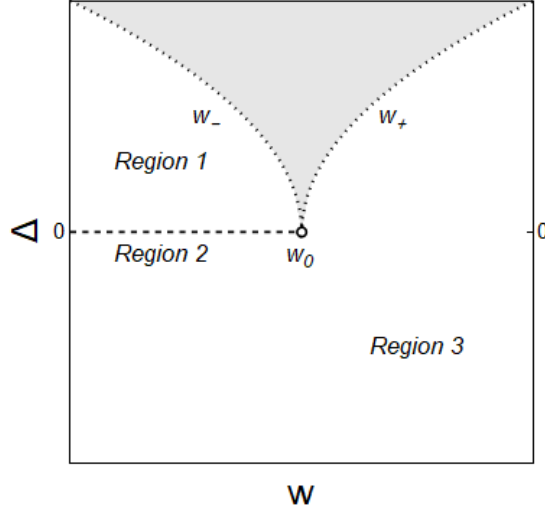


Figure 33: An overview of the domain of \mathcal{I} in the case where $A > 0$. The three solutions above have their domain on the three regions specified, the first being above the dashed line, the second being on the dashed line and the third being on the other side of the dashed line. $p = 0$ on the dotted lines and at $(0,0)$, and the grey area indicates that $p < 0$; there are no real-valued solutions to \mathcal{I} in these regions.

We now plug this result into equation (B.12) to get an equation for the geodesic,

$$\begin{cases} \chi e^{+\sqrt{A}\frac{\lambda}{L}} = -2Aw - B - 2\sqrt{A}\sqrt{Aw^2 - Bw + C}, & \text{if } \Delta > 0 \text{ and } w < w_- \\ \frac{1}{\chi} e^{-\sqrt{A}\frac{\lambda}{L}} = -2Aw - B - 2\sqrt{A}\sqrt{Aw^2 + Bw + C}, & \text{if } \Delta = 0 \text{ and } w < w_0 \\ \chi e^{+\sqrt{A}\frac{\lambda}{L}} = +2Aw + B + 2\sqrt{A}\sqrt{Aw^2 + Bw + C}, & \text{otherwise.} \end{cases} \quad (\text{B.20})$$

Here $\chi > 0$ is an integration constant coming from the $d\lambda$ -integral. We can straightforwardly invert these relations to get w as a function of λ ,

$$w(\lambda) = \begin{cases} +\frac{B^2 - 4AC - \chi^2}{4A\chi} \sinh \left(\sqrt{A}\frac{\lambda}{L} \right) - \frac{B^2 - 4AC + \chi^2}{4A\chi} \cosh \left(\sqrt{A}\frac{\lambda}{L} \right) - \frac{B}{2A}, & \text{if } \Delta > 0 \text{ and } w < w_- \\ -\frac{B^2 - 4AC - \chi^2}{4A\chi} \sinh \left(\sqrt{A}\frac{\lambda}{L} \right) - \frac{B^2 - 4AC + \chi^2}{4A\chi} \cosh \left(\sqrt{A}\frac{\lambda}{L} \right) - \frac{B}{2A}, & \text{if } \Delta = 0 \text{ and } w < w_0 \\ -\frac{B^2 - 4AC - \chi^2}{4A\chi} \sinh \left(\sqrt{A}\frac{\lambda}{L} \right) + \frac{B^2 - 4AC + \chi^2}{4A\chi} \cosh \left(\sqrt{A}\frac{\lambda}{L} \right) - \frac{B}{2A}, & \text{otherwise.} \end{cases} \quad (\text{B.21})$$

The requirement that these geodesics are radial translates to $x(0) = w(0) = 0$, which fixes χ .

$$\chi = \begin{cases} -B \pm 2\sqrt{A}\sqrt{C}, & \text{if } \Delta > 0 \text{ and } w < w_- \\ -B \pm 2\sqrt{A}\sqrt{C}, & \text{if } \Delta = 0 \text{ and } w < w_0 \\ +B \pm 2\sqrt{A}\sqrt{C}, & \text{otherwise.} \end{cases} \quad (\text{B.22})$$

If we plug these values for χ into the expressions for $w(\lambda)$ they collapse to a single expression that is valid for all cases:

$$w(\lambda) = \pm \frac{\sqrt{C}}{\sqrt{A}} \sinh\left(\sqrt{A} \frac{\lambda}{L}\right) + \frac{B}{2A} \left[\cosh\left(\sqrt{A} \frac{\lambda}{L}\right) - 1 \right] \quad (\text{B.23})$$

$$w(\lambda) = \frac{P_x}{\sqrt{1-2P_z^2}} \sinh\left(\sqrt{1-2P_z^2} \frac{\lambda}{L}\right) + \frac{P_y P_z}{1-2P_z^2} \left[\cosh\left(\sqrt{1-2P_z^2} \frac{\lambda}{L}\right) - 1 \right] \quad (\text{B.24})$$

$$x(\lambda) = L \sinh^{-1} \left[\frac{P_x}{\sqrt{1-2P_z^2}} \sinh\left(\sqrt{1-2P_z^2} \frac{\lambda}{L}\right) + \frac{P_y P_z}{1-2P_z^2} \left[\cosh\left(\sqrt{1-2P_z^2} \frac{\lambda}{L}\right) - 1 \right] \right]. \quad (\text{B.25})$$

This expression is a solution to (B.4) and has the correct large- L behaviour, $\lim_{L \rightarrow \infty} x(\lambda) = P_x \lambda$.

Case 2: $\mathbf{A} = 0$.

If $A = 0$ then $\Delta = B^2$ and we only need to consider the $\Delta = 0$ and $\Delta > 0$ scenarios. If $\Delta > 0$ then p reduces to a first-order polynomial $Bw + C$ and if $\Delta = 0$ then p reduces to a constant C . We can then simply write,

$$\lambda - \lambda_0 = \begin{cases} L \frac{2\sqrt{Bw+C}}{B}, & \text{if } \Delta > 0 \\ L \frac{w}{\sqrt{C}}, & \text{if } \Delta = 0. \end{cases} \quad (\text{B.26})$$

We can invert these relationships and require that $x(0) = 0$ to get

$$w(\lambda) = \pm \sqrt{C} \frac{\lambda}{L} + \frac{B}{4} \frac{\lambda^2}{L^2} \quad (\text{B.27})$$

$$w(\lambda) = P_x \frac{\lambda}{L} + \frac{P_y P_z}{2} \frac{\lambda^2}{L^2} \quad (\text{B.28})$$

$$x(\lambda) = L \sinh^{-1} \left[P_x \frac{\lambda}{L} + \frac{P_y P_z}{2} \frac{\lambda^2}{L^2} \right]. \quad (\text{B.29})$$

This expression again covers both the $\Delta = 0$ and $\Delta > 0$ cases and solves (B.4).

Case 3: $\mathbf{A} < 0$.

When $A < 0$ we know that $\Delta = B^2 - 4AC \geq 0$ since C is non-negative. If $\Delta = 0$ then $P_x = 0$, $P_y = 0$ and $P_z = \pm 1$ so that $\vec{x} = (0, 0, P_z \lambda)$ is a solution to the geodesic equation.

If $\Delta > 0$ then we proceed similarly to the $A > 0$ case. We now only find real-valued solutions for \mathcal{I} if $\Delta > 0$ and $w \in (w_-, w_+)$. This means we can again complete the square and substitute $u = w + B/2A$ and $a = \sqrt{\Delta}/2A$ to get

$$\mathcal{I} = \frac{1}{\sqrt{-A}} \int \frac{dw}{\sqrt{-(w + \frac{B}{2A})^2 + \frac{\Delta}{4A^2}}} = \frac{1}{\sqrt{-A}} \int \frac{du}{\sqrt{-u^2 + a^2}}. \quad (\text{B.30})$$

This is a standard integral and we can therefore find a complete solution for (B.11) in the $A < 0$ case as

$$\lambda - \lambda_0 = -\frac{L}{\sqrt{-A}} \arcsin\left(\frac{u}{a}\right) = -\frac{L}{\sqrt{-A}} \arcsin\left(\frac{2Aw + B}{\sqrt{\Delta}}\right), \quad \text{where } |2Aw + B| < \sqrt{\Delta}. \quad (\text{B.31})$$

We again invert these relationships and require that $x(0) = 0$ to get

$$w(\lambda) = \frac{\sqrt{\Delta}}{2(-A)} \sin\left(\sqrt{-A} \frac{\lambda}{L} - \arcsin\left(\frac{B}{\sqrt{\Delta}}\right)\right) - \frac{B}{2A} \quad (\text{B.32})$$

$$w(\lambda) = \frac{\sqrt{P_y^2 P_z^2 + P_x^2 (2P_z^2 - 1)}}{2P_z^2 - 1} \sin\left[\sqrt{2P_z^2 - 1} \frac{\lambda}{L} - \arcsin\left(\frac{P_y P_z}{\sqrt{P_y^2 P_z^2 + P_x^2 (2P_z^2 - 1)}}\right)\right] - \frac{P_y P_z}{2P_z^2 - 1} \quad (\text{B.33})$$

$$x(\lambda) = L \sinh^{-1} [w(\lambda)]. \quad (\text{B.34})$$

Final geodesics.

We can now write the geodesics for the $\widetilde{\text{U}(\mathbb{H}^2)}$ geometry in a compact form.

$$x(\lambda) = L \sinh^{-1} [w(\lambda)] \quad (\text{B.35})$$

$$y(\lambda) = \int d\lambda \frac{-P_z w + P_y}{1 + w^2} \quad (\text{B.36})$$

$$z(\lambda) = \int d\lambda \frac{2P_z w^2 - P_y w + P_z}{1 + w^2}, \quad (\text{B.37})$$

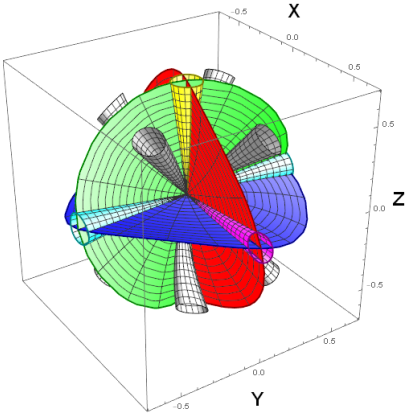


Figure 34: *Geodesics of the $\widetilde{U(\mathbb{H}^2)}$ geometry.* Note that the cyan cone is stretched horizontally, the magenta cone is stretched more harshly vertically, while the yellow cone is largely unaffected.

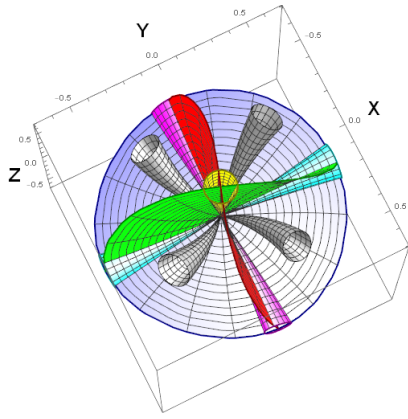


Figure 35: The same visualisation, viewed from a higher angle to show a clockwise twisting effect of geodesics about the z -axis of the geometry; a similar counter-clockwise twist can be observed around the y -axis in the first plot.

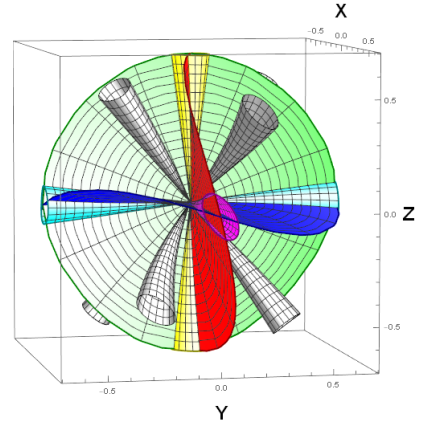


Figure 36: However, around x -axis of the geometry geodesics are skewed towards a diagonal direction rather than twisted.

where w is determined by the value of P_z ,

$$w(\lambda) = \begin{cases} \frac{P_x}{\sqrt{1-2P_z^2}} \sinh\left(\sqrt{1-2P_z^2}\frac{\lambda}{L}\right) + \frac{P_y P_z}{1-2P_z^2} \left[\cosh\left(\sqrt{1-2P_z^2}\frac{\lambda}{L}\right) - 1\right], & \text{if } P_z^2 < 1/2 \\ P_x \frac{\lambda}{L} + \frac{P_y P_z}{2} \frac{\lambda^2}{L^2}, & \text{if } P_z^2 = 1/2 \\ \frac{\sqrt{P_y^2 P_z^2 + P_x^2 (2P_z^2 - 1)}}{2P_z^2 - 1} \sin\left[\sqrt{2P_z^2 - 1}\frac{\lambda}{L} - \arcsin\left(\frac{P_y P_z}{\sqrt{P_y^2 P_z^2 + P_x^2 (2P_z^2 - 1)}}\right)\right] - \frac{P_y P_z}{2P_z^2 - 1}, & \text{if } 1/2 < P_z^2 < 1, \end{cases} \quad (\text{B.38})$$

and we have an additional constraint that $P_x^2 + P_y^2 + P_z^2 = 1$. The fact that these expressions are not smooth with respect to the initial velocity \hat{P} should not worry us. This feature exists within many other dynamical systems, c.f. elliptical, parabolic and hyperbolic trajectories on orbital mechanics.

To visualise these geodesics, Figures 34, 35 and 36 show the trajectory of the above geodesics along selected directions emanating from the origin. The curved red, green and blue surfaces traced by the set of geodesics with an initial direction orthogonal to the x -, y - and z -direction respectively. The magenta, cyan and yellow surfaces are traced by sets of geodesics with an initial direction in a small cone around the x -, y - and z -direction respectively. The grey surfaces are similar, but are cones around initial directions with $|P_x| = |P_y| = |P_z|$. To give a clearer visualisation of the effects of curvature, we have increased its effects by drawing the surfaces from distance $\lambda = 0$ to distance $\lambda = 5\eta_*$.

C Geodesics of the Nil geometry

The Nil case starts along the same general lines from spatial sections of the Nil-metric (2.19),

$$d\Sigma_3^2 = dx^2 + \left(1 + \frac{x^2}{L^2}\right) dy^2 + dz^2 - \frac{2x}{L} dydz. \quad (\text{C.1})$$

Note that we have written $L = 1/\sqrt{-\kappa}$ for notational convenience. Nil has two obvious Killing vectors, ∂_y and ∂_z , which lead two conserved quantities and therefore to two first-order equations,

$$Q_1 = \dot{y} \left(1 + \frac{x^2}{L^2}\right) - x\dot{z}/L \quad \longrightarrow \quad \dot{y} = Q_1 + Q_2 x/L. \quad (\text{C.2})$$

$$Q_2 = \dot{z} - x\dot{y}/L \quad \longrightarrow \quad \dot{z} = Q_2 \left(1 + \frac{x^2}{L^2}\right) + Q_1 x/L. \quad (\text{C.3})$$

Unfortunately, the Nil equivalent of (A.5) does not allow for separation of variables and we must solve the geodesic equation for x directly,

$$\ddot{x}(\lambda) + \frac{Q_2^2}{L^2} \left(x(\lambda) + \frac{Q_1 L}{Q_2}\right) = 0. \quad (\text{C.4})$$

This is the equation for a (shifted) simple harmonic oscillator with angular frequency $\omega = Q_2/L$ and it is solved by,

$$x(\lambda) + \frac{Q_2 L}{Q_1} = C_1 \cos(\omega\lambda) + C_2 \sin(\omega\lambda). \quad (\text{C.5})$$

From this result it is a straightforward, if tedious, exercise to derive a full solution for y and z . We will omit the details of this calculation and skip directly to the solution in a convenient form,

$$x(\lambda) = x_0 + \frac{P_x}{\omega} \sin(\omega\lambda) - \frac{P_y}{\omega} [1 - \cos(\omega\lambda)] \quad (\text{C.6})$$

$$y(\lambda) = y_0 + \frac{P_y}{\omega} \sin(\omega\lambda) + \frac{P_x}{\omega} [1 - \cos(\omega\lambda)] \quad (\text{C.7})$$

$$z(\lambda) = z_0 + L\omega\lambda + \frac{x_0 P_y}{L\omega} \sin(\omega\lambda) + \frac{P_x^2}{4L\omega^2} [\sin(2\omega\lambda) - 2\omega\lambda] + \frac{P_y^2}{4L\omega^2} [2\omega\lambda - 4\sin(\omega\lambda) + \sin(2\omega\lambda)] \quad (\text{C.8})$$

$$+ \frac{2P_x P_y}{L\omega^2} [x_0\omega + P_y \cos(\omega\lambda)] \sin^2\left(\frac{\omega\lambda}{2}\right), \quad (\text{C.9})$$

where we have chosen the Q s, C s and the constants arising from integrating (C.2) and (C.3) so that $x^i(0) = x_0^i$ and $\dot{x}^i(0) = P_i$, and the angular frequency is defined as, $\omega = \frac{LP_z - P_y x_0}{L^2}$.

Radial geodesics.

To make these geodesics radial, we set $x_0 = y_0 = z_0 = 0$. The angular frequency now simplifies to $\omega = P_z/L$ and we may write exact expressions for the geodesics as

$$x(\lambda) = \frac{LP_x}{P_z} \sin\left(\frac{P_z \lambda}{L}\right) - \frac{LP_y}{P_z} \left[1 - \cos\left(\frac{P_z \lambda}{L}\right)\right] \quad (\text{C.10})$$

$$y(\lambda) = \frac{LP_y}{P_z} \sin\left(\frac{P_z \lambda}{L}\right) + \frac{LP_x}{P_z} \left[1 - \cos\left(\frac{P_z \lambda}{L}\right)\right] \quad (\text{C.11})$$

$$z(\lambda) = P_z \lambda + \frac{P_x^2}{4P_z^2} \left[2P_z \lambda - L \sin\left(\frac{2P_z \lambda}{L}\right)\right] + \frac{P_y^2}{4P_z^2} \left[2P_z \lambda - 4L \sin\left(\frac{P_z \lambda}{L}\right) + L \sin\left(\frac{2P_z \lambda}{L}\right)\right] \quad (\text{C.12})$$

$$+ \frac{2LP_x P_y}{P_z^2} \cos\left(\frac{P_z \lambda}{L}\right) \sin^2\left(\frac{P_z \lambda}{2L}\right). \quad (\text{C.13})$$

Given these expressions, it is productive to reconsider equation (A.5), which now reads

$$1 = \epsilon = P_x^2 + P_y^2 + P_z^2. \quad (\text{C.14})$$

In effect, this tells us that if we choose initial velocity vector $\vec{P} = (P_x, P_y, P_z)$ to be of unit length, then λ parameterises geodesic distance along the curve. Hence, proper (radial) distance is again given by $\ell_{\text{rad}} = \lambda_f \equiv \rho_0$.

To visualise these geodesics we have again plotted select geodesics of this geometry in Figures 37, 38 and 39. For a description of the surfaces, please refer to the previous appendix. As in Appendix C, we have augmented the effects of curvature for a clearer visualisation. For this geometry it was sufficient to draw the surfaces from distance $\lambda = 0$ to distance $\lambda = 2.5\eta_*$.

D Geodesics of the Solv geometry

We again start from metric introduced in (2.21) and look at spatial sections,

$$d\Sigma_3^2 = e^{2z/L} dx^2 + e^{-2z/L} dy^2 + dz^2. \quad (\text{D.1})$$

This metric admits three Killing vectors, the first is $K_1 = \partial_x$, the second $K_2 = \partial_y$ and the third $K_3 = -\frac{x}{L}\partial_x - \frac{y}{L}\partial_y + \partial_z$. These lead to the following first-order equations,

$$\dot{x} = P_x e^{-2z/L} \quad (\text{D.2})$$

$$\dot{y} = P_y e^{2z/L} \quad (\text{D.3})$$

$$\dot{z} = P_z + P_x \frac{x}{L} - P_y \frac{y}{L}. \quad (\text{D.4})$$

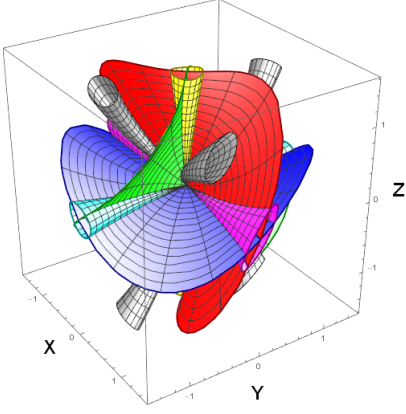


Figure 37: *Geodesics of the Nil geometry.* Like the $\widetilde{U(\mathbb{H}^2)}$ geometry, the cyan cone is stretched horizontally, the magenta cone is stretched more harshly vertically, while the yellow cone is largely unaffected.

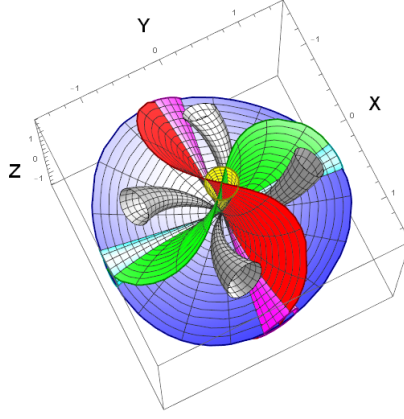


Figure 38: The same visualisation, viewed from a higher angle to show a counter-clockwise twisting effect of geodesics about the z -axis of the geometry; a similar twist can be observed around the y -axis in the first plot.

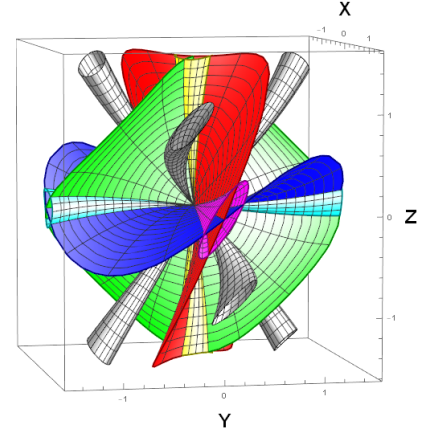


Figure 39: However, around x -axis of the geometry geodesics are skewed towards a diagonal geodesic direction rather than twisted. Note that the diagonal points the other way when compared to $\widetilde{U(\mathbb{H}^2)}$.

Unlike in the previous cases, it is hard to solve this system exactly²⁴ and so we will opt for a perturbative approach.

Radial geodesics.

We can write $\vec{x} = \sum_{i=0}^n \vec{x}_i L^{-i}$ and expand the system above to a desired power L^n . To linear order, for example, this would look like

$$\dot{x} = P_x(1 - 2z/L) \quad (\text{D.7})$$

$$\dot{y} = P_y(1 + 2z/L) \quad (\text{D.8})$$

$$\dot{z} = P_z + P_x \frac{x}{L} - P_y \frac{y}{L}. \quad (\text{D.9})$$

We can then require $x^i(0) = 0$ and equate terms of equal power of L to solve the system. This gives the following result,

$$x(\lambda) = \lambda P_x \left(1 - P_z \frac{\lambda}{L} - \frac{1}{3}(1 - 2P_y^2 + 3P_z^2) \frac{\lambda^2}{L^2} + \dots \right) \quad (\text{D.10})$$

$$y(\lambda) = \lambda P_y \left(1 + P_z \frac{\lambda}{L} + \frac{1}{3}(1 - 2P_y^2 + 3P_z^2) \frac{\lambda^2}{L^2} + \dots \right) \quad (\text{D.11})$$

$$z(\lambda) = P_z \lambda + \frac{P_x^2 - P_y^2}{2} \frac{\lambda}{L} + \frac{P_z^3 - P_z}{3} \frac{\lambda^2}{L^2} + \dots \quad (\text{D.12})$$

We can evaluate the constraint equation (A.5) at $\lambda = 0$, which tells us that $P_x^2 + P_y^2 + P_z^2 = 1$ holds as before. Hence (radial) proper distance to the origin is again given by $\ell_{\text{rad}} = \lambda_f \equiv \rho_0$.

To visualise these geodesics we have again plotted select geodesics of this geometry in Figures 40, 41 and 42. For a description of the surfaces, please refer to the previous appendix. As before, for a clearer visualisation we have augmented the effects of curvature by drawing the surfaces from distance $\lambda = 0$ to distance $\lambda = 2.5\eta_*$.

²⁴Upon inserting equations (D.2–D.3) into equations (D.1) one obtains,

$$1 = \frac{P_x^2}{e^{2z/L}} + \frac{P_y^2}{e^{-2z/L}} + \dot{z}^2 \implies \int \frac{dz}{\sqrt{1 - e^{-2z/L} P_x^2 - e^{2z/L} P_y^2}} = \lambda. \quad (\text{D.5})$$

A convenient variable is $w = e^{z/L}$, in terms of which this equation simplifies to,

$$\int \frac{dw}{\sqrt{w^2 - P_x^2 - w^4 P_y^2}} = \frac{\lambda}{L}. \quad (\text{D.6})$$

This is an elliptic integral, and so its solution can be expressed in terms of elliptic functions. Instead of studying these general solutions, we opt for a much simpler expansion in powers of $1/L$, with the results given in equations (D.10–D.12).

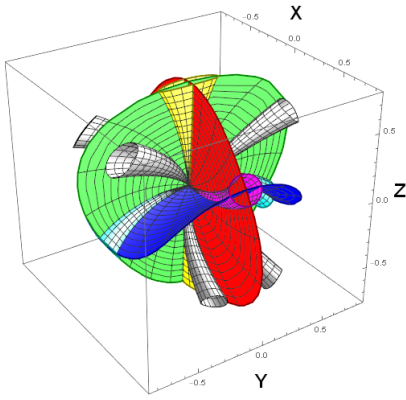


Figure 40: *Geodesics of the Solv geometry.* The geometry is characterized by geodesics being pushed up- or downward respectively depending on whether $|x|$ is larger or smaller than $|y|$.

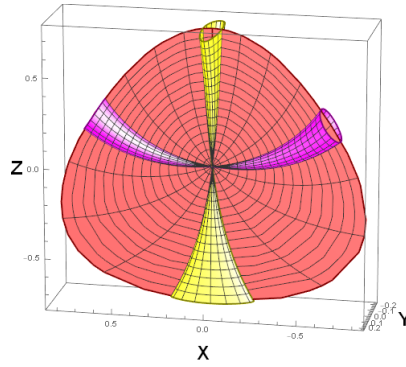


Figure 41: The same visualisation, viewed along the y -direction and with some elements removed to show more clearly how geodesics along the x - z plane are deflected upwards along a distinctive guitar pick shape.

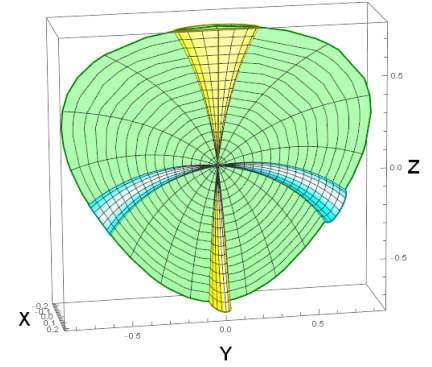


Figure 42: The same visualisation, viewed along the x -direction and with some elements removed to show more clearly how geodesics along the y - z plane are deflected downwards.

References

- [1] E. A. Milne, “World-Structure and the Expansion of the Universe.” *Zeitschrift fur Astrophysik* **6** (1933) 1.
- [2] A. de Oliveira-Costa, M. Tegmark, M. Zaldarriaga and A. Hamilton, “The Significance of the largest scale CMB fluctuations in WMAP,” *Phys. Rev. D* **69** (2004), 063516 doi:10.1103/PhysRevD.69.063516 [arXiv:astro-ph/0307282 [astro-ph]].
- [3] E. Abdalla, G. Franco Abellán, A. Aboubrahim, A. Agnello, O. Akarsu, Y. Akrami, G. Alestas, D. Aloni, L. Amendola and L. A. Anchordoqui, *et al.* “Cosmology intertwined: A review of the particle physics, astrophysics, and cosmology associated with the cosmological tensions and anomalies,” *JHEAp* **34** (2022), 49-211 doi:10.1016/j.jheap.2022.04.002 [arXiv:2203.06142 [astro-ph.CO]].
- [4] P. A. R. Ade *et al.* [Planck], “Planck 2015 results - XVIII. Background geometry and topology of the Universe,” *Astron. Astrophys.* **594** (2016), A18 doi:10.1051/0004-6361/201525829 [arXiv:1502.01593 [astro-ph.CO]].
- [5] P. A. R. Ade *et al.* [Planck], “Planck 2013 results. XXVI. Background geometry and topology of the Universe,” *Astron. Astrophys.* **571** (2014), A26 doi:10.1051/0004-6361/201321546 [arXiv:1303.5086 [astro-ph.CO]].
- [6] Y. Akrami *et al.* [COMPACT], “The Search for the Topology of the Universe Has Just Begun,” [arXiv:2210.11426 [astro-ph.CO]].
- [7] K. Land and J. Magueijo, “Cubic anomalies in WMAP,” *Mon. Not. Roy. Astron. Soc.* **357** (2005), 994-1002 doi:10.1111/j.1365-2966.2005.08707.x [arXiv:astro-ph/0405519 [astro-ph]].
- [8] K. Land and J. Magueijo, “The Axis of evil,” *Phys. Rev. Lett.* **95** (2005), 071301 doi:10.1103/PhysRevLett.95.071301 [arXiv:astro-ph/0502237 [astro-ph]].
- [9] K. Land and J. Magueijo, “The Axis of Evil revisited,” *Mon. Not. Roy. Astron. Soc.* **378** (2007), 153-158 doi:10.1111/j.1365-2966.2007.11749.x [arXiv:astro-ph/0611518 [astro-ph]].
- [10] C. J. Copi, D. Huterer, D. J. Schwarz and G. D. Starkman, “Large-scale alignments from WMAP and Planck,” *Mon. Not. Roy. Astron. Soc.* **449** (2015) no.4, 3458-3470 doi:10.1093/mnras/stv501 [arXiv:1311.4562 [astro-ph.CO]].
- [11] Y. Akrami *et al.* [Planck], “Planck 2018 results. VII. Isotropy and Statistics of the CMB,” *Astron. Astrophys.* **641** (2020), A7 doi:10.1051/0004-6361/201935201 [arXiv:1906.02552 [astro-ph.CO]].
- [12] P. A. R. Ade *et al.* [Planck], “Planck 2015 results. XVI. Isotropy and statistics of the CMB,” *Astron. Astrophys.* **594** (2016), A16 doi:10.1051/0004-6361/201526681 [arXiv:1506.07135 [astro-ph.CO]].
- [13] D. J. Schwarz, C. J. Copi, D. Huterer and G. D. Starkman, “CMB Anomalies after Planck,” *Class. Quant. Grav.* **33** (2016) no.18, 184001 doi:10.1088/0264-9381/33/18/184001 [arXiv:1510.07929 [astro-ph.CO]].

- [14] C. L. Bennett, M. Halpern, G. Hinshaw, et al., “First-Year Wilkinson Microwave Anisotropy Probe (WMAP) Observations: Preliminary Maps and Basic Results,” *Astrophys. J. Supp.* **148** (2003) 1 doi:10.1086/377253
- [15] H. K. Eriksen, F. K. Hansen, A. J. Banday, K. M. Gorski and P. B. Lilje, “Asymmetries in the Cosmic Microwave Background anisotropy field,” *Astrophys. J.* **605** (2004), 14-20 [erratum: *Astrophys. J.* **609** (2004), 1198] doi:10.1086/382267 [arXiv:astro-ph/0307507 [astro-ph]].
- [16] P. Vielva, E. Martinez-Gonzalez, R. B. Barreiro, J. L. Sanz and L. Cayon, “Detection of non-Gaussianity in the WMAP 1 - year data using spherical wavelets,” *Astrophys. J.* **609** (2004), 22-34 doi:10.1086/421007 [arXiv:astro-ph/0310273 [astro-ph]].
- [17] M. Cruz, E. Martinez-Gonzalez, P. Vielva and L. Cayon, “Detection of a non-gaussian spot in wmap,” *Mon. Not. Roy. Astron. Soc.* **356** (2005), 29-40 doi:10.1111/j.1365-2966.2004.08419.x [arXiv:astro-ph/0405341 [astro-ph]].
- [18] J. Jones, C. J. Copi, G. D. Starkman and Y. Akrami, [arXiv:2310.12859 [astro-ph.CO]].
- [19] P. J. E. Peebles, “Anomalies in Physical Cosmology,” [arXiv:2208.05018 [astro-ph.CO]].
- [20] P. Jain, G. Narain and S. Sarala, “Large scale alignment of optical polarizations from distant QSOs using coordinate invariant statistics,” *Mon. Not. Roy. Astron. Soc.* **347** (2004), 394 doi:10.1111/j.1365-2966.2004.07169.x [arXiv:astro-ph/0301530 [astro-ph]].
- [21] G. E. Marinello, R. G. Clowes, L. E. Campusano, G. M. Williger, I. K. Söchting and M. J. Graham, “Compatibility of the Large Quasar Groups with the Concordance Cosmological Model,” *Mon. Not. Roy. Astron. Soc.* **461** (2016) no.3, 2267-2281 doi:10.1093/mnras/stw1513 [arXiv:1603.03260 [astro-ph.CO]].
- [22] P. K. Aluri, P. Cea, P. Chingangbam, M. C. Chu, R. G. Clowes, D. Hutsemékers, J. P. Kochappan, A. Krasinski, A. M. Lopez and L. Liu, *et al.* “Is the Observable Universe Consistent with the Cosmological Principle?,” [arXiv:2207.05765 [astro-ph.CO]].
- [23] N. Secrest, S. von Hausegger, M. Rameez, R. Mohayaee and S. Sarkar, “A Challenge to the Standard Cosmological Model,” [arXiv:2206.05624 [astro-ph.CO]].
- [24] L. Perivolaropoulos and F. Skara, “Challenges for Λ CDM: An update,” *New Astron. Rev.* **95** (2022), 101659 doi:10.1016/j.newar.2022.101659 [arXiv:2105.05208 [astro-ph.CO]].
- [25] N. Aghanim *et al.* [Planck], “Planck 2018 results. VI. Cosmological parameters,” *Astron. Astrophys.* **641** (2020), A6 [erratum: *Astron. Astrophys.* **652** (2021), C4] doi:10.1051/0004-6361/201833910 [arXiv:1807.06209 [astro-ph.CO]].
- [26] T. Louis *et al.* [ACTPol], “The Atacama Cosmology Telescope: Two-Season ACTPol Spectra and Parameters,” *JCAP* **06** (2017), 031 doi:10.1088/1475-7516/2017/06/031 [arXiv:1610.02360 [astro-ph.CO]].
- [27] ACT website: act.princeton.edu (2023).
- [28] EUCLID collaboration website: <https://www.cosmos.esa.int/web/euclid> (2023).
- [29] R. Scaramella *et al.* [Euclid], “Euclid preparation - I. The Euclid Wide Survey,” *Astron. Astrophys.* **662** (2022), A112 doi:10.1051/0004-6361/202141938 [arXiv:2108.01201 [astro-ph.CO]].
- [30] SKAO collaboration website: <https://www.skao.int/en/about-us/skao> (2023).
- [31] C. D. Leonard, P. Bull and R. Allison, “Spatial curvature endgame: Reaching the limit of curvature determination,” *Phys. Rev. D* **94** (2016) no.2, 023502 doi:10.1103/PhysRevD.94.023502 [arXiv:1604.01410 [astro-ph.CO]].
- [32] E. Di Dio, F. Montanari, A. Raccanelli, R. Durrer, M. Kamionkowski and J. Lesgourgues, “Curvature constraints from Large Scale Structure,” *JCAP* **06** (2016), 013 doi:10.1088/1475-7516/2016/06/013 [arXiv:1603.09073 [astro-ph.CO]].
- [33] N. J. Cornish, D. N. Spergel and G. D. Starkman, “Measuring the topology of the universe,” *Proc. Nat. Acad. Sci.* **95** (1998), 82 doi:10.1073/pnas.95.1.82 [arXiv:astro-ph/9708083 [astro-ph]].
- [34] J. P. Luminet and B. F. Roukema, “Topology of the universe: Theory and observation,” [arXiv:astro-ph/9901364 [astro-ph]].
- [35] J. Sandhu, “Cosmic Topology,” [arXiv:1612.04157 [astro-ph.CO]].

- [36] P. Petersen *et al.* [COMPACT], “Cosmic topology. Part I. Limits on orientable Euclidean manifolds from circle searches,” *JCAP* **01** (2023), 030 doi:10.1088/1475-7516/2023/01/030 [arXiv:2211.02603 [astro-ph.CO]].
- [37] A. A. Starobinsky, “New restrictions on spatial topology of the universe from microwave background temperature fluctuations,” *JETP Lett.* **57** (1993), 622-625 [arXiv:gr-qc/9305019 [gr-qc]].
- [38] A. de Oliveira Costa and G. F. Smoot, “Constraints on the topology of the universe from the 2-year COBE data,” *Astrophys. J.* **448** (1995), 477 doi:10.1086/175977 [arXiv:astro-ph/9412003 [astro-ph]].
- [39] N. J. Cornish, D. N. Spergel, G. D. Starkman and E. Komatsu, “Constraining the topology of the universe,” *Phys. Rev. Lett.* **92** (2004), 201302 doi:10.1103/PhysRevLett.92.201302 [arXiv:astro-ph/0310233 [astro-ph]].
- [40] P. M. Vaudrevange, G. D. Starkman, N. J. Cornish and D. N. Spergel, “Constraints on the Topology of the Universe: Extension to General Geometries,” *Phys. Rev. D* **86** (2012), 083526 doi:10.1103/PhysRevD.86.083526 [arXiv:1206.2939 [astro-ph.CO]].
- [41] J. P. Luminet, J. Weeks, A. Riazuelo, R. Lehoucq and J. P. Uzan, “Dodecahedral space topology as an explanation for weak wide - angle temperature correlations in the cosmic microwave background,” *Nature* **425** (2003), 593 doi:10.1038/nature01944 [arXiv:astro-ph/0310253 [astro-ph]].
- [42] A. Bernui, C. P. Novaes, T. S. Pereira and G. D. Starkman, “Topology and the suppression of CMB large-angle correlations,” [arXiv:1809.05924 [astro-ph.CO]].
- [43] William P. Thurston, “Three dimensional Manifolds, Kleinian groups and hyperbolic geometry,” *Bull. Am. Math. Soc. (N.S.)* **6**, 357 (1982).
- [44] G. Perelman, “Finite extinction time for the solutions to the Ricci flow on certain three-manifolds,” [arXiv:math/0307245 [math.DG]].
- [45] G. Perelman, “The Entropy formula for the Ricci flow and its geometric applications,” [arXiv:math/0211159 [math.DG]].
- [46] G. Perelman, “Ricci flow with surgery on three-manifolds,” [arXiv:math/0303109 [math.DG]].
- [47] H. V. Fagundes, “Closed spaces in cosmology,” *Gen. Rel. Grav.* **24** (1992), 199 doi:10.1007/BF00756787 [arXiv:0812.4103 [gr-qc]].
- [48] R. Coquereaux, “The history of the universe is an elliptic curve,” *Class. Quant. Grav.* **32** (2015) no.11, 115013 [erratum: *Class. Quant. Grav.* **33** (2016) no.15, 159601] doi:10.1088/0264-9381/32/11/115013 [arXiv:1411.2192 [gr-qc]].
- [49] R. Coquereaux and A. Grossmann, “Analytic Discussion of Spatially Closed Friedmann Universes With Cosmological Constant and Radiation Pressure,” *Annals Phys.* **143** (1982), 296 doi:10.1016/0003-4916(82)90030-6
- [50] Y. Minami and E. Komatsu, *Phys. Rev. Lett.* **125** (2020) no.22, 221301 doi:10.1103/PhysRevLett.125.221301 [arXiv:2011.11254 [astro-ph.CO]].
- [51] P. Diego-Palazuelos, J. R. Eskilt, Y. Minami, M. Tristram, R. M. Sullivan, A. J. Banday, R. B. Barreiro, H. K. Eriksen, K. M. Górski and R. Keskitalo, *et al.* “Cosmic Birefringence from the Planck Data Release 4,” *Phys. Rev. Lett.* **128** (2022) no.9, 091302 doi:10.1103/PhysRevLett.128.091302 [arXiv:2201.07682 [astro-ph.CO]].
- [52] P. Diego-Palazuelos, E. Martínez-González, P. Vielva, R. B. Barreiro, M. Tristram, E. de la Hoz, J. R. Eskilt, Y. Minami, R. M. Sullivan and A. J. Banday, *et al.* “Robustness of cosmic birefringence measurement against Galactic foreground emission and instrumental systematics,” *JCAP* **01** (2023), 044 doi:10.1088/1475-7516/2023/01/044 [arXiv:2210.07655 [astro-ph.CO]].
- [53] J. R. Eskilt and E. Komatsu, “Improved constraints on cosmic birefringence from the WMAP and Planck cosmic microwave background polarization data,” *Phys. Rev. D* **106** (2022) no.6, 063503 doi:10.1103/PhysRevD.106.063503 [arXiv:2205.13962 [astro-ph.CO]].
- [54] O. H. E. Philcox, “Probing parity violation with the four-point correlation function of BOSS galaxies,” *Phys. Rev. D* **106** (2022) no.6, 063501 doi:10.1103/PhysRevD.106.063501 [arXiv:2206.04227 [astro-ph.CO]].
- [55] C. Creque-Sarbinowski, S. Alexander, M. Kamionkowski and O. Philcox, “Parity-Violating Trispectrum from Chern-Simons Gravity,” [arXiv:2303.04815 [astro-ph.CO]].
- [56] W. R. Coulton, O. H. E. Philcox and F. Villaescusa-Navarro, “Signatures of a Parity-Violating Universe,” [arXiv:2306.11782 [astro-ph.CO]].

- [57] M. Koussour, H. Filali and M. Bennai, “Two Minimally Interacting Fluids: Matter and Holographic Dark Energy in Bianchi Type-I Universe,” doi:10.2139/ssrn.4028697
- [58] Izrail Solomonovich Gradshteyn and Iosif Moiseevich Ryzhik, “Table of integrals, series, and products”, Academic press (2014)
- [59] C. J. G. Vedder, E. Belgacem, N. E. Chisari and T. Prokopec, “Fluctuating Dark Energy and the Luminosity Distance,” [arXiv:2209.00440 [astro-ph.CO]].
- [60] A. E. Fischer and V. Moncrief “Hamiltonian Reduction of Einstein’s Equations” doi:10.1016/B0-12-512666-2/00498-3